Porous Coatings for Chromatography Enhanced Sensors

Abdinassir Hassan Issa

Sixty ECTS credits

Master thesis in Chemistry

Department of chemistry

Faculty of Mathematics and Natural Sciences

UNIVERSITY OF OSLO

June 2023

Porous Coatings for Chromatography Enhanced Sensors

2023

Porous coatings for chromatography enhanced sensors

http://www.duo.uio.no/

Print: Graphic center, University of Oslo

Abstract

Metal Organic Frameworks (MOF) have received significant attention owing to their unique structural properties. Among the numerous developed MOFs, UiO-66 and UiO-67 are considered highly attractive as porous materials for chemical separation. An all-gas-phase approach to synthesize crystalline UiO-66 and UiO-67 has been developed, however, the growth dynamics and the evolution of the films porosity is not yet fully understood.

In this work we explore how the inorganic metal precursor zirconium tetrachloride ($ZrCl_4$) reacts with water, 1,4-benzendicarboxylic acid (1,4-BDC), and Biphenyl-4,4- dicarboxylic acid (BP-4,4-DC) precursors. Using the Atomic Layer Deposition (ALD) technique combined with *in-situ* Quartz Crystal Microbalance (QCM), we find that developing a ZrO_2 film with stable growth proved difficult, with identical deposition parameters leading to variations in film thickness and refractive index.

The growth of Zr-1,4-BDC exhibited standard stable growth with uniform rates of 0.7-0.9 nm/cycle. The reaction scheme indicated a stoichiometry of 1:2, whereas, pulsing water as part of the precursor sequence led to reduced overall growth, etching of 1,4-BDC, and a 1:1 stoichiometry. Spectroscopic ellipsometer (SE) was used to characterize the porosity, indicating irreversible structural changes during thermal treatment. Acetic acid modulation proved challenging, with Fourier Transform Infrared Spectroscopy (FTIR) confirming the presence of monodentate coordinated 1,4-BDC to zirconium.

QCM analysis of the Zr-BP-4,4-DC system revealed slower saturation of BP-4,4-DC compared to 1,4-BDC, revealing the necessity for extended pulse times to achieve saturation. Examination of the reaction mechanisms revealed a stoichiometry of 1:1 for Zr-BP-4,4-DC. Standard stable growth was achieved within 4 cycles for Zr-BP-4,4-DC on porous ZrO_2 film, while ZrO_2 deposition on Zr-BP-4,4-DC indicated sustained chemical activity of Zr-BP-4,4-DC after 200 cycles of ZrO_2 deposition. Pulsing water as part of the precursor sequence revealed the importance of a sufficiently long water purge for an effective water removal.

Acknowledgments

The master thesis project began in January 2022 and ended in November 2023. The work was carried out at the Nanostructures and Functional Materials group (NAFUMA) at the Department of Chemistry, Faculty of Mathematics and Natural Sciences at the University of Oslo (UiO).

I would like to express my gratitude to my main supervisor, Prof. Ola Nilsen, and co-supervisors, Prof. Steven Wilson and Prof. Stig Pedersen-Bjergaard. Ola, your passion for your craft has truly inspired me in this journey. Your ability to convey complex concepts and share your knowledge has greatly aided me in my role as a masters student. Beyond your support in completing this project, I value our insightful conversations. I am grateful for the advice you have provided about parenthood. I wish you and your family the best.

I would like to thank the Thin Film group, including Yani Leo Amedjkouh, Linn-Margrethe Rykkje, Bhagyesh Purohit, Veronica Killi, and a special thank you to Melania Rogowska. Melania, I appreciate your assistance throughout the project. Thank you for dedicating time from your busy schedule to aid me.

Thank you, Ali Haider Raja, for pushing me and reminding me to keep going. Your support is immeasurable. We have come far, but the journey has just begun. I would like to express my deepest gratitude to my parents for their endless support. This is as much your accomplishment as it is mine. To Ilyas Issa, I love you more than you will ever know. You are my greatest joy.

Finally, I would like to thank my wife Isabel Issa. You are the MVP. You have selflessly stood by me, provided a shoulder to lean on, and your unwavering love and support has meant the world to me. Thank you.

Abdinassir Hassan Issa

University of Oslo, November 2023

List of abbreviations

ALD	Atomic Layer Deposition
ANG	Adsorbed Natural Gas
BET	Brunauer-Emmett-Teller theory
CNG	Compressed Natural Gas
CVD	Chemical Vapor Deposition
DMF	Dimethylformamide
DRAMs	Dynamic Random Access Memories
EP	Ellipsometric Porosimetry
FCC	Face Centered Cubic
GC	Gas Chromatography
GPC	Growth Per Cycle
LC	Liquid Chromatography
MEMS	Micro-ElectroMechanical Systems
MOF	Metal Organic Frameworks
NAFUMA	NAnostrctures and FUnctional MAterials
NIR	Near-infrared
NMR	Nuclear Magnetic Resonance
PVD	Physical Vapor Deposition
QCM	Quartz Crystal Microbalance

QCR	Quartz Crystal Resonator
SE	Spectroscopic Ellipsometry
TLC	Thin layer Chromatography
UiO	University of Oslo
UV	Ultraviolet
UV-Vis	Ultraviolet-Visible
XRD	X-ray Diffraction
XRR	X-ray Reflectometry

Table of Contents

Abstract III

Aknowledgments VI

Abbreviations VIII

Table of Contents XII

1 Introduction 1
1.1 Motivation 1
1.2 Thesis Objective 1
1.3 Previous Work 2

2 Theory and Methods 3
2.1 Metal Organic Frameworks 3
2.1.1 Separation and Purification of Chemicals 5
2.1.2 Catalysis 7
2.1.3 Sensors 8
2.1.4 Gas Storage 8
2.1.5 Photoluminescence 10
2.2 UiO-66 and UiO-67 11
2.3 Synthesis 13
2.3.1 Atomic Layer Deposition 13
2.3.2 Optimizing ALD 14
2.3.2.1 Precursor Selection 14
2.3.2.2 Reaction Temperature 15
2.3.2.3 Pulse and Purge Time 16
2.4 Characterization 17
2.4.1 Quartz Crystal Microbalance 17
2.4.2 X-Ray Diffraction 17
2.4.3 Spectroscopic Ellipsometry 19
2.4.4 Fourier-Transform Infrared Spectroscopy 21
2.4.5 Ultraviolet-Visible Spectroscopy 21

3 Experimental 23
3.1 Atomic Layer Deposition 23
3.1.1 Reactor 23
3.1.2 Chemicals 25
3.1.3 Substrates 25
3.1.4 Parameters 26
3.2 Characterisation 27

3.2.1 Quartz Crystal Microbalance ... 27
3.2.2 X-Ray Diffraction ... 27
3.2.3 Precursor Tester ... 28
3.2.4 Spectroscopic Ellipsometer ... 28
3.2.5 Fourier-Transform Infrared Spectroscopy ... 30
3.2.6 UV-Vis Spectroscopy ... 30
3.2.7 Visual Tools ... 30

4 Results ... 31
4.1 Growth ... 31
4.1.1 ZrO_2 system ... 31
4.1.1.1 Analysis of growth dynamics by QCM ... 33
4.1.2 Zr-1,4-BDC system ... 37
4.1.2.1 Analysis of growth dynamics by QCM ... 38
4.1.2.2 QCM of Zr-1,4-BDC with water pulsing ... 41
4.1.3 Zr-BP-4,4-DC system ... 42
4.1.3.1 Analysis of growth dynamics by QCM ... 42
4.1.3.2 QCM of Zr-BP-4,4-DC with water pulsing ... 46
4.1.3.3 Porosity characterization by QCM ... 48
4.1.3.4 QCM of Zr-BP-4,4-DC with acetic acid pulsing ... 49
4.2 Characterization ... 50
4.2.1 XRD ... 50
4.2.2 Precursor Tester ... 51
4.2.3 SE ... 53
4.2.4 FTIR ... 55

5 Discussion ... 56
5.1 Growth ... 56
5.1.1 ZrO_2 System ... 56
5.1.2 Zr-1,4-BDC System ... 60
5.1.3 Zr-BP-4.4-DC System ... 62
5.2 Characterization ... 65

6 Conclusion ... 66

7 Future Work ... 67

8 Appendix ... 68
8.1 ZrO_2 system - Growth ... 68
8.2 Temperature log for the deposition campaign of the ZrO_2 system ... 69
8.3 Stoichiometry calculations ... 69
8.3.1 ZrO_2 system ... 69

8.3.1.1 Short QCM cycle of ZrO_2 growth 69
8.3.1.2 Long QCM cycle of ZrO_2 growth 70
8.3.2 Zr+1,4-BDC system 71
8.3.3 Zr+BP-4,4-DC system 72
8.4 Packing density calculations 72
8.5 Capping of Zr-BP-4,4-DC with ZrO_2 75
8.6 Stoichiometry calculation for Zr-1,4-BDC with water pulsing 75
8.7 Characterization 76
8.7.1 UV-Vis of Zr-1,4-BDC 76

References 77

1 Introduction

1.1 Motivation

Throughout the evolution of technology, from its earliest iterations to its most advanced forms, technological development has thoroughly shaped the way we experience the world. Material technology stands prominently at the forefront of these technological advancements. The purpose and objective of material technology is to synthesize materials with a specific set of properties that best meet the requirements of its application. The desired application can be achieved by employing various synthesis and characterization methods such as Atomic Layer Deposition (ALD) and X-Ray Diffraction (XRD) [1, 2]. Over the years, these methods have undergone significant development, reaching a stage where precise control over the thickness of thin films at the atomic level and the discovery of information about the arrangement of atoms within a crystal are now possible. This opens up possibilities for synthesizing materials that host a wide range of applications [3, 2].

This has paved the way for research into Metal Organic Frameworks (MOFs), a class of compounds that exhibit remarkable pore tunability, making them particularly functional for catalysis applications and processes [4]. Additionally, MOFs can be used for the separation and purification of chemicals by fine-tuning their structural, optical, electrical, and magnetic properties [5, 6], possibly contributing to a reduction in the 10-15% of global energy consumption that is allocated to chemical separation processes [7]. MOFs such as UiO-66 and UiO-67 have been investigated for various applications, including the separation of chemicals [8]. Nevertheless, there is a need to delve into challenges associated with the thermal stability and synthesis conditions of the systems in order to bridge the gap between theoretical understanding and practical applications [9, 10].

1.2 Thesis Objective

The aim of this thesis is to develop porous coatings for chromatography enhanced sensors. The method of choice for the deposition process is ALD. Thin films can be synthesized by other methods such as Physical Vapor Deposition (PVD) and Chemical Vapor Deposition (CVD), however, these methods do not offer equivalent precision and control during synthesis [11]. The ALD approach for the deposition of organic-inorganic hybrid materials offers a great deal of flexibility with regard to the metal oxide and organic linker molecules, whilst allowing exceptional control of the porosity and chemistry of the film.

This project will be carried out in a step-wise manner, with an initial focus on characterizing the growth of ZrO_2 ($ZrCl_4$+H_2O), Zr-1,4-BDC ($ZrCl_4$+1,4-BDC), and Zr-BP-4,4-DC ($ZrCl_4$+BP-4,4-DC) by using the ALD technique. This will be combined with characterization and complimentary methods such as Quartz Crystal Microbalance (QCM), Spectroscopic Ellipsometry (SE), XRD, Ultraviolet–visible spectroscopy (UV-Vis), and Fourier Transform Infrared Spectroscopy (FTIR). This will be followed by the characterization of the evolution of the films porosity using SE equipped with an environmental chamber.

1.3 Previous Work

Extensive research has been conducted to investigate the diverse characteristics and properties of UiO-66 (Zr-1,4-BDC), UiO-67 (Zr-BP-4,4-DC), and their derivatives. Cavka *et al.* demonstrated that it is neither the length of the linker molecule nor the covalent bond between the secondary building unit and the linker that compromise the stability of material [12]. Rather it is the carbon-carbon bond between the carboxylate carbon and the benzene ring. Similarly, an uptake of water vapor isotherm at 25 °C, 90% relative humidity, reduced the BET surface area of UiO-67 from 2145 m^2 g^{-1} to 10 m^2 g^{-1} [13]. Mondloch *et al.* owed this reduction in surface area to improper activation (solvent removal from porous framework) [14]. Activation of UiO-67 from water indicated complete loss of porosity, whereas solvent-exchange to acetone resulted in retained porosity. It was thus proposed that the instability was due to capillary-force-driven collapse. Capillary force-driven collapse, a phenomenon commonly observed in porous materials, occurs as a consequence of a reduction in volume exerted by a fluid. Owing to the interconnected pores of UiO-67, a reduction in the volume of local pores extends throughout the network [14].

The structural integrity and chemical stability was investigated by observing the material's behavior when exposed to different environmental conditions. Recent studies on the structural stability of UiO-66 in various environments including exposure to Dimethylformamide (DMF), water, air, and chloroform was analyzed over the course of a year at room temperature [15]. UiO-66 exhibited structural resilience when exposed to water, air, and chloroform. However, when exposed to DMF, XRD data confirmed partial structural degradation. Exposure to DMF, water, air, and chloroform resulted in a surface area reduction of 30.6%, 21.9%, 10.3%, and 14.2%, respectively [16].

Various approaches for converting Zr-1,4-BDC into crystalline UiO-66 using acetic acid have been explored. Lausund *et al.* experimented with incorporating acetic acid modulation during the deposition process [17]. However, this led to acetic acid altering the bonding scheme of the 1,4-BDC linker from monodentate to bidentate coordination to zirconium. They determined that crystalline UiO-66 could be successfully synthesized by autoclave treatment at 160 °C for 24 hours in acetic acid vapor. Lan *et al.* also converted Zr-1,4-BDC to crystalline UiO-66 using a similar procedure to Lausund *et al.*, but with a few modifications [18]. They pre-heated a 500 mL Teflon vessel and Zr-1,4-BDC coated blade or arrow for 10 minutes, followed by the subsequent transfer of 4 mL acetic acid into a Teflon vessel that was sealed for 23 hours. They determined that a too small acetic acid volume ($<$4 mL) and too short conversion time ($<$21 h) led to incomplete conversion of Zr-1,4-BDC to crystalline UiO-66 film. Buzek *et al.* investigated the stability of UiO-66 and its pH dependence as a catalysts for degradation of organophosphate toxic compounds [19]. They determined that Powder XRD analysis, following potentiometric titration of UiO-66 suspension in an aqueous solution with pH values ranging from 3 to more than 11, revealed a reduction in the surface area of UiO-66 from 1391 m^2g^{-1} to 1283 m^2g^{-1} at pH 8.5 and complete structure collapse at pH 9.5 and above. In summary, the existing literature provides valuable insights into the stability, synthesis, and environmental behavior of UiO-66, UiO-67, and their derivatives.

2 Theory and Methods

This section of the report establishes the foundation that underpins the experimental, theoretical and analytical aspects of the report.

2.1 Metal Organic Frameworks

MOF are a subclass of coordination polymers that are composed of inorganic secondary building units and organic linker molecules that form one-, two-, or three-dimensional structures [20]. The secondary building units compromise a metal ion or a cluster of metal ions such as Zr(IV), Cu(II) and Zn(II) as well as lanthanides and rare earth elements. Combined with the organic linker molecules that are generally monovalent, divalent, trivalent or tetravalent ligands, the size and the shape of MOF can be meticulously controlled [21, 22]. MOF's are characterised by their high surface area and porosity which makes them useful for several applications [23–27]. Examples of MOF's include UiO-66, UiO-67, and UiO-68 (see Figure 2.1), which are three MOFs that differ in linker length, affecting porosity and functionality.

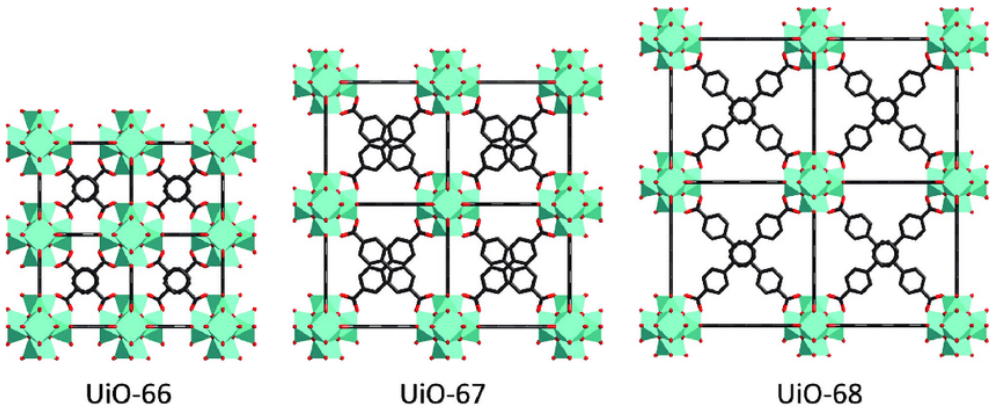

Figure 2.1: Crystal structures showing the difference in the length of the linker as well as the porosity between UiO-66 (left), UiO-67 (center), and UiO-68 (right). Obtained from [28].

Synthesis of MOFs with uniform properties and stoichiometry has been a formidable challenge, with instability concerns such as framework collapse being a major issue. In 1999, Li *et al.* conducted synthesis of MOF-5 and identified specific cavities within its framework [29]. The dimensions of these cavities presented challenges owing to their size, leading to reproducibility and stability issues. Through meticulous experimentation and analysis, Li *et al.* achieved reproducibility and stability through the use of an organic dicarboxylate linker, leading to the synthesis of clusters within a three-dimensional framework. This groundbreaking approach to MOF synthesis laid the foundation for the future advancement in the field of MOFs [29]. At present, MOFs stand out as distinctive materials owing to their extraordinary porosity and exceptional stability [30, 31]. MOFs

exhibit remarkable stability by preserving their structure and properties amid changing conditions such as temperature, pressure, and chemical environment. This resilience is fundamental for their utility in practical applications. Concurrently, their remarkable porosity, defined by the spaces between their constituent atoms, adds another layer of versatility. MOFs exhibit varying porosity, ranging in depth and diameter from the nanometer to the micrometer scale. Such materials are commonly categorized as macroporous, mesoporous and microporous.

Macroporous materials feature pores with a diameter exceeding 50 nm, mesoporous materials have pores ranging between 2 nm and 50 nm in diameter, and microporous materials feature pores with a diameter less than 2 nm [32]. Porous materials consist voids that can be either isolated or interconnected to different degrees. Consequently, porous materials enable fluids to enter, exit, and/or flow within the isolated or interconnected voids. The permeability of voids in porous materials is influenced by several factors, such as chemical composition, pore arrangement, overall porosity, roughness of the internal void surface, among others [32]. Porous MOFs have been extensively studied and used for various applications [33, 34]. The large surface area of these materials provide both adsorption and storage capabilities. Coupled with their low density, these materials provide an excellent framework for applications such as catalysis and gas storage [4, 35]. Figure 2.2 shows how the porosity of MOF's changes when the linker molecules are different.

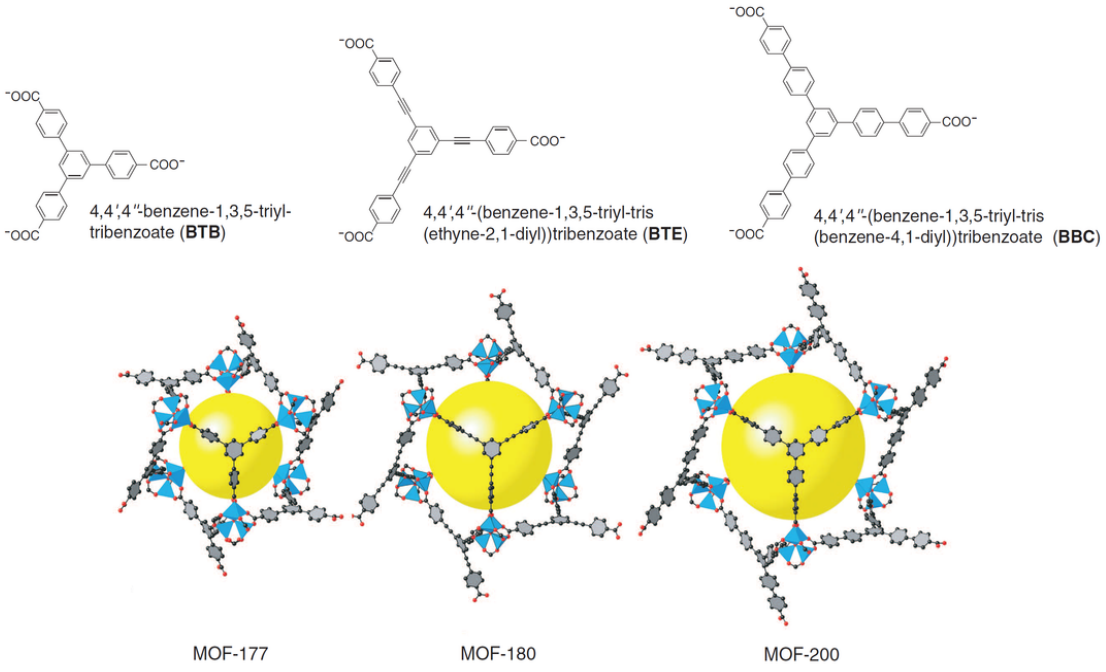

Figure 2.2: Crystal structures illustrating the increase in porosity from MOF-177 (left) to MOF-180 (middle), and MOF-200 (right), with their respective linkers shown above. Obtained from [36].

The increase in the length of the linker molecules, from MOF-177 to MOF-200, resulted in an increase in porosity from an initial 83% to 90%, which provides enhanced storage capacity for gas storage applications, whilst preserving the fundamental properties of the original MOF [36, 37]. The following sections provide a brief overview of potential applications of MOFs, with a focus on separation of chemicals as the main motivating application.

2.1.1 Separation and Purification of Chemicals

Chemists allocate significant resources, including time and money, to implement the separation of chemical mixtures. Chemical separation is a necessary procedure that is carried out to acquire specific chemicals at the desired level of purity. Such procedures, which are often labor-intensive and energy-ineffective, contribute to substantial operational costs that could otherwise be allocated towards alternative areas such as research and development. At present, approximately 10-15% of the world's energy consumption is dedicated to the separation of chemicals [7]. Any technology or method that is capable of improving current procedures by any margin would offer major benefits from an economic and environmental viewpoint. A major challenge in the petrochemical industry is the separation of benzene derivatives and cyclohexane due to their almost indistinguishable physical properties [38]. Extractive distillation, which utilizes a miscible, high boiling and relatively non-volatile solvent, serves as the main method for achieving such a separation [39]. This process often involves complex processes that constitute high energy and operating costs [38]. An alternative solution to distillation lies in the development of adsorbents with specific chemical and physical properties. MOFs, which can be synthesized with varying structural, optical, electrical and magnetic properties, could be used to adsorb and separate chemicals by various mechanisms. This includes separation of chemicals driven by the differences in affinities of chemicals towards an adsorbent. Separation can also be achieved by exploiting the differences in size between chemicals, such as benzene and cyclohexane derivatives [38]. In this manner, porous MOFs can be utilized to retain specific molecules while allowing others to pass through in a manner similar to molecular sieving [40].

Chromatography is an analytical technique that enables the identification, purification, and separation of a mixture's constituents by enabling separation according to physical or chemical properties [41]. Such a technique, which can provide both qualitative and quantitative data, enables separation of components according to molecular characteristics such as size, shape, charge, and binding energy [42]. Chromatography is based on the principle of separating components into constituents by exploiting the variations in their interaction with a stationary and mobile phase. The three components that constitute such a technique include the stationary phase, mobile phase and mixture. The stationary phase is the immobile material, often a solid or a liquid that is deposited on the surface of a solid support. It serves to retain components of a mixture, according to factors such as polarity and affinity, as the mixture traverses the system. The mixture is carried along the

stationary phase by a liquid or gas known as the mobile phase, serving as a means of transportation of the mixture through the stationary phase [42]. As aforementioned, separation can be achieved according to the difference in size between the components of a mixture [41]. Crystalline MOFs with well defined pore sizes and volume can serve as the stationary phase in such a technique. In such a system, separation is based on the adsorption and retention of certain molecules with dimensions similar to pores and exclusion of molecules with dimensions larger than pores [43]. UiO-66 and UiO-67, featuring both tetrahedral and octahedral pores that vary in size, may be rendered suitable for such an application [44].

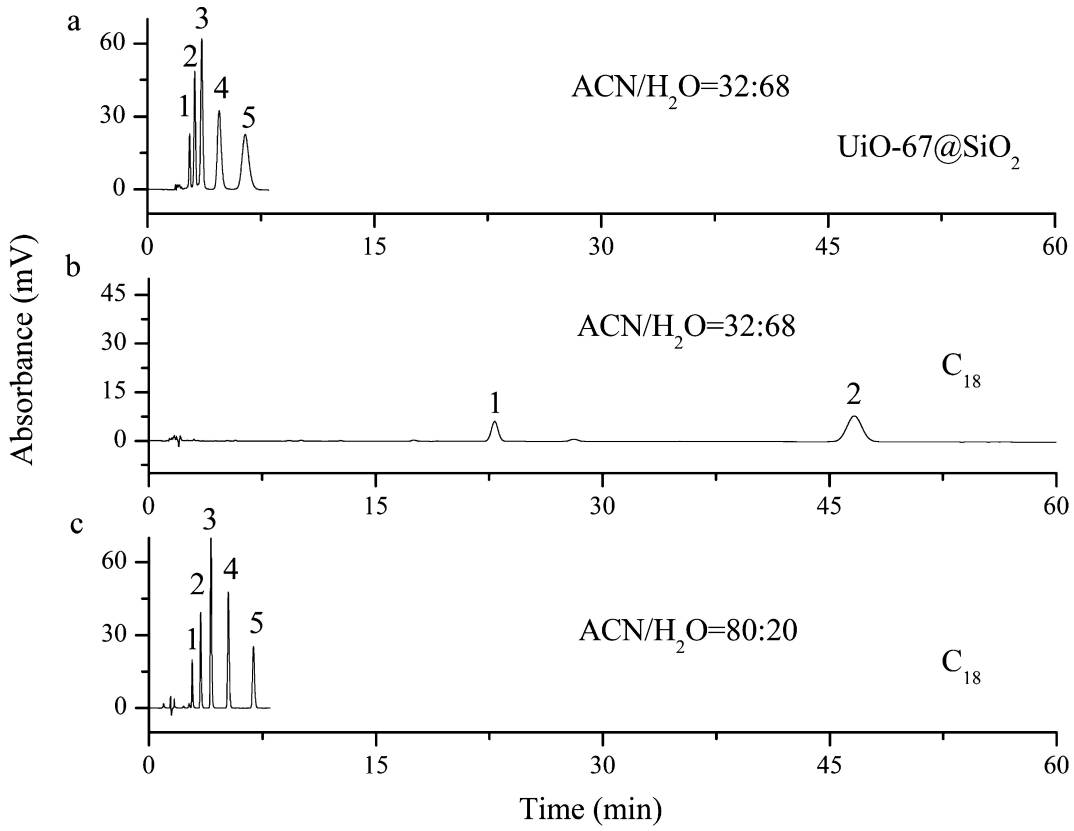

Figure 2.3: Chromatographic performance test of UiO-67@SiO_2 (a) and C_{18} (b,c) columns for separation of hydrophobic alkylbenzene compounds. Analytes: 1, benzene; 2, methylbenzene; 3. ethylbenzene; 4, propylbenzene; 5, butylbenzene. UiO-67@SiO_2 shows superior baseline separation than C_{18} at eluent concentration of 32% ACN/68%$_2$O and similar baseline separation to C_{18} (80% ACN/20%$_2$O). Obtained from [45].

The extensive possible combinations between inorganic metal cores and organic ligands enables the synthesis of MOFs with diverse physical and chemical properties that are tailored for the separation of specific chemicals. Although research indicates that MOFs offer a promising alternative to

existing separation methods [46], significant challenges persist in the application of MOFs for chemical separation, such as challenges pertaining to the reusability of MOFs. Microporous adsorbents exhibit a strong interaction between the adsorbate and adsorbent due to their high degree of confinement. Challenges related to the desorption of adsorbates from active sites without causing damage to both the adsorbate and the active site persist [40]. While various desorption mechanisms, such as thermal desorption, chemical- or radiation-stimulated desorption, can be employed, the full potential of MOFs in separating molecules will be realized once an improved balance between maximum selectivity and minimum regenerative energy requirements is met.

2.1.2 Catalysis

Industrial chemical processes that require chemical transformations rely heavily on catalysts. Catalysts offer the advantage of reducing costs by lowering energy requirements and ensuring environmental sustainability by reducing waste generated during manufacturing processes [47]. MOFs emerge as a compelling choice for heterogeneous catalysis, possessing substantially greater potential for industrial applications compared to homogeneous catalysis. MOFs offer unprecedented tunability of parameters such as pore dimensions. Development in the accuracy of tools to tune pore dimensions, as well as the advancement in in-situ characterization methods, has allowed development and incorporation of complex catalysts that can be utilized for encapsulation purposes [48–50]. MOFs can host a wide range of active sites by encapsulating active species in pores, furthering the notion that catalytically functionalized MOFs constitute immense unrealized potential [51]. Functionalization can be achieved or enhanced through pre- and/or post-synthetic modifications that give rise to properties that would be challenging to achieve using conventional methods [47].

MOFs, however, have some challenges in catalysis such as stability concerns and low catalytic activity [52]. Stability issues often arise as a consequence of organic linker degradation under certain reaction conditions, possibly leading to framework collapse. It is crucial to address such a concern as it can hinder both performance and application. Degradation of the organic linker may limit the reusability of MOFs as catalysts, potentially resulting in increased costs and waste generation. Furthermore, MOFs, depending on the combination of organic linker and metal ions, may exhibit low catalytic activity due to weak interactions, pore blockage, and restricted accessibility to active sites within the framework [52]. Fortunately, such challenge can be mitigated and potentially overcome through pre- and/or post-synthetic modifications [47].

2.1.3 Sensors

A sensor is a device that detects and responds to an input or information from its environment or surroundings. Sensors are primarily composed of two units. The sensing unit, responsible for detecting information, and the transduction unit, responsible for converting the detected signal into another form of signal [53]. This can include the detection and transduction of mechanical, optical, electrical and photophysical energy [54]. The development of sensing materials that not only fulfill the aforementioned prerequisites but also offer high selectivity, sensitivity, stability, and rapid response times has lead to an interest in MOFs. MOFs are renowned for their tunable chemical properties, as well as their structural diversity, which makes them ideal sensing units for chromatography enhanced sensors [53]. MOFs, which are composed of a rigid inorganic core surrounded by flexible organic ligands, can be synthesized with varying structural, optical, electrical and magnetic properties by selecting a suitable combination of inorganic core and organic ligand. This offers a solution that meets the precise demands of modern sensing technologies. In order to sustain industrial development and population growth, advanced and improved sensors are needed especially in the agricultural, mining, and forestry sectors [55–57]. Modern sensors have played a key role in providing vital information; however, issues with modern sensors include the use of expensive equipment, difficulty of use and slow result acquisition [58]. Consequently, new sensing technologies that require cheaper equipment, are easier to use, and have the capability for real-time and continuous data acquisition are a requisite for the contemporary climate.

2.1.4 Gas Storage

Several critical industrial and societal processes, including transportation, energy generation, heating, and manufacturing, heavily depend on gas storage [59, 60]. Gas storage plays a vital role in ensuring the safe and effective facilitation of a steady and consistent supply of energy. Without the capacity to store gases, challenges in balancing the supply and demand of gases, leading to potential energy shortages and disruptions in various sectors of society, would become prevalent. Research indicates that MOFs provide a promising alternative to conventional means of storing gas [61]. The high surface area and adsorption capacities of MOFs can be utilised to adsorb gas molecules within a small volume at a reduced pressure. This becomes advantageous when storing low volumetric energy-dense gases like methane, which is the primary component of natural gas for electricity generation and heating [62]. Figure 2.4 illustrates the improved volumetric storage capacity achieved at different pressures when gas is adsorbed, as opposed to compressed.

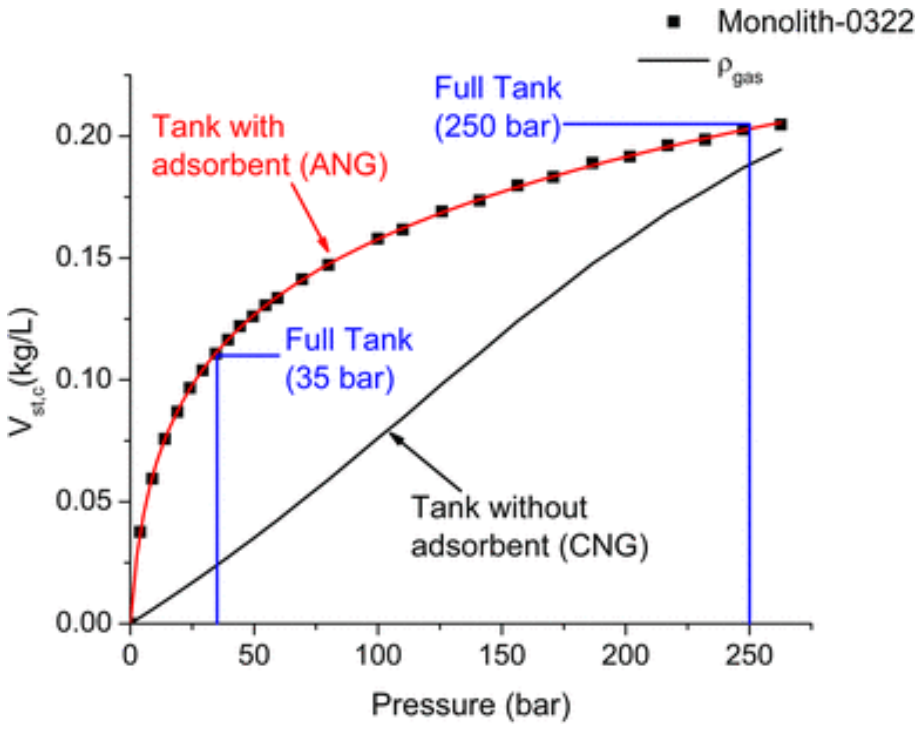

Figure 2.4: Graph illustrating the relationship between volumetric storage capacity and pressure at 23 °C, highlighting enhanced volumetric storage capacity of Adsorbed Natural Gas (ANG) over Compressed Natural Gas (CNG) achieved through the adsorption of gas onto a carbon monolith. Obtained from [63].

Another benefit of MOFs lies in the capability to synthesize amino-functionalized Zr(IV)-based MOFs with high physicochemical stability, a feature that would allow the use of MOFs for high-pressure gas storage [64]. MOFs can display stable gas storage and release over a broad range of temperatures and pressures. The safe and efficient storage of gas is paramount, given the potential risk associated with leaks or accidents, especially in systems involving high pressures of compressed gas storage. While MOFs show great promise for gas storage applications, several challenges include scalability of synthesis and cost of synthesis [65]. The difficulty in scaling up MOF synthesis for practical applications stems from challenges related to maintaining consistency and ensuring reproducibility. The economic viability of MOFs is significantly affected by the challenges of scaling up, as even slight parameter variations can lead to the production of materials that exhibit unintended and possibly unexpected properties.

2.1.5 Photoluminescence

Photoluminescence is the spontaneous emission of light, known as luminescence, from matter as a result photoexcitation. This includes phosphorescence and fluorescence, which are emission phenomena utilized in various applications, such as detecting environmental pollutants and in imaging within surgical and radiological disciplines [66, 67]. MOFs can be employed as luminescent materials by incorporating luminescent metal ions or conjugated/aromatic linker molecules that readily luminesce [68]. In such a system, the luminescent properties arise from electronic transitions that occur within the π-conjugated framework. The interaction between the guest species and framework renders MOFs an excellent candidate for use as a sensor material. The framework of MOFs can provide a number of interaction sites, which provides enhanced detection sensitivity. Combined with the capability to tune the chemical properties and structural framework, MOFs have the potential as sensor materials with high sensitivity and selectivity. Furthermore, luminescent MOFs can be synthesized by introducing guest species such as organic dyes that selectively adsorb onto the porous framework of MOFs through electrostatic interactions [69]. The use of luminescent MOFs as biosensors for detection and quantification purposes has been an area of research that has received a great deal of attention [67, 70, 71].

2.2 UiO-66 and UiO-67

UiO-66 and UiO-67 contain a zirconium metal center ($Zr_6O_4(OH)_4$), which act as secondary building units within the structural framework. The building unit for UiO-66 is linked together by 1,4-BDC, while BP-4,4-DC serves as the organic linker for UiO-67 [72]. These linkers connect the nodes, creating the extended lattice structure of the materials. The materials have a face-centered cubic (FCC) structure in which Zr nodes are octahedrally coordinated by oxygen atoms from the organic linker molecules to form a metal center ($Zr_6O_4(OH)_4$) [73, 74]. The metal centers are further connected to 12 neighbouring organic linkers to form the crystal structure [16]. UiO-66 and UiO-67 have two types of pores within their structural framework, comprising tetrahedral and octahedral pores [44].

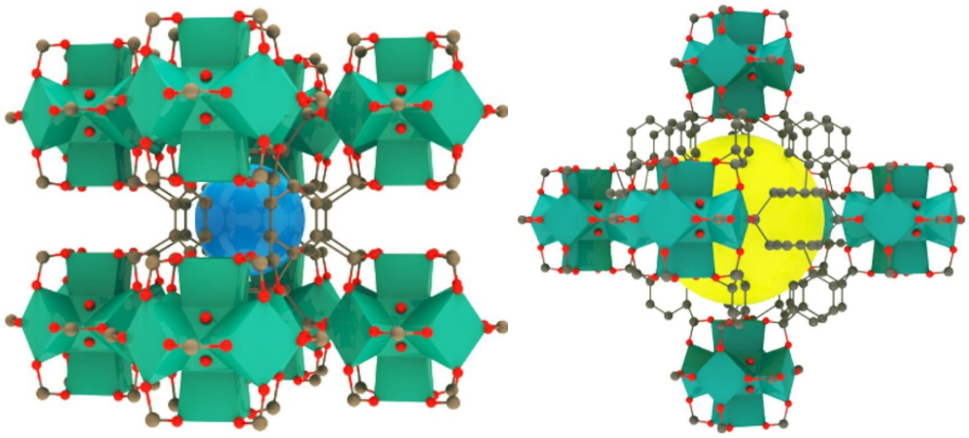

Figure 2.5: Illustration of the crystal structure of UiO-66 showing a tetrahedral (left) and octahedral (right) void, represented by the blue and yellow spheres, respectively. Adapted from [16].

The primary obstacle that poses a significant challenge for the practical application of crystalline MOFs and porous films like UiO-66 and UiO-67 is the synthesis method. For instance, conventional methods, such as solvent-based methods like solvothermal synthesis, are not suitable for implementing UiO-66 in microelectronic due to the lack control over the deposition process [10, 32]. ALD offers numerous advantages including a higher degree of precision. The overarching benefit of improving the method is the capacity to synthesise materials with unique properties and versatile functional applications, as illustrated in Figure 2.6.

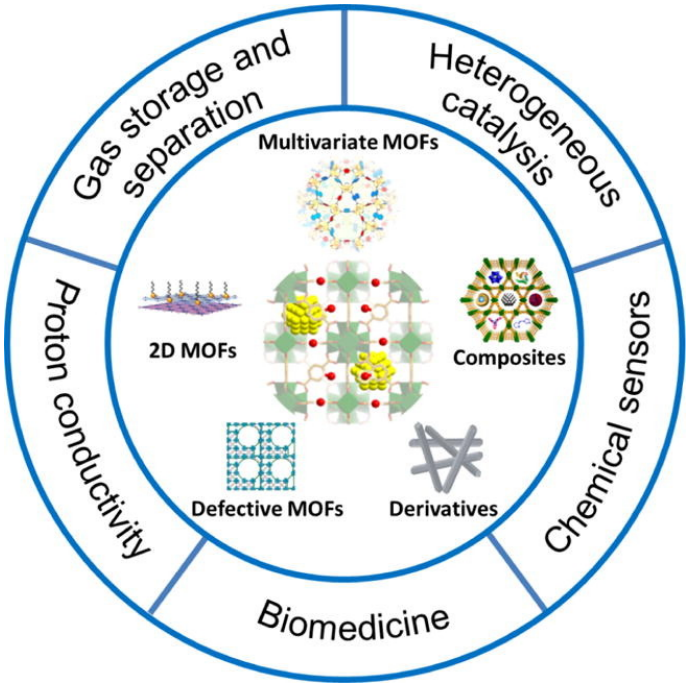

Figure 2.6: Illustration of the highly versatile functional application of MOFs. Obtained from [75].

Controlled synthesis of UiO-66, UiO-67, and its derivatives such as UiO-67-Me and UiO-67-BN, which are based on 3,3'-dimethylbyphenyl and 1,1'-binaphthyl linker molecules, respectively, offer excellent stability to water and volumetric adsorption capacity for hydrocarbons such as benzene, an organic chemical that is extensively used as an industrial solvent [76]. Moreover, UiO-67 can be doped to exhibit photophysical properties such as luminescence vapochromism [77]. The large internal surface area of UiO-67 can be utilized in sensors as an application to separate volatile organic compounds [78]. Despite the potential applications of UiO-66 and UiO-67, challenges related to thermal stability and synthesis method highlight the necessity for additional research on these materials.

2.3 Synthesis

2.3.1 Atomic Layer Deposition

ALD was first introduced in the 1960s by Stanislav Koltsov and co, [79]. During the development of thin-film electrolumiescent displays, Dr. Tuomo Suntola devised ALD, formerly named molecular layering, as an advanced thin-film technology naming the technique Atomic Layer Epitaxy (ALE) [80]. The introduction of ALE technology for semiconductor applications lead to Dr. Tuomo Suntola being awarded the European SEMI award the Millennium technology price *"Honoring the Pioneer in Atomic Layer Deposition Techniques ... that paved the way for the development of nanoscale semiconductor devices"* in 2004 at the Munich Electronics Show [80]. From that point forward, ALE, revised to the widely adopted term ALD, has been widely employed for synthesizing thin films. ALD has a multitude of applications within industry and research including Micro-electromechanical systems (MEMS), Li-ion batteries, solar and nano cells, Dynamic random access memories (DRAMs), and more [81–84].

ALD is characterised by its precise control of growth of coatings on the surface of a substrate, enabling meticulous control of the films thickness and composition at the atomic level [32]. It is a self-limiting technique, as film growth relies on precursor adsorption to the substrate through a sequence of self-saturating surface reactions. The process of ALD involves exposing the surface of a substrate to alternating precursors that are introduced into the reaction chamber in a sequential manner. As such, the process is carried in pressures ranging from 0.1 mbar to 10 mbar. In contrast to CVD methods, where reactant gases are simultaneously introduced into the reaction chamber, potentially causing uncontrolled film growth, ALD precursors are separately and sequentially pulsed into the reaction chamber. Thus, controlled layer-by-layer film growth on a substrate is achieved. Unadsorbed precursor molecules are purged out using an inert gas, and the process is repeated [32]. The cyclic process, which is separated into two half-cycles, is illustrated in Figure 2.7.

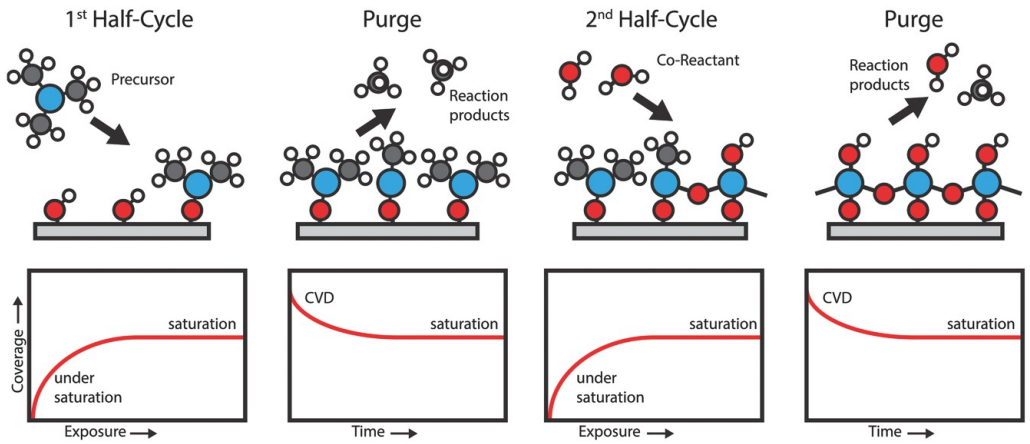

Figure 2.7: Illustration of ALD half-cycles highlighting the sequential pulsing of precursor molecules into the reaction chamber and the corresponding growth. Obtained from [85].

The first step comprises pulsing the first precursor into the reaction chamber. This results in the precursor reacting with and adsorbing onto the surface of the substrate, leading to saturation. This saturated layer serves as the first layer of the film. In the subsequent step, the reaction chamber is purged with an inert carrier gas to remove any surplus precursor that is in the reaction chamber and the byproducts from the surface reactions. This step aims to prevent gas-phase reactions between the precursors, marking the completion of the first half-cycle. In the second half-cycle, the third step entails pulsing the second precursor into the reaction chamber, where it reacts with the adsorbed precursor on the surface of the substrate to saturation. The fourth step entails purging the reaction chamber to flush both the second precursor and byproducts. This approach of exposing the surface to alternating precursors for a specific duration ensures self-limiting film growth [32]. As the precursors do not react with themselves or decompose, the thickness of each monolayer is precisely controlled with every pulse.

2.3.2 Optimizing ALD

2.3.2.1 Precursor Selection

The precursors should either possess a low sublimation temperature or high vapor pressure, allowing them to be introduced into the reaction chamber in gaseous form [86]. Additionally, the precursor must remain thermally stable under the given conditions to prevent thermal decomposition and unintended reactions from occurring. Precursors should have high purity to prevent contaminants from affecting the properties of the film. Furthermore, the byproducts of the precursors should be chemically inert to prevent the formation of compounds that could affect the films composition and thus, properties [86].

2.3.2.2 Reaction Temperature

Achieving controlled growth in ALD is crucial as it ensures the uniform and precise deposition of film with a consistent thickness and composition, both of which significantly influence the films properties. Controlled growth can be achieved by selecting the appropriate reaction temperature. To ensure that consistent film thickness is achieved in each cycle, the growth per cycle (GPC) needs to remain relatively constant. This is accomplished by choosing a reaction temperature within the ALD-window, as illustrated in Figure 2.8.

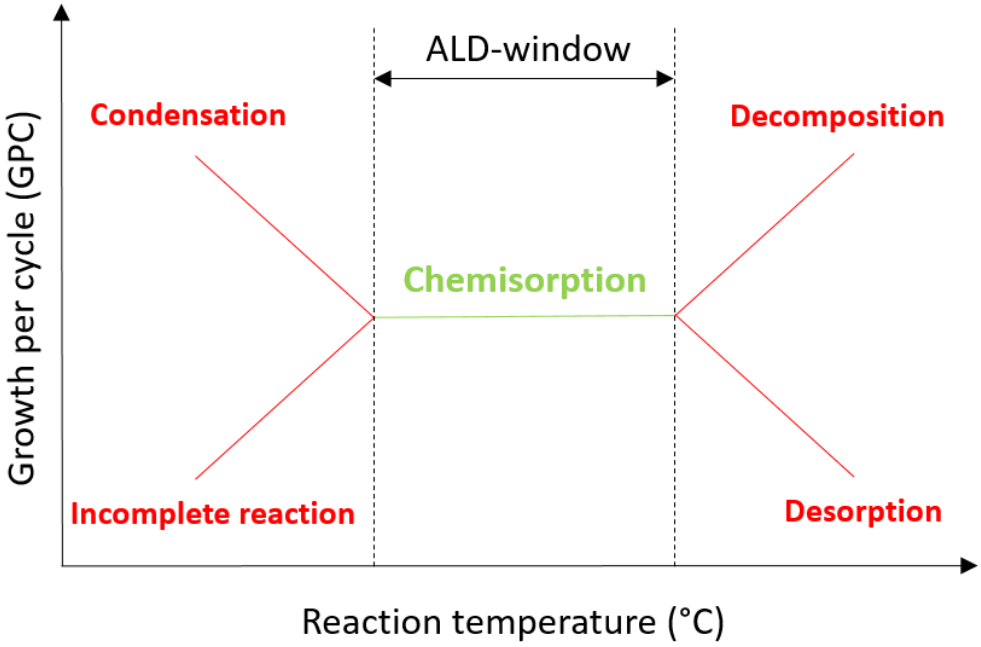

Figure 2.8: Schematic illustration of growth per cycle against reaction temperature. The temperature at which the growth rate remains unaffected by the temperature is the ALD-window (green). At temperatures below and above the ALD-window, condensation, incomplete reaction, decomposition, and desorption (red) occur. Inspired by [87].

The ALD window refers to the temperature range where the growth rate is unaffected by the reaction temperature [88]. Within this temperature range, chemisorption, a process in which molecules or atoms adhere to the surface of the substrate through chemical bonds, takes place. A reaction temperature that is too high can result in desorption, where uncontrolled growth on the surface leads to weakened interaction between the precursors and surface of the substrate, or decomposition, where precursors thermally decompose on the surface of the substrate. A reaction temperature that is too low may lead to incomplete reaction between a precursor and the substrate, due to insufficient thermal energy for surface reactions, or condensation, where physisorption takes

place, leading to weak interactions between the precursors and the substrate [88]. As depicted in Figure 2.8, the ALD-window spans a temperature range, ensuring that fluctuations within the reaction chamber do not lead to uncontrolled growth.

2.3.2.3 Pulse and Purge Time

In addition to the selection of a suitable reaction temperature, the precursor pulse and purge times are parameters that significantly influence the film growth process. A pulse time that is too short might not allow adequate time for the precursor to completely saturate the surface, while a pulse time that is too long could lead to over-saturation [86]. In either case, uneven or incomplete film growth should be expected. Over pulsing is preferred over under pulsing, as any excess precursor may be effectively removed from the reaction chamber during the subsequent purging process. Figure 2.9.a. shows a system with only chemisorption and Figure 2.9.b. shows a system with both chemisorption and physisorption.

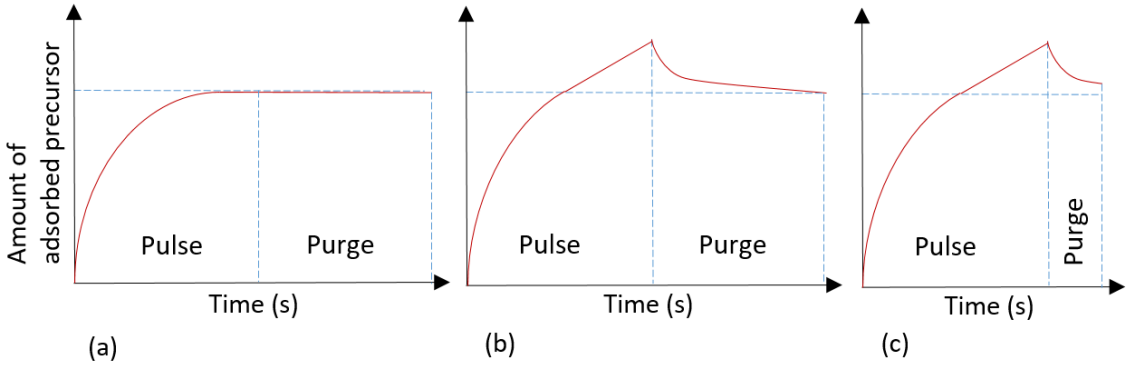

Figure 2.9: Schematic illustration displaying the variation in adsorbed precursor over time in (a) a self-limiting growth system, (b) a system involving both chemisorption and physisorption, and (c) a system with an insufficient purge time. Inspired by [17].

In systems (a)-(c), the pulse time is longer than necessary. Despite this, Figure 2.9.a. indicates that the amount of adsorbed precursor remains constant for a system that undergoes only chemisorption, regardless of the excess pulse time. In this type of system, film growth is self-limiting. The thickness of the film increases uniformly with each consecutive cycle, providing significant control over the films properties. Figure 2.9.b highlights the importance of a sufficient purge time in systems that undergo both chemisorption and physisorption. In this particular system, the purge time is sufficient to flush any physisorbed molecules from the film. A purge time that is too short, Figure 2.9.c, may result in excess precursor molecules remaining adsorbed on the surface, leading to non-uniform growth.

2.4 Characterization

2.4.1 Quartz Crystal Microbalance

QCM is an in-situ technique that is used to characterize the growth mechanism of deposited film [89]. It functions as a highly sensitive mass balance that can measure incremental changes in mass in the nanogram range, enabling detailed analysis of the films growth process. This technique involves applying an alternating electric field, via metal electrodes, to quartz crystals, which are made of piezoelectric material. The applied electric field induces oscillations in the the quartz crystals at a specific frequency. This oscillation frequency is highly sensitive to alterations in mass on the surface of the crystal, allowing real time analysis of the deposition rate, films growth, and adsorption behavior [89]. The use of this technique facilitates modifications to the ALD process, ensuring the synthesis of the desired film with the desired characteristics.

In QCM, the Sauerbrey equation, Equation 2.1, is used to relate the change in mass, Δm, to the frequency change, Δf.

$$\Delta f = -\frac{2 \times f_0^2 \times \Delta m}{A \times \sqrt{\rho_q}} \tag{2.1}$$

Where Δf is the change in frequency (Hz), f_0 is the resonant frequency of the crystal (Hz), Δm is the change in mass (g), A is the crystal area (cm^2), and ρ_q is the density of crystal (g/cm^3).

2.4.2 X-Ray Diffraction

XRD is an analytical technique that is used to obtain microstructural information about the structural properties of crystalline materials. This characterization method uses high-energy X-ray beams, a form of electromagnetic radiation that is characterized by its wavelength and energy, to interact with the crystal lattice of a material [90]. The interaction between the high-energy X-ray beam and the crystal lattice of a material provides microstructural information that is based on the arrangement of the atoms within the crystalline material. In XRD, diffraction of the incident beam is observed. Diffraction occurs when X-rays interact with the periodically arranged atoms, leading to the scattering of X-ray waves. Depending on the spacing between the atomic planes of the crystal and the angle of incidence, the diffracted X-rays can either cancel each other out (destructive interference) or reinforce each other (constructive interference).

Destructive interference is observed when the diffracted beams from parallel crystal planes align such that the phase difference between the parallel beams is equal to an integer plus half of the wavelength, $n + \frac{1}{2}\lambda$. Constructive interference is observed when diffracted beams from parallel crystal planes have a phase difference of $n\lambda$. By scanning the sample across a range of diffraction angles, typically 5°-70° and measuring the relative intensity of diffracted X-rays, a diffractogram is obtained [90]. This can be understood in terms of Bragg's law, depicted in Equation 2.2.

$$n\lambda = 2dsin\theta \tag{2.2}$$

Where n is a positive integer, λ is the wavelength of the incident X-ray beam, d is the atomic spacing between planes of a crystal, and θ is the incident and scattering angle. A schematic illustrating Bragg's law is presented in Figure 2.10.

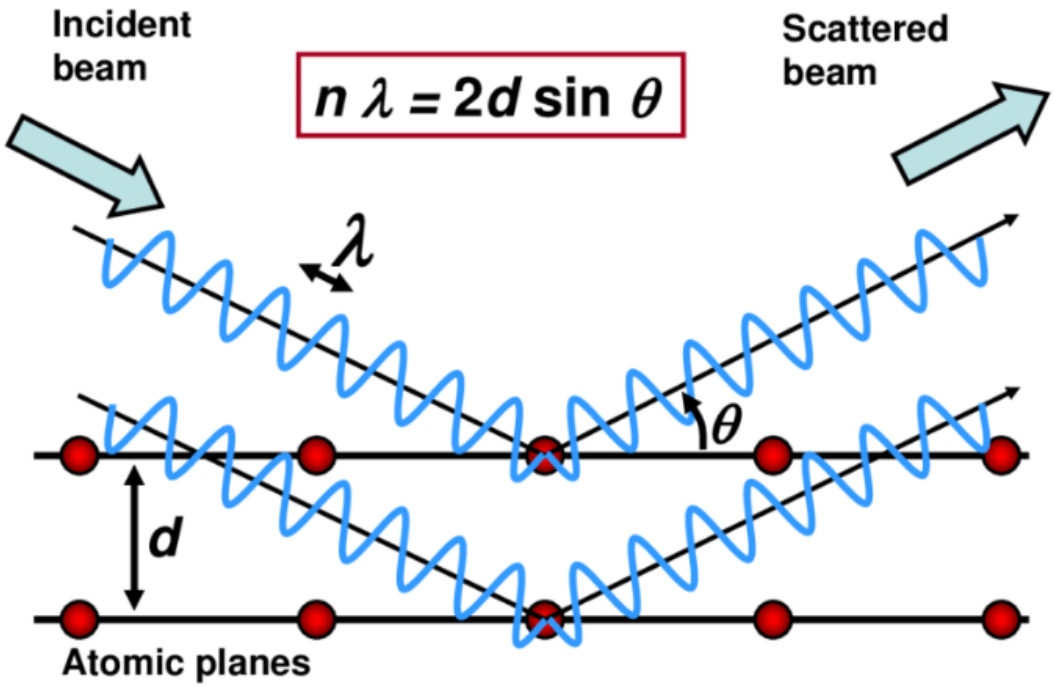

Figure 2.10: A schematic illustrating X-ray diffraction according to Bragg's law showing the wavelength of the incident X-ray beam, λ, the atomic spacing between the planes, d, and the scattering angle, θ. Obtained from [91].

Samples that diffract constructively produce characteristic X-ray peaks in the X-ray diffractogram. The diffractogram shows the intensity of the peaks at various angles, providing information about the crystal structure of the sample. Analysis of the XRD spectrum of crystalline materials is relatively simple, owing to the sharp and distinct peaks that are easily distinguished and characterized. Samples that diffract destructively do not produce characteristic X-ray peaks in the diffractogram. This indicates that there is a lack of long-range order in the sample [90]. Such samples are amorphous. Analysis of amorphous materials is difficult due to the absence of well defined peaks, as indicated in Figure 2.11.

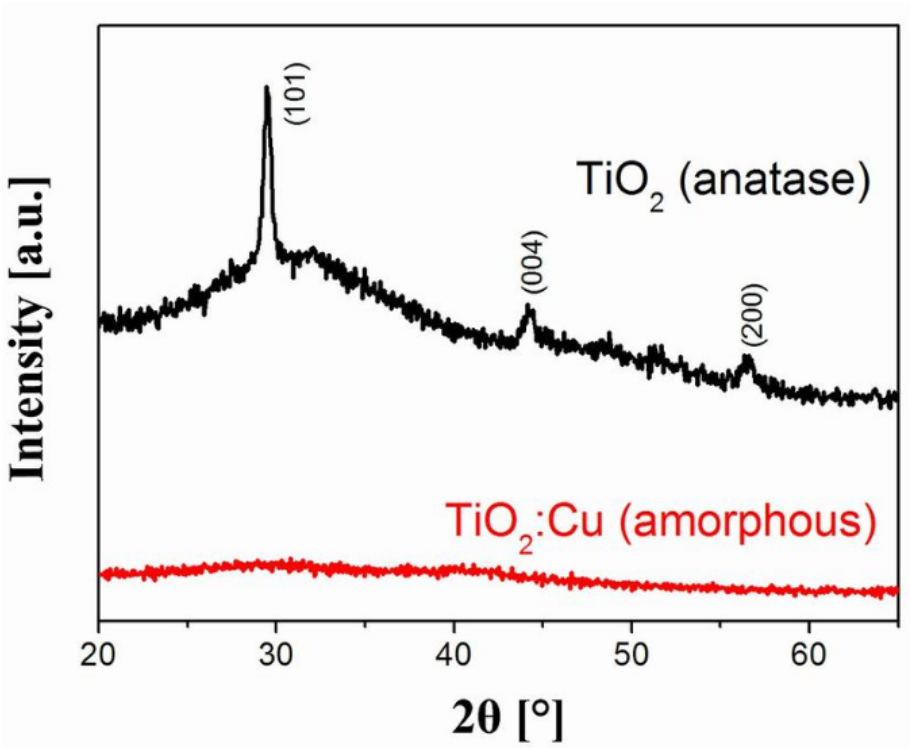

Figure 2.11: XRD diffractogram showing the XRD pattern of crystalline TiO_2 and amorphous TiO_2:Cu thin films. Obtained from [92].

2.4.3 Spectroscopic Ellipsometry

SE is a non-invasive and non-destructive optical technique that measures a change in polarization of light as incident radiation interacts with a thin film. These interactions lead to light polarization due to specific interactions between the thin films and the light waves [93]. When the incoming linearly polarized light interacts with the surface of the substrate, the light beam becomes transformed to elliptically polarized light. The elliptically polarized light is measured using a detector that converts the light beam to an electronic signal. The films interactions with linearly polarized light includes selective absorption, transmission, scattering, and reflection, enabling the characterization of the films thickness, d, which can range from a few angstrom to several microns. This technique also allows for the assessment of surface roughness, providing insight into the topographical variations of a film [93]. Additionally, it assesses the films index of refraction, n, providing insight into the extent to which light slows down when passing through a material compared to its speed in a vacuum. The working principle of the technique is presented in Figure 2.12.

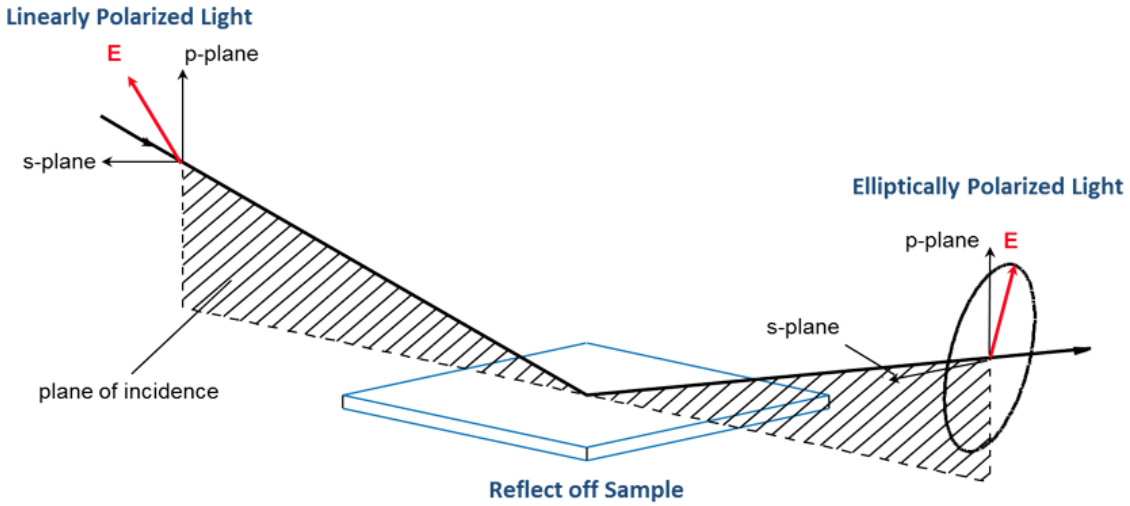

Figure 2.12: A sketch of the working principle of a spectroscopic ellipsometer highlighting the reflection of the incoming polarized light on contact with the sample to an elliptically polarized light. Obtained from [94].

The optical response of the sample when it interacts with light can be determined through a model analysis of the experimental measurements. The employed dispersion model is the Cauchy model, which describes the relationship between the wavelength, λ, and the index of refraction, n, as demonstrated in Equation 2.3. The Cauchy model is typically employed for the analysis of transparent thin films due its simplicity as it only requires a few fitting parameters.

$$n(\lambda) = n_0 + \frac{n_1}{\lambda^2} + \frac{n_2}{\lambda^4} \tag{2.3}$$

where the parameters n_0, n_1 and n_1, known as the Cauchy coefficients, are fitting coefficients that are adjusted during the fitting process to match experimental data with the models predictions. The instrument's simplicity, coupled with the fact that the technique is non-destructive, enables the analysis of the mentioned parameters over time, offering insights into the films evolution.

2.4.4 Fourier-Transform Infrared Spectroscopy

FTIR spectroscopy is an analytical technique that is used to determine the structure of molecules and the chemical composition of materials [95]. In FTIR, a sample is irradiated with varying frequencies of infrared radiation, causing unique modes of molecular vibrations, as depicted in Figure 2.13.

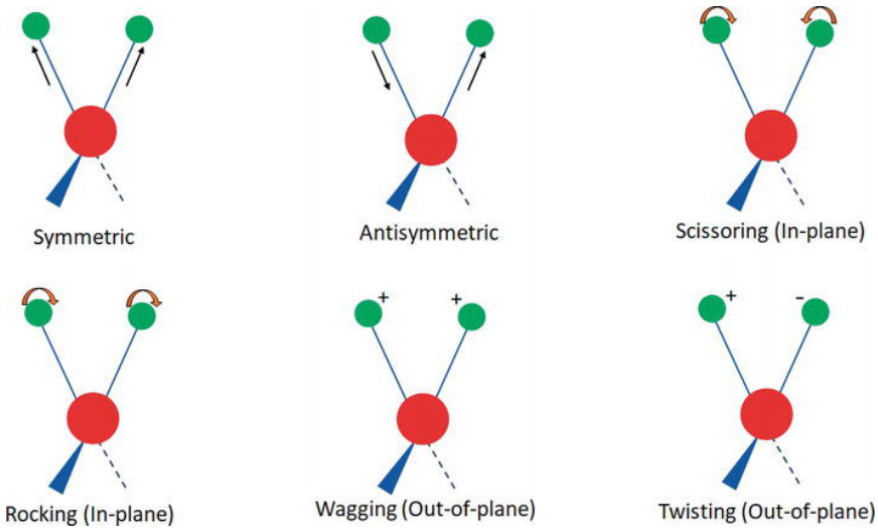

Figure 2.13: A schematic illustration of the modes of molecular vibration. Obtained from [96].

When the frequency of bond vibrations of a molecules is equivalent to the frequency of the infrared radiation, absorbance at that specific frequency occurs [95]. Thus, FTIR spectra can be viewed as distinctive fingerprints, enabling the identification of specific compounds within a molecule.

2.4.5 Ultraviolet-Visible Spectroscopy

UV-Vis spectroscopy is a technique that is used to characterize a materials absorbance of electromagnetic radiation from the ultraviolet (UV) to visible (Vis) region, encompassing wavelengths from 190 nm to 800 nm in the electromagnetic spectrum [97]. In this technique, a sample is subjected to UV and Vis light, enabling the measurement of light absorption, reflectance or transmission, which is measured as a function of wavelength. When a sample is irradiated, electrons within the atomic or molecular orbitals absorb energy and transition from lower to higher energy levels. The electronic transition that occurs corresponds to the absorption of energy at a particular wavelength. Information such as chemical composition, concentration, physical and electronic characteristics can be determined [97]. Equation 2.4 is used to obtain valuable information from thin films by

determining the relation between absorbance (A), transmittance (T), and reflectance (R).

$$T + R + A = 1 \tag{2.4}$$

Transmittance refers to the light that passes through the film, while reflectance refers to the light that is reflected by the film. Reflectance is inversely proportional to transmittance and is equivalent to 1-T [97]. Absorbance refers to the light that is absorbed by the film at a specific wavelength. A reference, which is used to obtain an absorbance spectrum that accurately represents the film, serves the role of establishing a standard or baseline for comparative analysis.

3 Experimental

This section of the report outlines the experimental methods that were utilized, commencing with ALD for film synthesis and subsequent characterization techniques.

3.1 Atomic Layer Deposition

3.1.1 Reactor

Thin films were synthesized using ALD reactor F-120 satellite from ASM microchemistry Ltd, presented in Figure 3.1 and 3.2. The reactor, which is based on the ASM Microchemistry F-120 reactor, was assembled at the Department of Chemistry at the University of Oslo. Nitrogen gas (<99.999% from PRAXAIR) was used as the carrier gas. An air-free environment in the reactor was achieved by using RV12 and iH600 pumps from Edwards. The digital signal output of the vacuum pressure gauges during depositions was 7.0 ± 1.0 mbar under Pirani APR 250 and circa -0.15 under Piezo TPR 261.

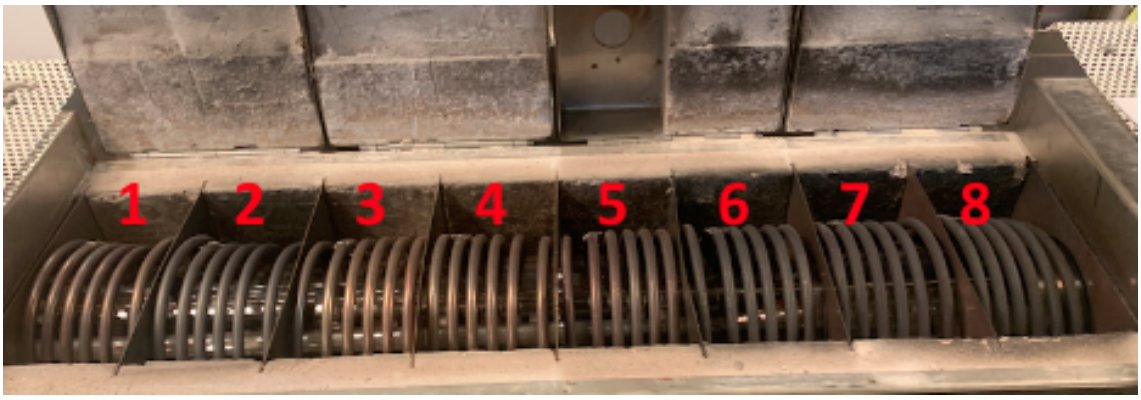

Figure 3.1: Image of the temperature zones 1-8 showing the heating coils and the metal sheet.

The temperature zones, which were separated by a metal sheet, were heated using heating coil. Temperature zones 1-4 were used to heat the precursors. The temperature in these zones varied according to the desired sublimation temperature. Zone 2 contained $ZrCl_4$ and zone 4 contained the organic linker molecules, 1,4-BDC and BP-4,4-DC. Zones 5-8 served to stabilise the temperature in the reaction chamber. Zones 7-8 contained the reaction chamber with the substrates, while zone 8 was also used as the control zone.

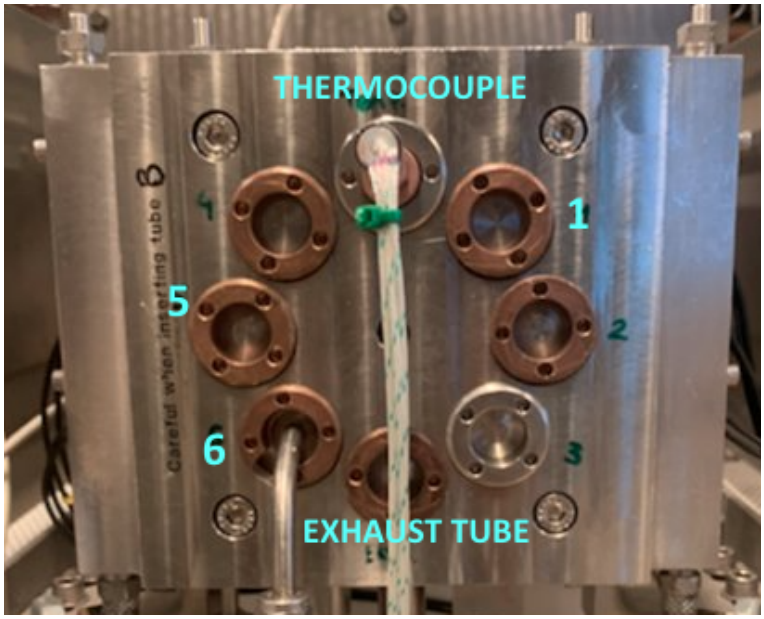

Figure 3.2: Image of the entry points for the precursors tubes, the thermocouple, and the exhaust tube.

During depositions, valve 1 was used for $ZrCl_4$, valve 5 was used for the organic linker molecules and valve 6 was used as the carrier valve for water and acetic acid. The valve at the bottom was used as an exhaust valve for carrying out byproducts and residue. The valve at the top contained the thermocouple. Two vacuum pumps were used to provide a vacuum. Pfeiffer Vacuum Duo 10 was used to evacuate the reactor to remove unwanted gases, reactants, or contaminants from the reactor system and Pfeiffer Vacuum Okta was used to further reduce the pressure.

3.1.2 Chemicals

Information regarding the chemicals that were used in this project are presented in Table 3.1.

Table 3.1: List of chemicals used in ALD deposition including chemical, chemical formula, CAS number, manufacturer, and purity.

Chemical	Chemical formula	CAS	Manufacturer	Purity
Nitrogen	N_2	500743	Linde plc	5.0 (<99.999% N_2)
Ionized water	H_2O	-	-	Type 2
Ozone	O_3	AC-2025 Ozone generator	IN USA Inc	15% O_3 in O_2
Oxygen	O_2	-	-	Air
Zirconium(IV) chloride	$ZrCl_4$	10026-11-6	Sigma-Aldrich	99.95+%-Zr
1,4-benzenedicarboxylic acid	$C_8H_6O_4$	100-21-0	Sigma-Aldrich	95%
Acetic acid	CH_3COOH	64-19-7	Sigma-Aldrich	99+%
Biphenyl-4,4 -dicarboxylic acid	$C_{14}H_{10}O4$	787-70-2	Sigma-Aldrich	97%

3.1.3 Substrates

Several substrates were used in the project. These substrates are listed in Table 3.2 and an illustration of the placement of silicon substrates inside the reaction chamber is presented in Figure 3.3. The silicon substrates were cleaned with dry wipes and blow dried to remove dust. The glass plates were washed with ethanol and blow dried. The electropolished steel substrates were covered with protective tape, thus no further course of action was taken as it was considered clean upon removing the tapes.

Table 3.2: Information regarding the specifications of different substrates.

Silicon					
Material	Diameter (mm)	Thickness (μm)	Dopant element	Lot number	Supplier
Silicon	200 ± 0.2	> 600	Boron	MG960	University Wafer
Glass					
Material	Diameter (mm)	Thickness (mm)	Lot number	Supplier	
Glass	50 x 75	1	6101	Benz Microscope Optics Center, Inc	
Electropolished Steel					
Material			Supplier		
Steel			Rimex Metals Group		

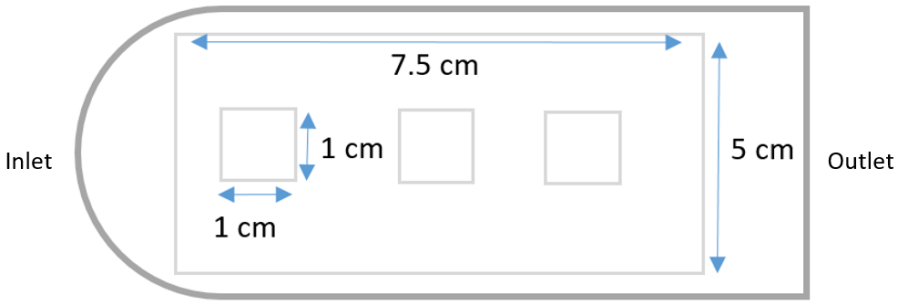

Figure 3.3: A schematic illustration of the reaction chamber from above. The silicon substrates were placed on a glass plate in the manner depicted. The position and size of the glass plate and silicon substrates are presented. A similar setup is used for the electropilshed steel.

3.1.4 Parameters

The standard precursor temperature for $ZrCl_4$ was set at 165 °C, while the standard precursor temperature for 1,4-BDC and BP-4,4-DC was set at 220 °C. The process parameters for the internal standard of known ZrO_2 growth is 4 s / 6 s / 5 s / 6 s for $ZrCl_4$ / purge / H_2O / purge. The growth rate for the internal standard was -0.2425 and -0.4324 for sensor A and sensor B, respectively. The process parameters for the internal standard of known Zr-1,4-BDC growth is 4 s / 6 s / 5 s / 6 s for $ZrCl_4$ / purge / 1,4-BDC / purge. The growth rate for the internal standard was -0.0003 and -0.0005 for sensor A and sensor B, respectively. The process parameters for the internal standard of known Zr-BP-4,4-DC growth is 4 s / 6 s / 15 s / 6 s for $ZrCl_4$ / purge / BP-4,4-DC / purge. The growth rate for the internal standard was -0.0011 and -0.0002 for sensor A and sensor B, respectively.

3.2 Characterisation

3.2.1 Quartz Crystal Microbalance

QCM analysis was performed in-situ using the ALD reactor. The setup, made by Ola Nilsen at the Department of Chemistry, is composed of a specifically designed QCR holder that is designed for the reaction chamber. It holds two 6 MHz gold-plated α-quartz crystals from Inficon (SPC-1157-G10) at a 5 cm distance from one another. The signal was obtained using an Inficon SQM-160 Rate/Thickness monitor and logged using a homemade Arduino-chipset. The data was analysed using a Python program prepared by Ola Nilsen. The reaction chamber and its components is presented in Figure 3.4.

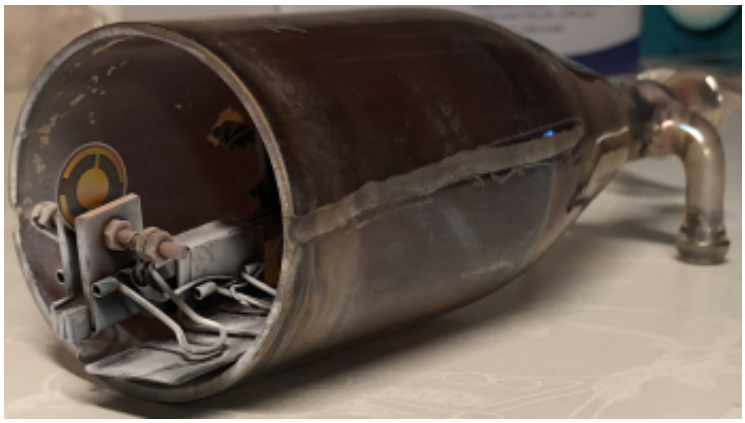

Figure 3.4: QCM setup showing the Quartz crystal holder setup located at the center of the reaction chamber, the QCR sensor nearest the exhaust.

3.2.2 X-Ray Diffraction

XRD measurements were taken using a Bruker AXS D8 diffractometer in Bragg-Brentano mode. The instrument is equipped with a LynxEye strip detector, a 90 position sample changer, and a Ge(111) Johanssen monochromator providing Cu Kα_1 radiation with a wavelength of 1.542 Å. We performed θ-2θ scans between 10° to 70° with a time resolution of 10 seconds per scan. The data was analyzed using DIFFRAC.EVA Version 6.0.0.7 from Bruker.

3.2.3 Precursor Tester

The Department of Chemistry has developed a specialized instrument to evaluate the thermal properties of precursors by simulating the conditions in an ALD reaction chamber. The instrument uses a thermocouple connected to a holder to heat substrates. The thermal properties of substrates can be examined in a vacuum environment by using a glass tube secured with a flexible hose clamp, as illustrated in Figure 3.5. A camera captured images at 30 second intervals. These images were run through a Python Script that analyzed the change in color in a specified area of the images, which was then plotted against temperature.

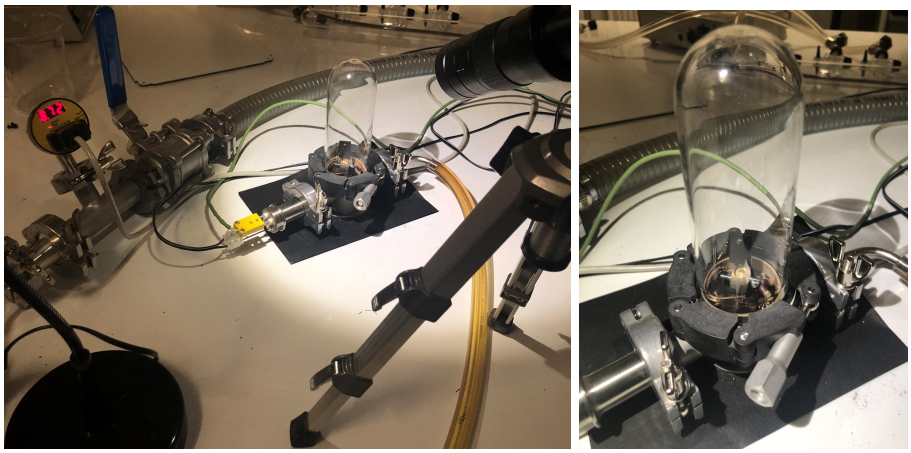

Figure 3.5: Images of the instrumental setup from above (left), showing the pressure gauge, thermocouple and camera, and up-close (right), showing the hose clamp and reaction chamber.

3.2.4 Spectroscopic Ellipsometer

The thickness, index of refraction, and roughness of the thin films were determined using a J.A. Woollam Co, Inc. ellipsometer of type α-SE^{TM} fit in the 380-900 nm range using a xenon light source. The measurements were made at a 70° angle of incidence and a refractive index of 632.8 nm. The ellipsometry data for the transparent films was fit to a Cauchy model. Silicon substrates and glass plates were used for ellipsometry. The silicon substrates had a thin native silicon oxide layer on the surface that was measured before each deposition. This layer was in the 1.5-2 nm range. Surface roughness was not included in the model as it did not improve the fit. The optical properties were modelled using CompleteEASE version 4.92. An image of the instrument is presented in Figure 3.6.

Figure 3.6: J.A. Woollam Ellipsometer Setup showing the light source, detector and sample stage.

In addition, the porosity of films were investigated by ellipsometric porosimetry using a J.A Wollam M-2000 Spectroscopic Ellipsometer with an environmental chamber. The ellipsometry data for the transparent films was fit to a Cauchy model. The optical properties were modelled using CompleteEASE version 6.52. An image of the environmental chamber is presented in Figure 3.7.

Figure 3.7: J.A. Woollam Ellipsometer setup showing the closed (left) and open (right) environmental chamber.

3.2.5 Fourier-Transform Infrared Spectroscopy

The deposited films were investigated using a Bruker Vertex 70 FTIR spectrometer in reflection mode. Electropolished steel substrates were used to acquire the FTIR spectra and an uncoated electropolished steel substrate was used as background. The data was acquired using OPUS version 7.0 from Burker.

3.2.6 UV-Vis Spectroscopy

UV-Vis spectroscopy measurements were conducted using a Shimadzu UV-3600 Photospectrometer with a spectral range from 200 to 1700 nm. A D2 lamp was used for the UV region of the spectrum and a halogen lamp was used for the visible and near-infrared (NIR) wavelengths. Data was acquired using a photomultiplier tube for 180 – 900 nm. Data acquisition was carried out with a Shimadzu UVProbe software, version 2.43.

3.2.7 Visual Tools

The graphs and figures presented in the report have been produced in Origin Graphing Analysis version 2022b from OriginLab and Microsoft PowerPoint 2016. The chemical structures have been produced in ChemDraw v21.0 from PerkinElmer, Inc, as well as Web whiteboard from Miro. The report and tables have been produced in TeX Live 2022 from Overleaf.

4 Results

This section present an overview of the experimental findings during our investigation.

4.1 Growth

4.1.1 ZrO_2 system

The first objective was to verify growth of ZrO_2, to determine the stability of the process over time, and to characterise the stability of the Atomic Layer Deposition (ALD) reactor. The results presented in Figure 4.1 show a reproducibility test to determine variations in film thickness and index of refraction between depositions of ZrO_2. The error bars correspond to the standard deviation of the three substrates. The parameters for the ZrO_2 system was 3 s / 6 s / 5 s / 6 s for $ZrCl_4$ / purge / H_2O / purge. The depositions were carried out at 220 °C.

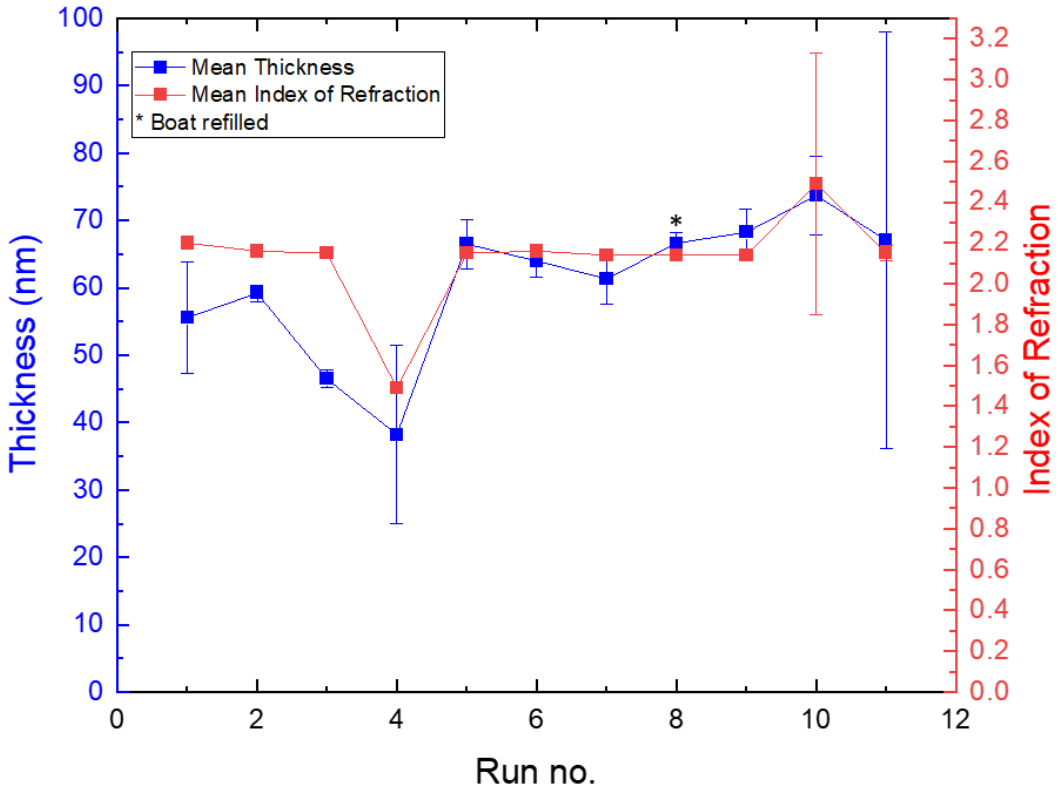

Figure 4.1: Thickness, index of refraction, and standard deviation of ZrO_2 films acquired over 405 cycles for a total of 11 runs. The blue squares correspond to the average thickness of the films and the red squares correspond to the average index of refraction of the films.

Figure 4.1 shows a steady decrease in film thickness between run no. 2-4 and 5-7. This can be attributed to a reduction in the precursor quantity and sintering, the latter factor contributing to a decrease in the surface area of the precursor, and hence evaporation rate. To counteract this, the boats were replenished with their respective precursors after run no. 7. A relatively constant thickness in the refractive index is observed between run no. 1-9, with run no. 4 being an exception. This exception could be due to instrumental error. The large variation in the index of refraction and film thickness for run no. 10 and 11, respectively, is possibly due to temperature fluctuations in the reactor.

4.1.1.1 Analysis of growth dynamics by QCM

The growth of ZrO_2 using $ZrCl_4$ and H_2O was investigated by Quartz Crystal Microbalance (QCM) as a reference for further investigations of the hybrid materials to follow. The aim was to characterize the stoichiometry and gain a better understanding of the effect of water on $ZrCl_4$. The change in mass during the pulse and purge of $ZrCl_4$ and H_2O is presented in Figure 4.2. The deposition was carried out at a reaction temperature of 245 °C.

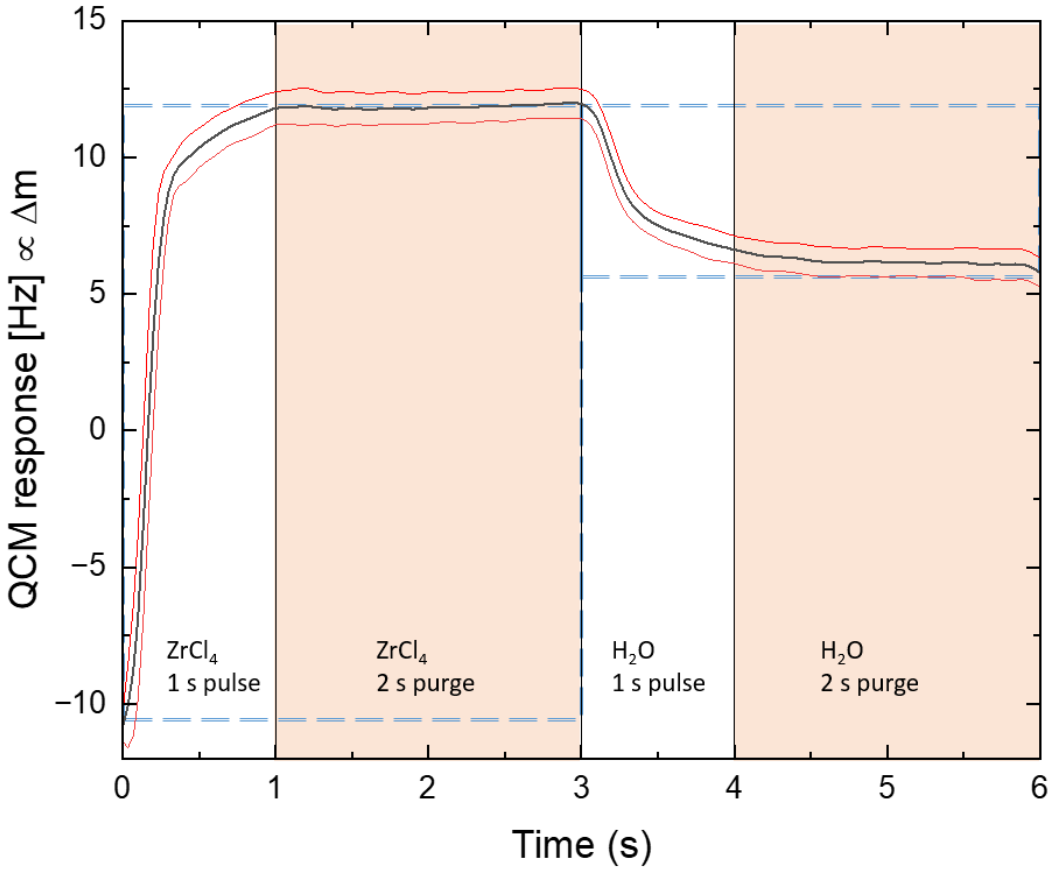

Figure 4.2: QCM cycle showing the change in mass as a function of time for the ZrO_2 system. The figure contains two dashed rectangles to indicate Δm_1 ($ZrCl_4$ pulse and purge), left, and Δm_2 (H_2O pulse and purge), right. The red lines indicate the standard deviation of the measurements.

Figure 4.2 shows a mass increase during the $ZrCl_4$ pulse. The shape of the growth indicates rapid saturation since only a small variation in growth is observed after approximately 0.25 seconds. The stable and consistent mass during purging indicates that desorption of the precursor was minimal. This indicates that the precursor is strongly bound to the surface of the substrate forming a stable

and adherent layer. The mass decrease during the water pulse is attributed to the substitution of heavier chlorine atoms with lighter hydroxide ions. Further mass decrease is also observed during the water purge, indicating removal of water that has entered the pores of the film.

In order to assess the necessary $ZrCl_4$ pulse time to achieve saturation and to eventually determine the effect of pulse time on the stoichiometry, the mass at varied pulse times was examined for both sensor A and sensor B, see Figure 4.3. The plot has been normalized with respect to an internal standard of known ZrO_2 growth. The parameters for the Zr-1,4-BDC system was 0-12 s / 6 s / 5 s / 6 s for $ZrCl_4$ / purge / 1,4-BDC / purge. The deposition was carried out at a reaction temperature of 245 °C.

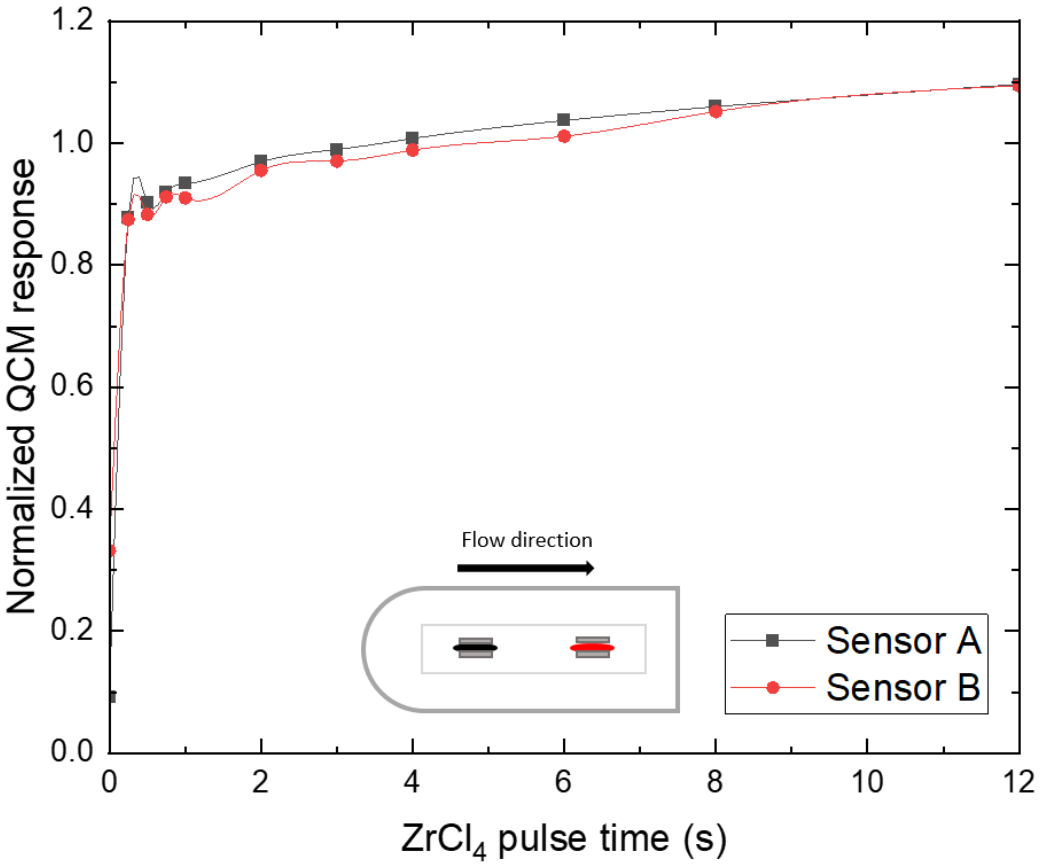

Figure 4.3: The growth rate as a function of pulse time as measured by QCM for $ZrCl_4$. $ZrCl_4$ is normalized with respect to an internal standard of known ZrO_2 growth.

It is clear from Figure 4.3 that the majority of reactions at the surface of the substrate have taken place after approximately 0.25 seconds of pulsing $ZrCl_4$. This indicates that the 1 second pulse of $ZrCl_4$, Figure 4.2, should have been sufficient to achieve saturation. A slow increase in mass is observed over longer exposure which may be due to CVD growth and/or rearrangement of weakly adsorbed precursor fragments on the surface of the film. The difference in the mass between sensor A and sensor B could be attributed to the gradient in the chamber. Larger growth is observed for sensor A. This was expected since it was located at the inlet. However, the time at which saturation is reached is almost equal for both sensors. As the growth for one of the sensors varies, so does the other by a similar amount.

To further investigate the reason for the increase in mass and to verify that saturation was achieved within 1 second, an additional QCM cycle of the ZrO_2 system with longer pulse and purge times was performed. The primary objective was to determine whether a prolonged $ZrCl_4$ pulse time better represents the stoichiometry of a ZrO_2 system. The results with modified parameters are presented in Figure 4.4. The deposition was carried out at a reaction temperature of 245 °C.

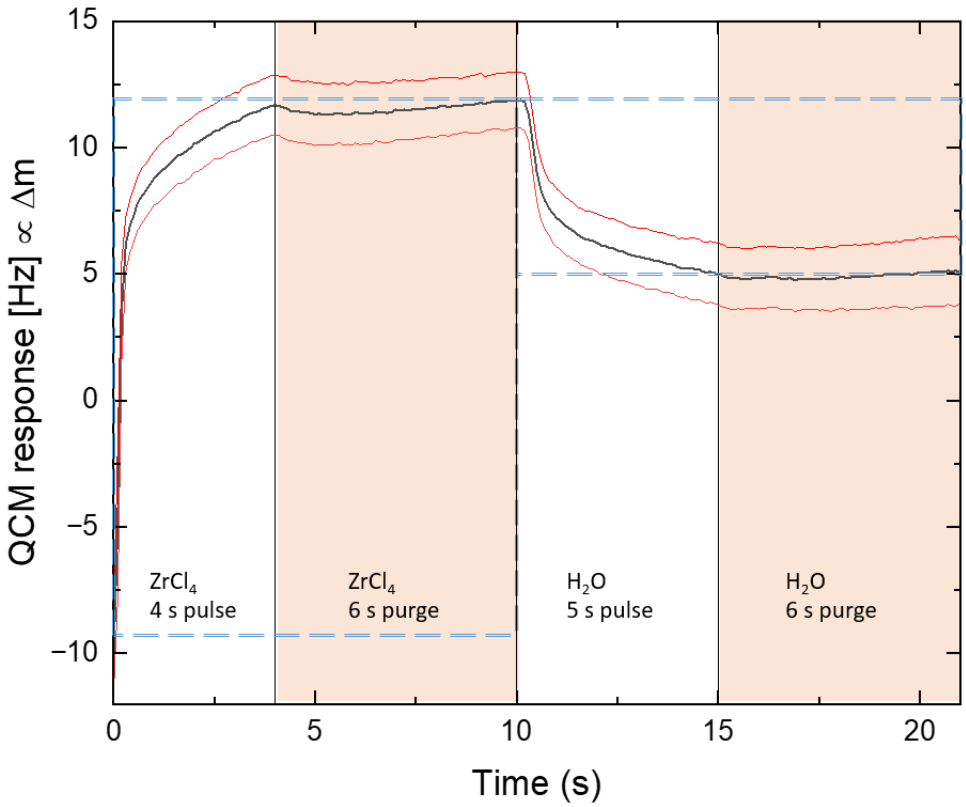

Figure 4.4: QCM cycle showing the change in mass as a function of time for the ZrO_2 system. The figure contains two dashed rectangles to indicate Δm_1 ($ZrCl_4$ pulse and purge), left, and Δm_2 (H_2O pulse and purge), right. The red lines indicate the standard deviation of measurements.

In comparison to Figure 4.2, the growth rate of the $ZrCl_4$ pulse remains consistent; however, the magnitude of mass increase varies. Some loss in mass is observed during the subsequent purging step. This could be attributed to desorption of physisorbed molecules, indicating that both chemisorption and physisorption occurred during pulsing. The decrease in mass when water is pulsed and purged is similar to Figure 4.2. The main difference is the larger standard deviation in Figure 4.4.

4.1.2 Zr-1,4-BDC system

The first objective for the synthesis of Zr-1,4-BDC was to achieve reproducible growth. This was investigated by performing comparative analysis by varying the number of cycles as well as the pulse and purge times. The depositions were carried out at a reaction temperature of 245 °C. The parameters were selected from previous depositions carried out by the NAnostructure and FUnctional MAterials (NAFUMA) research group [17]. The parameters for the Zr-1,4-BDC system was 4 s / 6 s / 5 s / 6 s for $ZrCl_4$ / purge / 1,4-BDC / purge for the 100 cycle depositions and 3 s / 4 s / 3 s / 4 s for $ZrCl_4$ / purge / 1,4-BDC / purge for the 500 cycle depositions. These parameters were used to produce the results presented in Table 4.1.

Table 4.1: Run no. and (cycles), mean thickness (nm), growth per cycle (GPC) (nm/cycle), and index of refraction for the Zr-1,4-BDC system.

Run no. (cycles)	Thickness (nm)	GPC (nm/cycle)	Index of refraction
15(100)	80	0.8	1.69
16(500)	360	0.7	1.72
17(100)	81	0.8	1.88
18(500)	326	0.7	1.69
19(100)	93	0.9	1.64
20(500)	337	0.7	1.69

Despite the limited number of runs, the results show that the incorporation of 1,4-BDC resulted in relatively consistent film growth for the 100 and 500 cycle depositions.

4.1.2.1 Analysis of growth dynamics by QCM

The growth of Zr-1,4-BDC using $ZrCl_4$ and 1,4-BDC precursors was investigated by QCM. The aim was to characterize the growth by investigating the relative mass increase during pulsing and purging of the precursors. The QCM response is presented in Figure 4.5. The deposition was carried out at a reaction temperature of 245 °C.

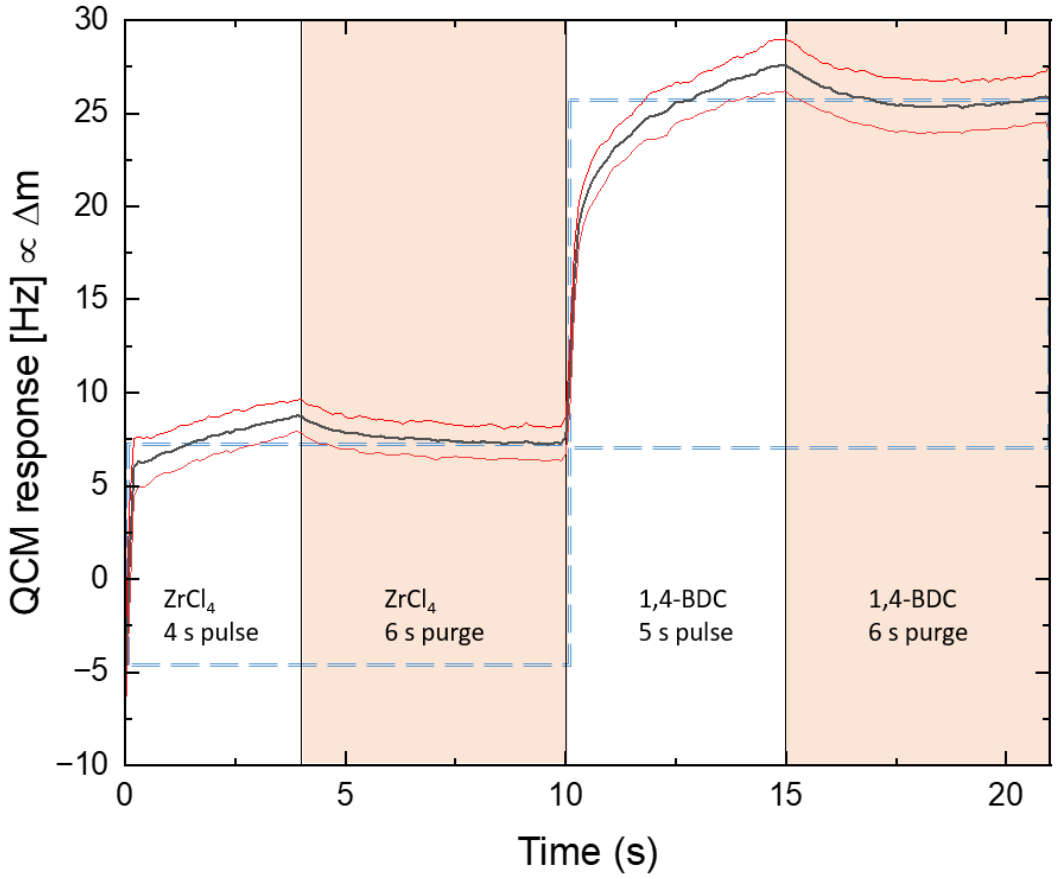

Figure 4.5: QCM cycle showing the change in mass as a function of time for the Zr-1,4-BDC system. The figure contains two dashed rectangles to indicate Δm_1 ($ZrCl_4$ pulse and purge), left, and Δm_2 (1,4-BDC pulse and purge), right. The red lines indicate the standard deviation of measurements.

By depositing $ZrCl_4$ on a 1,4-BDC surface, we notice a slow and steady increase in the mass of $ZrCl_4$ between approximately 0.25-4 seconds. This indicates that a short pulse time is required to achieve saturation. The steady increase in mass may correspond to incomplete surface reactions. During

the purging step of the process, the decrease in mass may correspond to removal of physisorbed molecules. It is also possible that the decrease in mass is due to the rearrangement of precursor fragments. This could potentially result in the loss of certain functional groups or atoms. The almost constant mass between 7-10 seconds indicates that no further desorption or rearrangement of precursor fragments occur. A similar response is observed for the deposition of the organic linker, (1,4-BDC).

In order to assess the necessary 1,4-BDC pulse time to achieve saturation and to eventually determine the effect of pulse time on the growth of the system, the mass at varied pulse times was examined for both sensor A and sensor B, Figure 4.6. The plot has been normalized with respect to an internal standard of known Zr-1,4-BDC growth. The deposition was carried out at a reaction temperature of 245 °C over 20 cycles. The parameters for the Zr-1,4-BDC system was 4 s / 6 s / 0-20 s / 6 s for $ZrCl_4$ / purge / 1,4-BDC / purge.

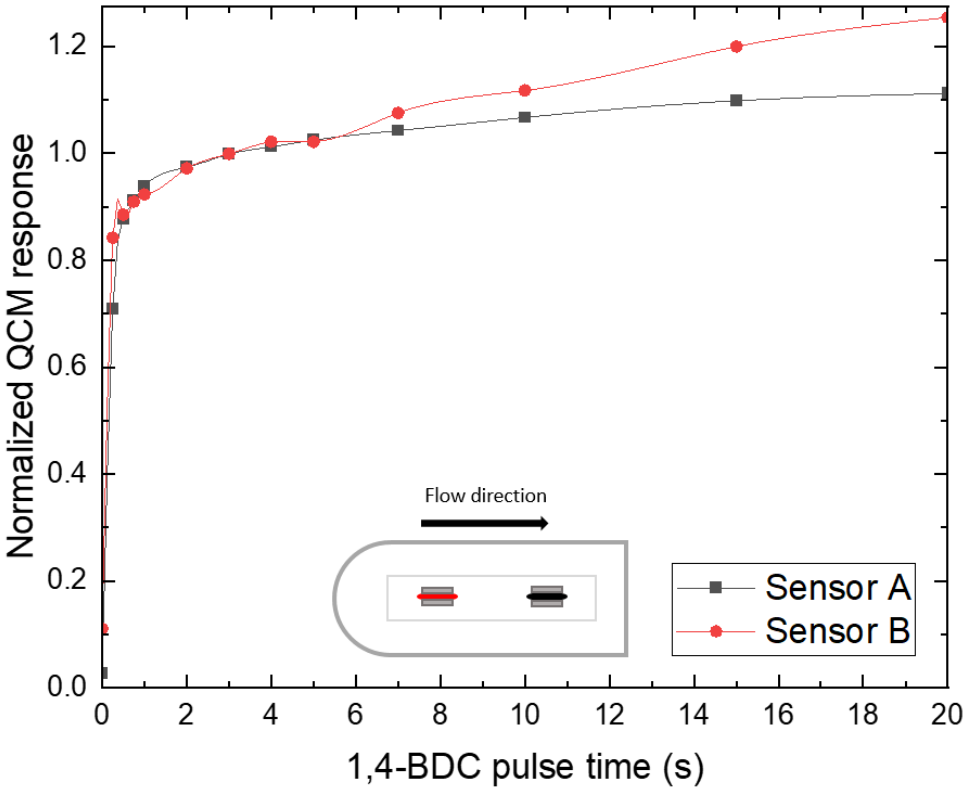

Figure 4.6: The growth rate as a function of pulse time as measured by QCM for 1,4-BDC. 1,4-BDC is normalized with respect to an internal standard of known Zr-1,4-BDC growth.

Figure 4.6 clearly demonstrates that a 4 second pulse of 1,4-BDC is sufficient to achieve saturation. This suggests that the QCM data presented in Figure 4.5 depicts a system where both precursors

have reached saturation. Thus, that system should reflect the stoichiometry of Zr-1,4-BDC. Similarly to Figure 4.3, approximately 0.25 seconds of a 1,4-BDC pulse was sufficient for the majority of reactions at the surface of the substrate to occur. The gradual increase in mass during extended exposures could stem from either CVD growth or the rearrangement of precursor fragments on the surface opening for more reactive sites. Deviation in mass between the two crystals is observed after approximately 5.5 seconds, where higher growth is observed for sensor B. This is expected since the sensor is located at the inlet.

4.1.2.2 QCM of Zr-1,4-BDC with water pulsing

An *in-situ* QCM investigation of a Zr-1,4-BDC system containing a pulse and purge sequence of water was performed. The purpose of this investigation was to evaluate how varying the precursor sequence affects the systems growth. The deposition was carried out at a reaction temperature of 230 °C. The results are presented in Figure 4.7.

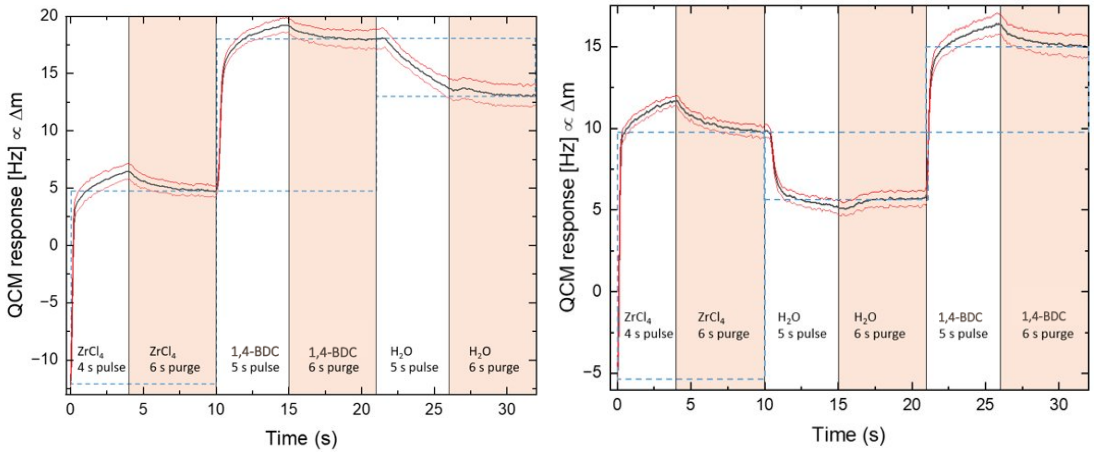

(a) The figure contains three dashed rectangles to indicate Δm_1 ($ZrCl_4$ pulse and purge), left, Δm_2 (1,4-BDC pulse and purge), center, and Δm_3 (H_2O pulse and purge), right.

(b) The figure contains three dashed rectangles to indicate Δm_1 (ZrCl4 pulse and purge), left, Δm_2 (H_2O pulse and purge), center, and Δm_3 (1,4-BDC pulse and purge), right.

Figure 4.7: QCM cycle showing the change in mass as a function of time for the (a) $ZrCl_4$+1,4-BDC+H_2O and (b) $ZrCl_4$+H_2O+1,4-BDC systems. The depositions were carried out at 245 °C. The red lines indicate the standard deviation of measurements.

Figure 4.7.a presents a QCM cycle where Zr-1,4-BDC+H_2O are deposited. Following the deposition of $ZrCl_4$ and 1,4-BDC, a noticeable reduction in mass is observed upon pulsing and purging water. Figure 4.7.b also shows a decrease in mass upon pulsing and purging water. The more significant decrease in mass when water is pulsed after the $ZrCl_4$ cycle, Figure 4.7.b, compared to the pulsing of water after the 1,4-BDC cycle, Figure 4.7.a, could indicate that water has a higher chemisorption efficiency to a $ZrCl_4$ surface compared to a 1,4-BDC surface. The decrease in mass when water is pulsed in Figure 4.7.a indicates etching of 1,4-BDC. Figure 4.7.a has the higher growth at $\Delta m = 25$, compared to $\Delta m = 20.5$ for Figure 4.7.b.

4.1.3 Zr-BP-4,4-DC system

4.1.3.1 Analysis of growth dynamics by QCM

To evaluate the reactivity and stability of the Zr-BP-4,4-DC system, various parameters were examined. The first parameter assessed was the pulse time required to saturate BP-4,4-DC. This is presented in Figure 4.8. The plot has been normalized with respect to an internal standard of known Zr-BP-4,4-DC growth. The parameters for the Zr-BP-4,4-DC system was 4 s / 6 s / 0-80 s / 6 s for $ZrCl_4$ / purge / BP-4,4-DC / purge. The deposition was carried out at a reaction temperature of 265 °C.

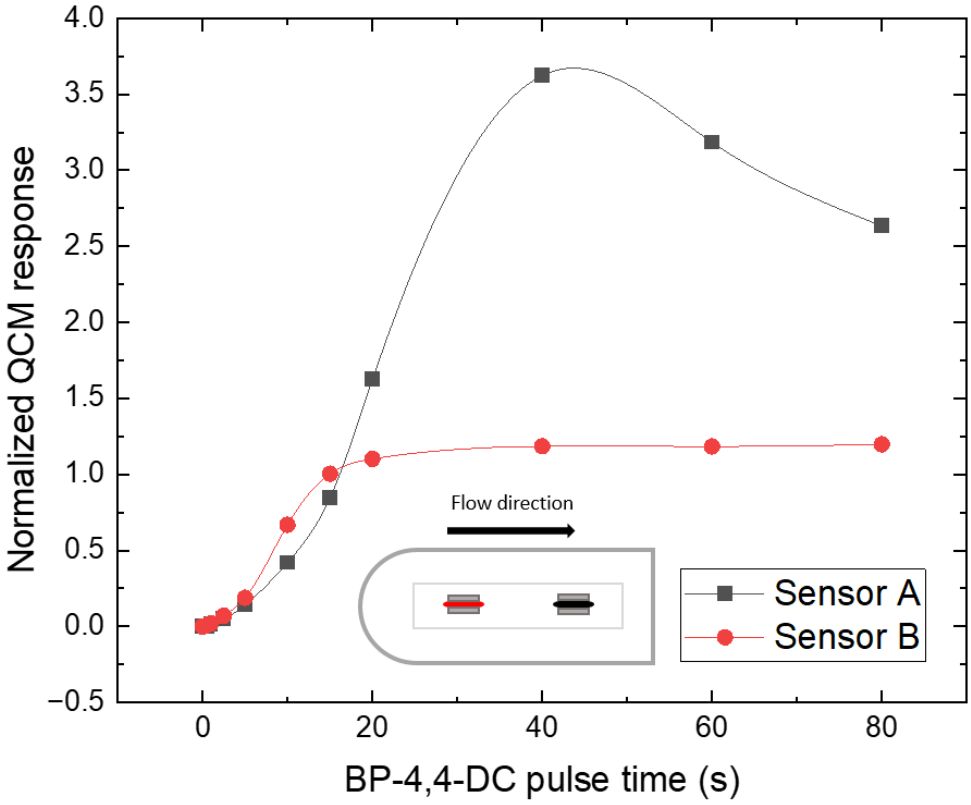

Figure 4.8: The growth rate as a function of pulse time as measured by QCM for the BP-4,4-DC system. BP-4,4-DC is normalized with respect to an internal standard of known Zr-BP-4,4-DC growth.

The curve for sensor B indicates that a pulse of approximately 40 seconds of BP-4,4-DC is required to achieve self-limiting growth. The growth rate is slow between 0-5 seconds, followed by a substantial increase between 5-10 seconds. The growth rate eventually stabilizes after 10 seconds

indicating the self-limiting growth that is typical of ALD processes. The growth rate displays a sigmoidal curve, indicating a deviation from ideal behaviour. The growth rate of sensor A indicates a potential sensor malfunction. While both sensors displayed unexpected growth rates, further analysis of the Zr-BP-4,4-DC system was conducted by focusing on sensor B. To support this, a direct comparison of the two sensors was carried out, as illustrated in Figure 4.9. The depositions were carried out at a reaction temperature of 265 °C.

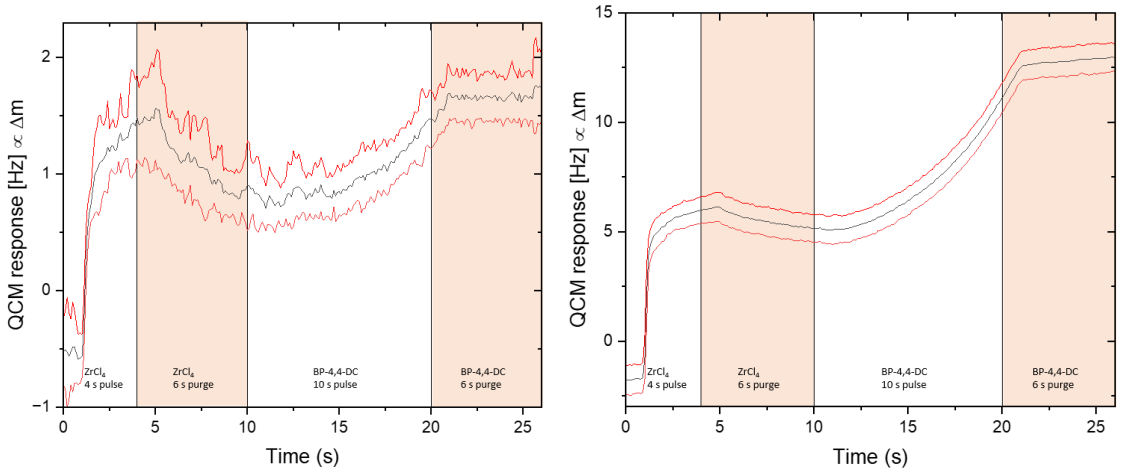

(a) QCM cycle from sensor A.

(b) QCM cycle from sensor B.

Figure 4.9: QCM cycle showing the change in mass as a function of time for the Zr-BP-4,4-DC system. The red lines indicate the standard deviation of measurements.

An irregular growth pattern is observed in sensor A, Figure 4.9.a, indicating non-uniform growth. The $ZrCl_4$ pulse in Figure 4.9.b shows an increase in mass as $ZrCl_4$ adsorbs to the crystal. The subsequent purging shows a steady decrease in mass, which might indicate CVD growth and/or rearrangement of weakly adsorbed precursor fragments on the surface of the film. Although purging initiated at 4 seconds, growth is observed between 4-5 seconds. This increase in mass, as well as the increase that is observed between 20-21 seconds could be due to a delay in the instrument. A 10 second pulse of BP-4,4-DC led to a slow increase in mass. A more rapid increase in mass should have occurred, since BP-4,4-DC is heavier than 1,4-BDC. The slow growth rate of BP-4,4-DC may be due to increased steric hindrance caused by the bulkier molecules blocking reaction sites. It is evident that complete saturation of BP-4,4-DC did not occur. Nonetheless, the data from sensor B is superior to that of sensor A by providing results that better align with what is expected.

The stoichiometry for the Zr-BP-4,4-DC system can be investigated by inspecting the QCM response for Δm_1 and Δm_2 in Figure 4.10. BP-4,4-DC was pulsed for 40 seconds. The choice of pulse time was based on the observed change in mass of sensor B in Figure 4.8. The depositions was carried out at a reaction temperature of 265 °C.

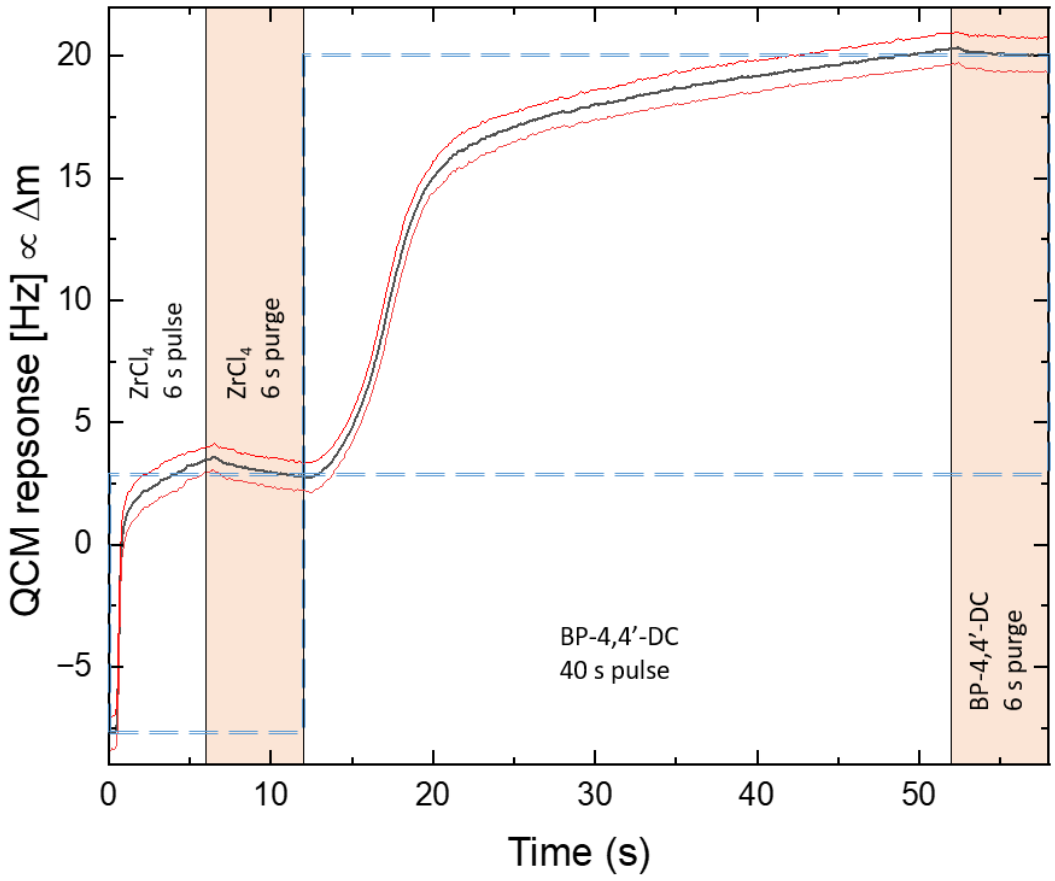

Figure 4.10: QCM cycle showing the change in mass as a function of time for Zr-BP-4,4-DC. The figure contains dashed rectangles to indicate Δm_1 ($ZrCl_4$ pulse and purge), left, and Δm_2 (BP-4,4-DC pulse and purge), right. The red lines indicate the standard deviation of measurements.

Increasing the pulse time from 10-40 seconds led to saturation of BP-4,4-DC. A steady mass increase occurs between 20-60 seconds. The minimal reduction in mass during the subsequent purge step reinforces the assumption that steric hindrance is responsible for the slow growth rate of BP-4,4-DC.

After having performed the previous depositions, we realised that we were unable to obtain the expected growth for ZrO_2 as illustrated in Figure 4.4, most probably due to the porosity created on the surface. We attempted but failed to obtain reproducible growth of ZrO_2 in 20 cycles with the following parameters; 12 s / 20 s / 20 s / 30 s for $ZrCl_4$ / purge / H_2O / purge. Therefore, we decided to examine whether we could achieve standard stable growth of Zr-BP-4,4-DC after the 20 cycles of ZrO_2. This would enable us to investigate the effect that ZrO_2 from prior depositions has on Zr-BP-4,4-DC. The results are presented in Figure 4.11. The deposition was carried out at 245 °C with the following parameters; 4 s / 6 s / 15 s / 6 s for $ZrCl_4$ / purge / BP-4,4-DC / purge.

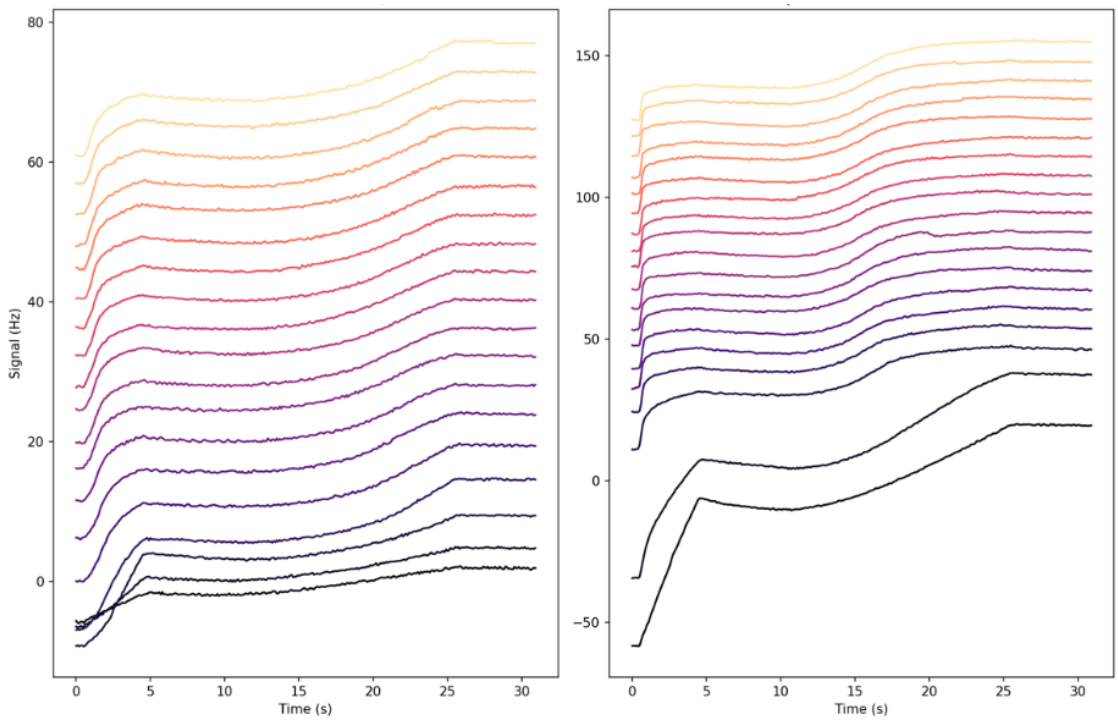

Figure 4.11: QCM response for the consecutive depositions of Zr-BP-4,4-DC. The cycle at the bottom of the graph (black) represents the first cycle, whilst the cycle at the top of the graph (yellow) represents the last cycle. The growth of the cycles at 0 seconds is positioned above the preceding cycle by a distance equal to 75% the growth of the preceding cycle. The left graph corresponds to sensor A and the right graph corresponds to sensor B.

The results indicates that standard stable growth is achieved after 4 cycles in sensor A and 3 or 4 cycles in sensor B. The first 2 cycles of sensor B show that saturation of $ZrCl_4$ was not achieved prior to purging. It is also evident that a slow increase in mass during the pulse of BP-4,4-DC occurs in all the cycles. Moreover, the growth of the cycles assume a similar curve as the deposition progresses. This implies standard stable growth.

An attempt was made to cap the Zr-BP-4,4-DC film with ZrO_2 to assess its stability. This would provide an insight into the chemical activity of the film. To establish a sufficient capping layer, 200 consecutive cycles of ZrO_2 were deposited on a Zr-BP-4,4-DC film. The parameters for the ZrO_2 system were 2 s / 2 s / 1 s / 2 s for $ZrCl_4$ / purge / H_2O / purge. The results, Appendix 8.5, show that standard stable growth was not achieved within 200 cycles. This indicates that the bulk of the material is chemically active during the growth of ZrO_2 even after 200 cycles.

4.1.3.2 QCM of Zr-BP-4,4-DC with water pulsing

A QCM investigation of a Zr-BP-4,4-DC system containing a pulse and purge sequence of water was performed. This was done to evaluate how varying the precursor sequence affects the systems growth. The deposition was carried out at a reaction temperature of 245 °C. The results are presented in Figure 4.12.

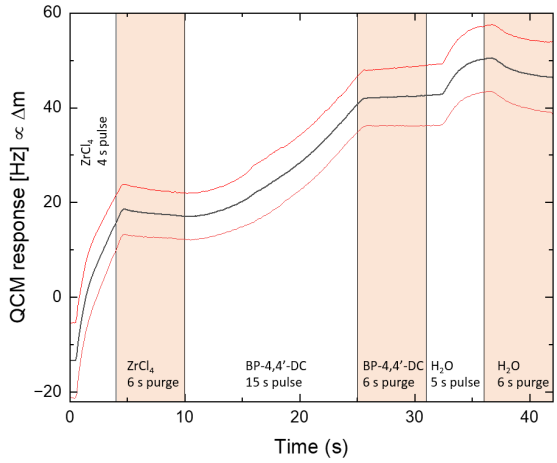

(a) QCM cycle of a Zr-BP-4,4-DC+H_2O system.

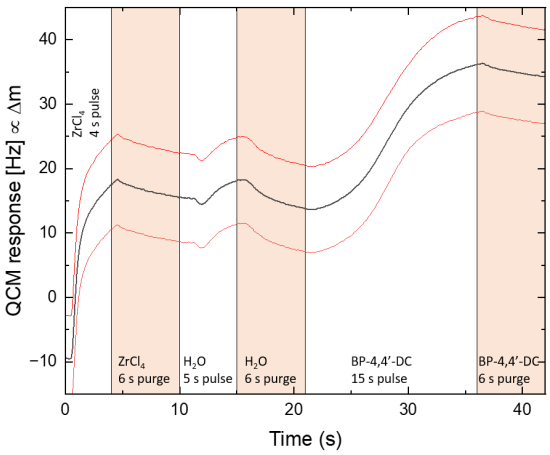

(b) QCM cycle of a $ZrCl_4$+H_2O+BP-4,4-DC system.

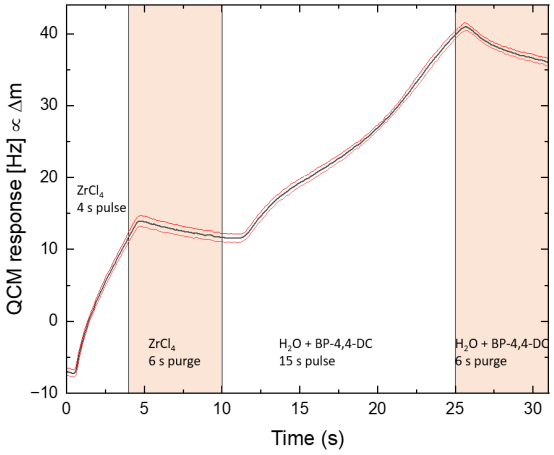

(c) QCM cycle of a $ZrCl_4$+H_2O+BP-4,4-DC system.

Figure 4.12: QCM cycle showing the change in mass as a function of time for the Zr-BP-4,4-DC system with water pulsing. The red lines indicate the standard deviation of measurements.

The results suggest that while Figure 4.12.a and b exhibit large standard deviations, their growth represent ALD-type growth more accurately than Figure 4.12.c. All the figures indicate a delay in the system, which could be due to instrumental malfunction. Saturation of BP-4,4-DC is only observed for Figure 4.12.b. The observed sigmoidal growth during pulsing indicates that the linker molecule encounters difficulties in adsorbing onto the OH-terminated surface. The decrease in mass during BP-4,4-DC purging, Figures 4.12.b and c, indicates a lack of growth stabilization during pulsing. The observed increase in mass after pulsing water, Figures 4.12.a and b, indicates water getting into the pores. The subsequent decrease in mass during purging suggests removal of water

that entered the pores. However, some water remains in the pores of the film in Figure 4.12.a, as indicated by the increase in mass upon the completion of the water cycle. Figure 4.12.c shows that co-pulsing water and BP-4,4-DC did not yield conclusive results.

4.1.3.3 Porosity characterization by QCM

The aim in this section was to gain an insight into the porosity of a Zr-BP-4,4-DC system. This is crucial for interpreting the film's evolution during treatment on the ellipsometer with the heating plate. Figure 4.13.a illustrates the deposition of ZrO_2 on a pristine crystal, whereas Figure 4.13.b illustrates the deposition of ZrO_2 on a crystal containing hybrid film from prior depositions. The reaction temperature for the depositions was 245 °C. It is important to note that the parameters for both cycles are identical.

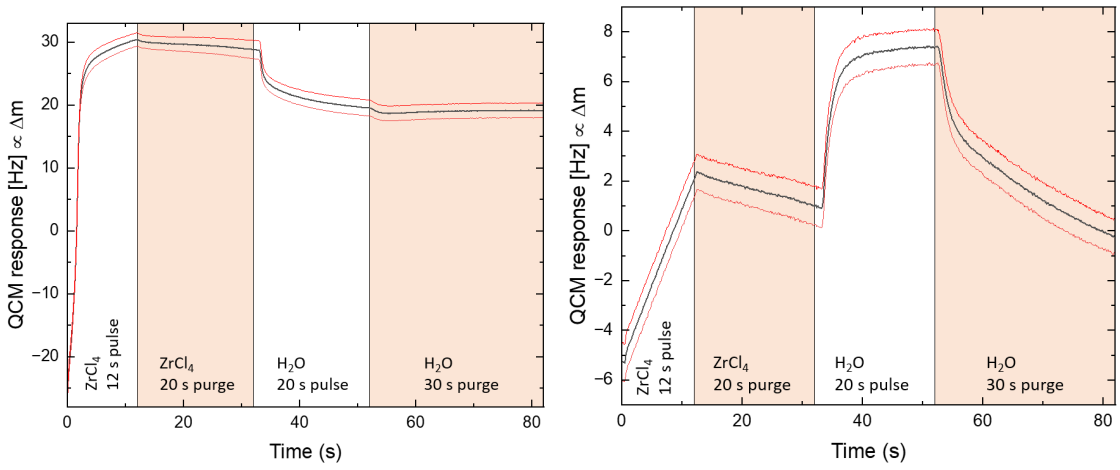

(a) QCM cycle of ZrO_2 deposition on a pristine crystal.

(b) QCM cycle of ZrO_2 2 on a crystal containing hybrid film from previous depositions.

Figure 4.13: QCM cycle showing the change in mass as a function of time for the ZrO_2 system. The The red lines indicate the standard deviation of measurements

Figure 4.13.a shows a decrease in mass during the water pulse, which is expected due to the lower molar mass of hydroxide atoms compared to the chloride atoms. Figure 4.13.b shows an increase in mass during the water pulse, which indicates water getting into the pores. The observed decrease in mass during the water purge suggests that water that gets into pores is eventually removed. Additionally, the mass upon the completion of water purging, Figure 4.13.b, is less than the mass at the beginning of the cycle. This suggests that chlorine atoms have also been removed.

4.1.3.4 QCM of Zr-BP-4,4-DC with acetic acid pulsing

QCM investigation of acetic acid as a modulator to achieve compositional control during growth was performed. The sublimation temperature for BP-4,4-DC was 250 °C, while the reaction temperature was 265 °C. The results are presented in Figure 4.14.

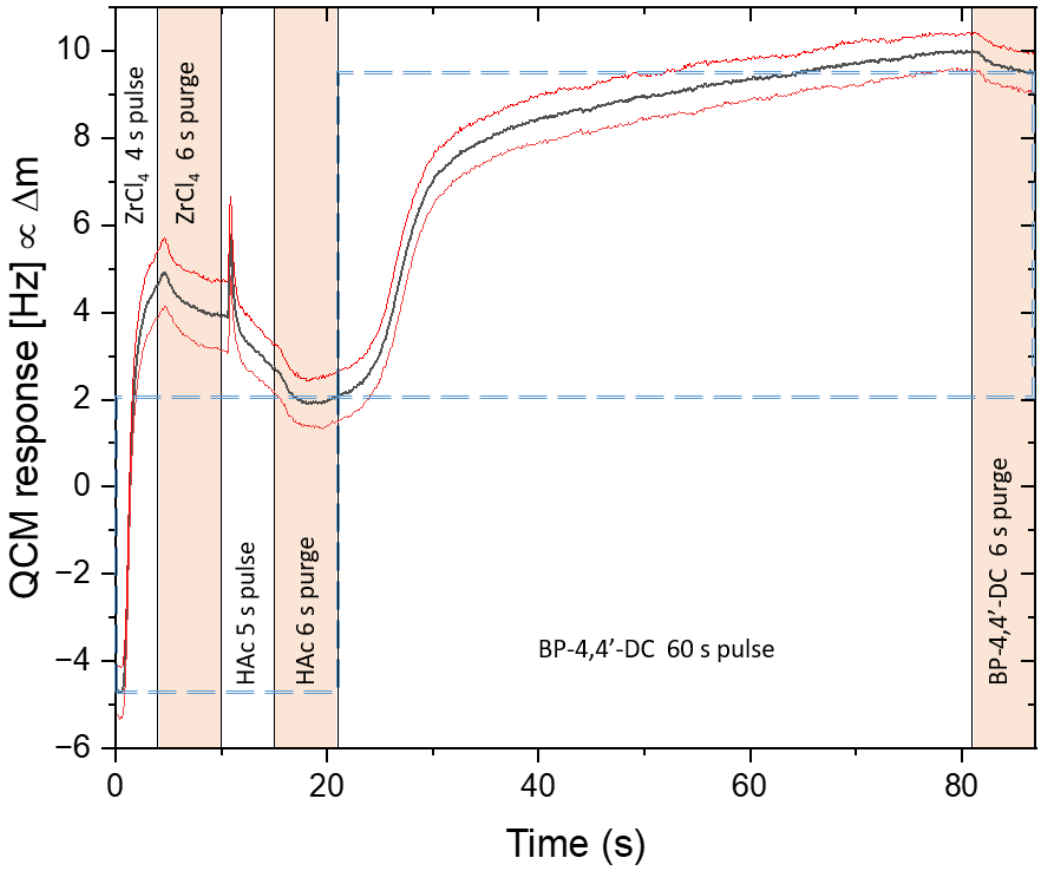

Figure 4.14: QCM cycle showing the change in mass as a function of time for the Zr-BP-4,4-DC with acetic acid pulsing. The red lines indicate the standard deviation of measurements.

Pulsing acetic acid resulted in a rapid increase, followed by a rapid decrease, and finally a steady decrease in mass. The rapid increase and decrease could indicate acetic acid coordinating to and dissociating from zirconium. The steady decrease in mass during pulsing indicates surface etching where acetic acid etches the surface of the film. This decrease in mass continues even after pulsing has concluded. The change in mass of BP-4,4-DC is as expected, although a small decrease in mass is observed during purging. This decrease could correspond to rearrangement of weakly adsorbed precursor fragments on the surface of the film.

4.2 Characterization

This section provides results from the characterization techniques that were employed.

4.2.1 XRD

The crystallinity of Zr-1,4-BDC films underwent characterization using X-Ray Diffraction (XRD). One Zr-1,4-BDC film was stored in a humidity chamber, while the other films were subjected to heat treatment using a Spectroscopic Ellipsometer (SE) with an environmental chamber filled with nitrogen gas and/or water vapor. The results, presented in Figure 4.15, indicate that all the films exhibit amorphous character. A peak is observed at 27.9 °for Zr-1,4-BDC-Aa that was heated up to 150 °C in a nitrogen-filled environmental chamber. This peak might be attributed to contaminants causing localized crystallization on the surface of the film. While a broad diffuse peak at the same angle was observed for the Zr-1,4-BDC film stored in a humidity chamber, this feature was absent in the other films.

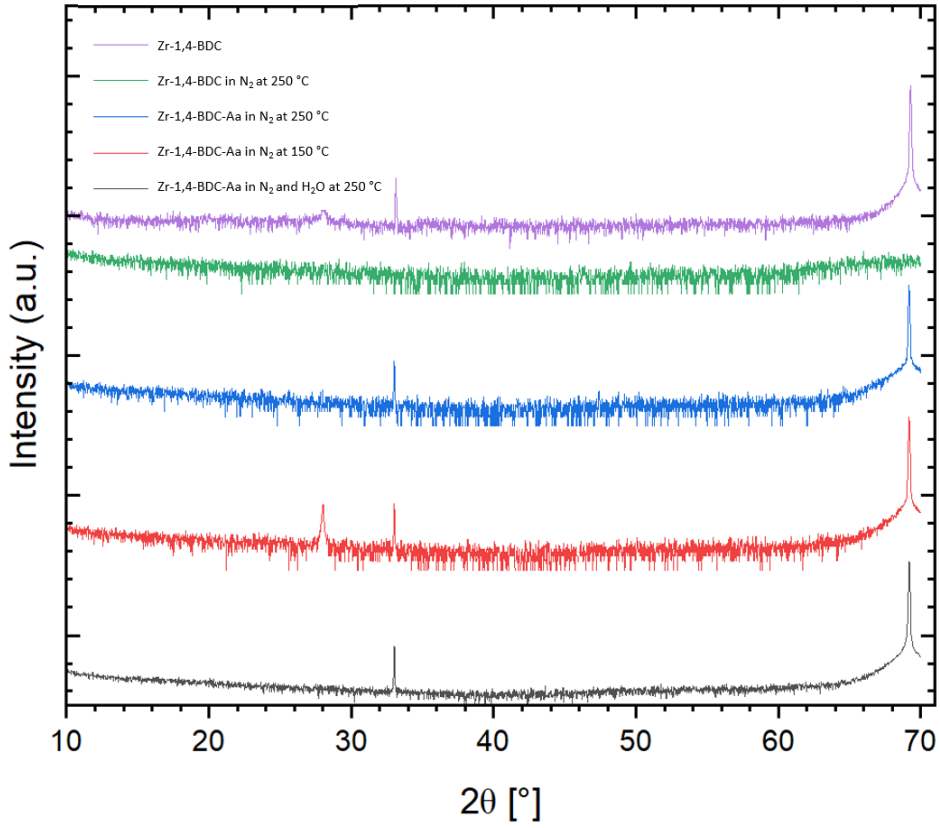

Figure 4.15: XRD spectra of a thin film that was stored in a humidity chamber (around 70% humidity) and films that were heat treated in an SE setup filled with nitrogen gas and/or water vapor.

4.2.2 Precursor Tester

A Zr-1,4-BDC film underwent heat treatment in a vacuum with temperature ranging from 20 °C - 150 °C. Pictures were taken at 30 second intervals over a 24-hour period. The purpose was to investigate the films reversibility and stability by analyzing its saturation profile at varied temperatures. The film had a thickness of 535.76 nm and an index of refraction of 1.73. The parameters for the Zr-1,4-BDC system was 2 s / 4 s / 3 s / 16 s for $ZrCl_4$ / purge / 1,4-BDC / purge. The film was deposited by 500 cycles at a reaction temperature of 265 °C. The temperature and saturation profile is presented in Figure 4.16. Images are presented in Figure 4.17 as a visual representation.

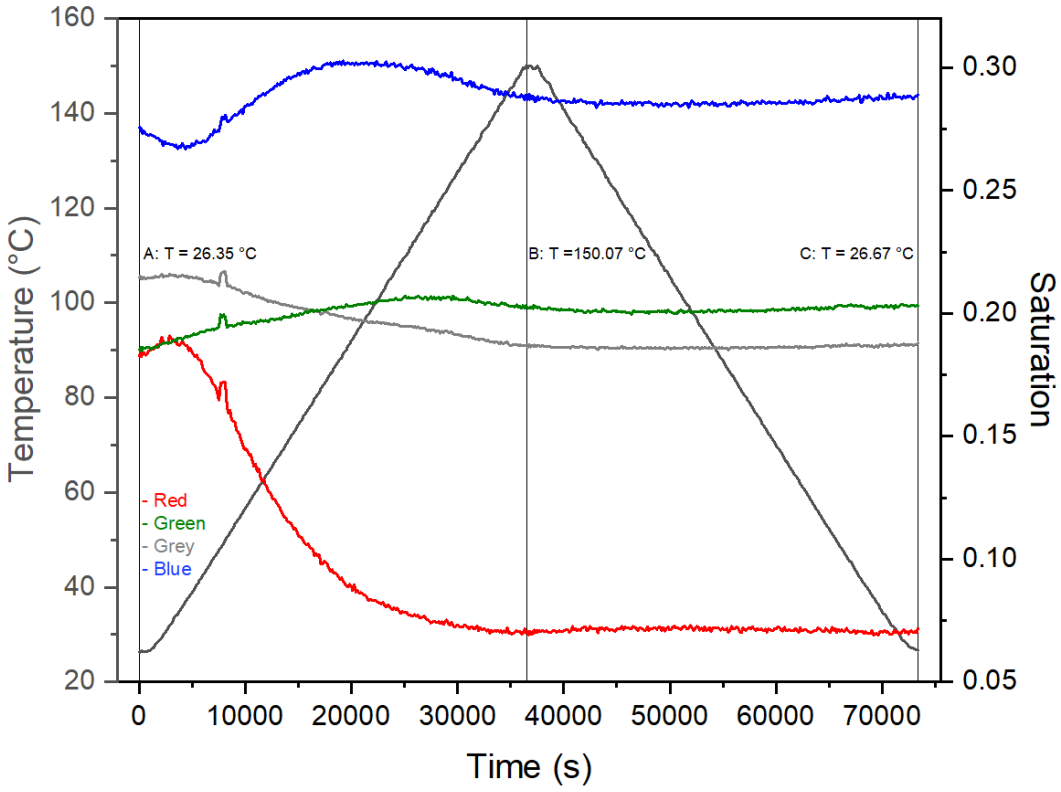

Figure 4.16: The saturation profile of Zr-1,4-BDC at temperatures ranging from 26.32°C to 150.07 °C.The vertical lines correspond to the start, middle, and end of the cycle. The change in saturation (red, green, grey, and blue) correspond to the quantity of pixels of that color within a selected area of the pictures.

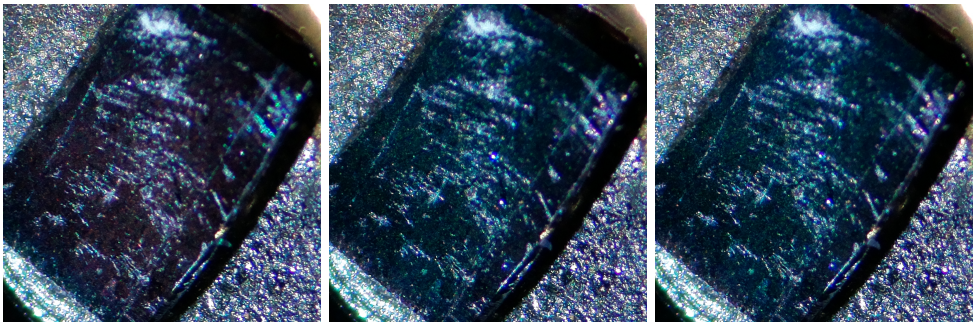

(a) The film prior to heat treatment at 26.32 °C. The majority of the film is dark purple.

(b) The film at 150.07 °C. The dark purple regions have changed to light blue.

(c) The film after a complete cycle of heat treatment. The light blue color remained.

Figure 4.17: Images taken at (a) the beginning, (b) the middle, and (c) the end of the thermal cycle.

Heat treatment of Zr-1,4-BDC highlights the sensitivity of the film to temperature. The transition from dark purple (Figure 4.17.a) to light blue (Figure 4.17.c) implies an irreversible change induced by thermal treatment. This irreversibility is corroborated by the saturation profile depicted in Figure 4.16, which shows a change in saturation from the start to the end of the cycle. The saturation profile stabilizes upon a reduction in temperature.

4.2.3 SE

Film thickness at different temperatures was analyzed by employing a Spectroscopic Ellipsometer (SE) combined with a heating plate. This specialized setup functions as an Ellipsometric porosimeter (EP) to characterize the evolution of porosity of the film. The study involved changing the temperature while monitoring the thickness of the films. Each film was kept at the designated temperatures for 2 minutes. The parameters for the Zr-1,4-BDC system was 2 s / 4 s / 3 s / 4 s for $ZrCl_4$ / purge / 1,4-BDC / purge. The parameters for the Zr-1,4-BDC-Aa system was 2 s / 4 s / 3 s / 4 s / 2 s / 10 s for $ZrCl_4$ / purge / 1,4-BDC / purge / HAc / purge. The deposition for the system with and without acetic acid was carried out at a reaction temperature of 265 °C and 245 °C, respectively. The results are presented in Figure 4.18.

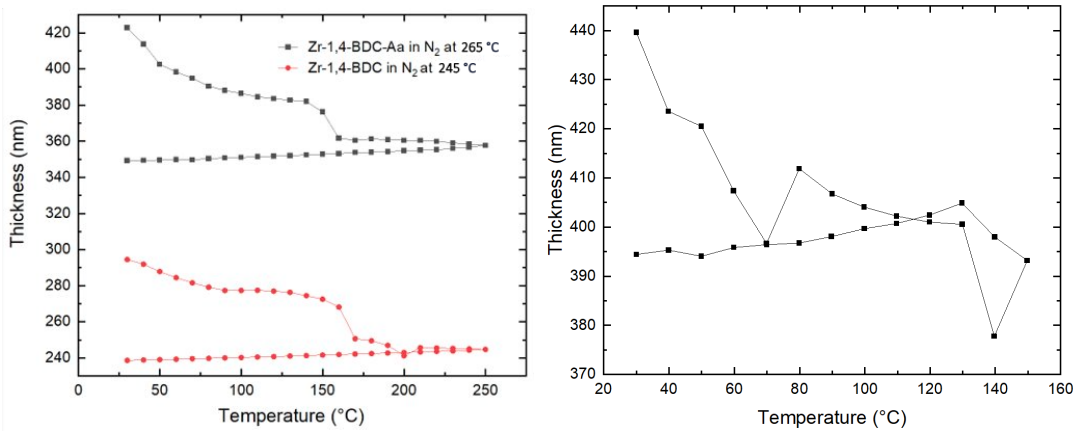

(a) SE measurements of (black) Zr-1,4-BDC-Aa and (red) Zr-1,4-BDC film, deposited at 265 °C and 245 °C using ALD, respectively, in an environmental chamber containing nitrogen gas. The temperature was varied by 10 °C increments, ranging from 30 °C to 250 °C.

(b) SE measurement of Zr-1,4-BDC-Aa, deposited at 265 °C using ALD, in an environmental chamber containing water vapor. The temperature was varied by 10 °C increments, ranging from 30 °C to 150 °C.

Figure 4.18: SE measurements of films showing film thickness as a function of temperature.

In Figure 4.18.a, it is evident that the thickness of the films decreased with increasing temperature. This highlights the films sensitivity to temperature, even at the lower temperatures. The reduction in film thickness is substantial, approximately 20%, indicating densification resulting from pore shrinkage or collapse in the amorphous film. A similar observation was made for Figure 4.18.b, although the temperature related changes in thickness were less predictable, i.e the increase in thickness by ca. 15 nm between 70 °C - 80 °C and ca. 20 nm between 140 °C - 150 °C, possibly due to condensation of water vapor on the surface of the film. Although there is an indication of reversibility between 150 °C - 130 °C, the almost linear change in thickness when the temperature is

further reduced suggests that the evolution of porosity cannot be characterized due to irreversible structural changes of the film.

We measured the thickness of films, Table 4.1, that had been stored in a humidity chamber for an extended period. The purpose was to investigate the stability of the films under controlled humidity to ensure reproducibility across measurements. This allows us to analyze how the thickness of the films changes over time. The results are presented in Figure 4.19.

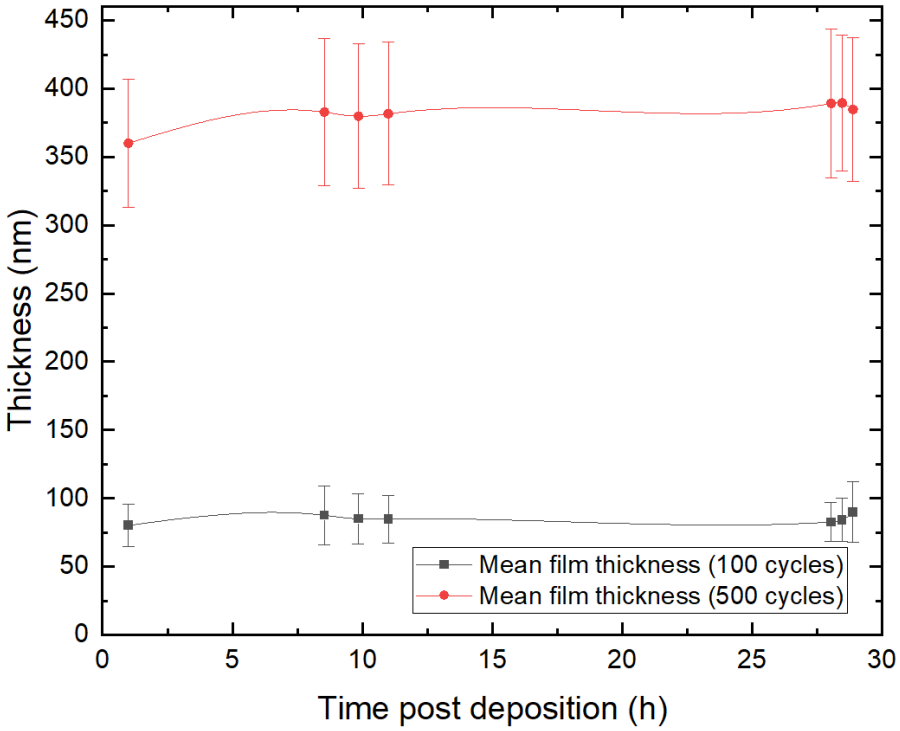

Figure 4.19: SE measurements of Zr-1,4-BDC film showing the change in film thickness as a function of time for films deposited by 100 (black) and 500 (red) cycles. The films were stored in a humidity chamber (ca. 70% humidity). The time post-deposition is expressed as $\sqrt{h}$.

It is clear that storing the films in a controlled environment resulted in minimal thickness variation. There is a noticeable increase in film thickness during the first 1-8 hours post-deposition, however, the thickness eventually stabilizes. The standard deviation for both deposition cycles is relatively consistent, indicating that all the substrates experienced comparable thickness variation.

4.2.4 FTIR

FTIR was performed on electropolished steel to investigate the bonding modes and molecular interactions that are present in the material. Figure 4.20 shows the corresponding results.

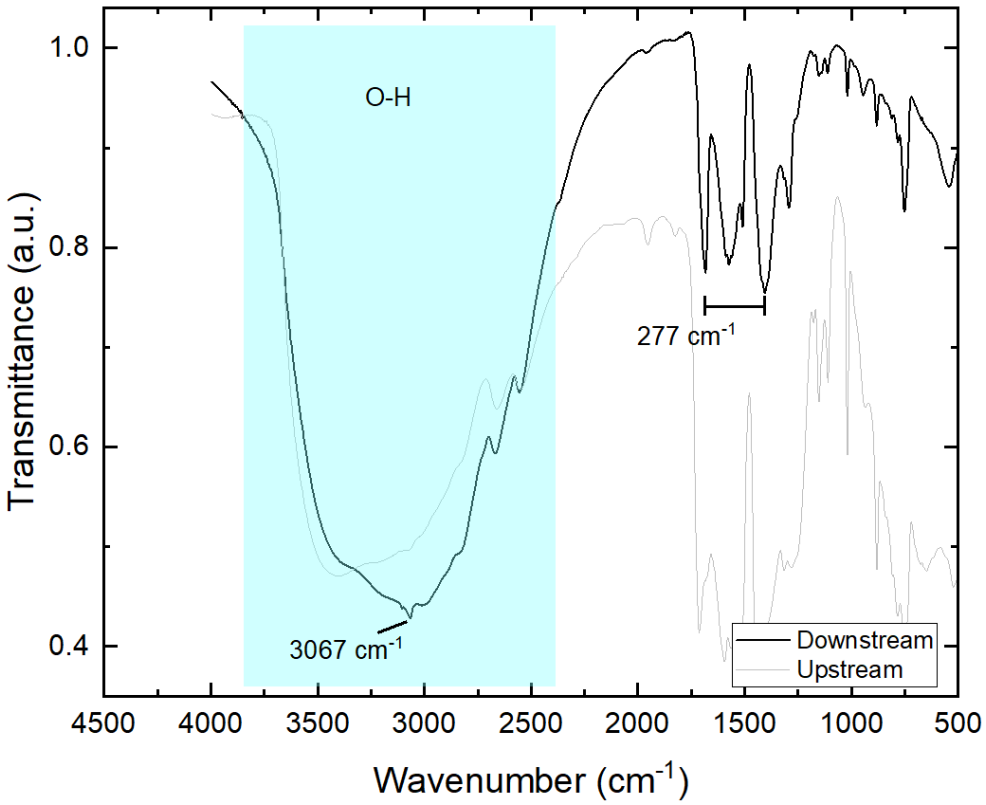

Figure 4.20: FTIR spectra for Zr-1,4-BDC with water pulsing showing films that were upstream (faint) and downstream (bold). The value for a selected peak and splitting between selected peaks are displayed.

The FTIR spectrum of Zr-1,4-BDC shows a broad absorption band with a peak at 3067 cm^{-1}. This indicates that water was absorbed into the pores of the film. The doublet observed at 1573 cm^{-1} and 1406 cm^{-1} correspond to the asymmetric (V_{as}) and symmetric (V_s) stretching modes of the carboxylate group, respectively [98].

5 Discussion

This section of the report will analyze and discuss the results presented in the previous section. The results are compared and contrasted with each other and with results from the literature.

5.1 Growth

5.1.1 ZrO_2 System

During this project, the growth process was thoroughly investigated. The first step involved obtaining an understanding of the factors that affect the films growth and the reasons for such growth under various conditions and under varying parameters. The focus for the project was directed towards the ZrO_2 system as its foundation. The purpose of this was three-fold. An investigation of such a system would provide an understanding of the reaction between $ZrCl_4$ and the terminal hydroxide atoms of the silicon substrates. This is crucial as the organic linker molecules in both UiO-66 and UiO-67 possess carboxylic acid groups that coordinate to $ZrCl_4$. Additionally, analysis of the ZrO_2 system would allow us to investigate the optimal pulse and purge time required to achieve saturation of $ZrCl_4$. This has been explored in previous publications, however, wanted to explore this further. Lastly, analysis of the ZrO_2 system would serve as the foundation for evaluating the stability and performance of the ALD instrument.

Figure 4.1 illustrates the thickness, index of refraction, and standard deviation of ZrO_2 films. The results demonstrate substantial variations in film thickness across the three substrates for a number of runs, especially run no. 4 and 11. Since the index of refraction exhibits minimal variation across three substrates, indicating that the material remains as ZrO_2, the standard deviation and percent variation for film thickness were analyzed, Table 8.2 in Appendix 8.1. In comparison to the other runs, run no. 4 and 11 show substantially larger percent variations in thickness. This could be due to the inconsistency in the placement of the substrates inside the reaction chamber. This, however, cannot account for the high standard deviation of 65% and 89% observed in run no. 4 and 11. The disparity in film thickness might be due to a variation in the temperature of the ALD instrument, Appendix 8.2. The set temperature in zones 4-8 was between 205 °C - 220 °C. It is clear that the actual temperature in zone 4 and 5 varied by up to 10 °C, zone 6 and 7 by almost 30 °C, and zone 8 by over 20 °C. The significant variations in temperature that have been observed in half of the zones certainly affect the thickness of the film. Scarel *et al.* investigated how varying the growth temperature from 165 - 350 °C affects the composition of ZrO_2 film grown using ALD [99]. They showed that the thickness of ZrO_2 film that were grown using $ZrCl_4$ and H_2O precursors on a Si(100) *p*-type wafer varied by 23% with a thickness of 26.2 nm and 20.8 nm at 200 and 250 °C, respectively. They also showed that the GPC decreased as the reaction temperature increased. At 200 and 250 °C the GPC was reported to be 0.13 and 0.10 nm/cycle, respectively. The average GPC for the ZrO_2 film over the 11 runs was 0.15 nm/cycle, which is slightly higher than the GPC values reported by Scarel *et al.* In an ideal ALD process, a constant growth rate is maintained throughout the process, showing minimal variation over time. Variations in temperature could

certainly affect the growth rate, as demonstrated by Scarel *et al.*, potentially causing the growth rate and thickness to deviate during cycles.

Statistical analysis with respect to film thickness and index of refraction, Tables 5.1 and 5.2, was conducted to interpret the data presented in Figure 4.1. The standard deviation corresponds to the variation about the mean for the 11 runs.

Table 5.1: Statistical analysis of film thickness.

Standard deviation	Mean	Min Z-score	Max Z-score
10.4	60.7	-2.2	1.3

Table 5.2: Statistical analysis of film thickness.

Standard deviation	Mean	Min Z-score	Max Z-score
0.2	2.1	-2.7	1.6

From the standard deviation and mean values presented in Tables 5.1 and 5.2, the coefficient of variation was determined to be 17% for thickness and 10% for the index of refraction. These values suggest that there is moderate variation about the mean, indicating a relatively stable dataset for both parameters. Standard scores (Z-score) were also calculated to compare the minimum and maximum film thickness and index of refraction to the overall distribution. This indicates how far the result deviates from the mean in terms of the standard deviation. The values of the minimum Z-score for both thickness and index of refraction indicate the possibility of an outlier among the 11 runs. As evident in Figure 4.1, it is clear that the mean film thickness and index of refraction for run no. 4 significantly deviates when compared to the other runs. Under the premise that data points that fall above or below 2 standard deviations are considered outliers, a minimum Z-score of -2.2 for film thickness and -2.7 for the index of refraction indicates that run no.4 is an outlier. With run no. 4 discarded, the data is revised to produce the values presented in Tables 5.3 and 5.4.

Table 5.3: Statistical analysis of film thickness excluding run no. 4.

Standard deviation	Mean	Min Z-score	Max Z-score
7.7	62.9	-2.13	1.3

Table 5.4: Statistical analysis of film thickness excluding run no. 4.

Standard deviation	Mean	Min Z-score	Max Z-score
0.1	2.2	-0.4	1.6

The revised data supports the argument that run no. 4 is an outlier. The standard deviation and the mean Z-score for both film thickness and the index of refraction decreased substantially, despite the minimum Z-score for film thickness exceeding 2 standard deviations. The coefficient of variation was also calculated with and without the inclusion of run no. 4. The coefficient of variation for film thickness changed from 17% to 12%, whereas the index of refraction changed from 10% to 5%.

The QCM response for the half-cycles in Figure 4.2 are presented as Δm_1 and Δm_2, left and right blue, dashed rectangles, respectively. The stoichiometry is determined by inspecting the mass change during the pulse and purge sequences. Since frequency changes proportionally with the change in mass, the difference between Δm_1 and Δm_2 can be compared with the mass change calculated for the reaction scheme presented in Equation (5.1) and (5.2). The QCM response for $ZrCl_4$ and H_2O resulted in a change of 2.4 and -0.4, respectively. This equates to a $\Delta m_1/\Delta m_2$ of -6.0.

$$\vdash (OH)_x + ZrCl_{4(g)} \rightarrow \vdash O_x - Zr - Cl_{(4-x)} + xHCl_{(g)} \tag{5.1}$$

$$\vdash O_x - Zr - Cl_{(4-x)} + 2H_2O_{(g)} \rightarrow \vdash O_x - Zr - (OH)_x + (4-x)HCl_{(g)} \tag{5.2}$$

- Where $\vdash$ corresponds to the film and x corresponds to the number of ligands Zr reacts with during pulses, the number of ligands Zr is bonded to following purges, and the excess molecules that have been flushed from the reaction chamber. In order to determine the stoichiometry, x was calculated using the reaction scheme and $\Delta m_1/\Delta m_2$, Appendix 8.3.1.1. An x value of 2.3 was calculated. In the system with extended pulse and purge times (Figure 4.4), the x value, using the reaction scheme in Equation (5.1) and (5.2), was determined to be 2.4, Appendix 8.3.1.2. This is very close to the ZrO_2 system with the shorter pulse and purge times which implies that prolonged exposure did not alter the stoichiometry. The reaction scheme suggests the stoichiometry of Zr:H_2O is 1:2, indicating that zirconium's coordination number is greater than 4 in ZrO_2. This is plausible since zirconium tends to have high coordination numbers [100]. An x value that is less than or equal to 2 is obtained when the stoichiometry for Zr:H_2O is 1:3. This seems more plausible, considering the porosity of ZrO_2, which could facilitate water entering and potentially incorporating into the film. Furthermore, this reaction scheme does not take into account the potential presence of residual chlorine. Merisula *et al.* conducted a study on the resistive switching behavior in dielectric films containing either multilayer ZrO_2:Al_2O_3 or ZrO_2 deposited on Zr_x:Al_yO_x [101]. Their investigation determined that films, which were grown by ALD at 300 °C, contained residual chlorine, originating from the $ZrCl_4$ precursor. At temperatures between 180-380 °C, one to two chlorine atoms were flushed from the reaction chamber per $ZrCl_4$ compound that was pulsed [102].

The density of ZrO_2 was investigated to determine the effect that chlorine atoms have on the growth rate. Densely packed chlorine atoms might limit the growth rate by partially blocking the available surface sites for precursor molecules to react with. In order to determine the effect of the chlorine atoms on the density of ZrO_2, the expected density was calculated. With a calculated

GPC of 0.15 nm/cycle, obtained from the average GPC of the data presented in Figure 4.1, the expected density, assuming that the limiting factor of the GPC is the radius of chlorine atoms, was determined to be 1.5 times larger than the true density of ZrO_2. This indicates that the chlorine atoms are in fact less densely packed than expected, Appendix 8.4. This suggests that the growth rate is slightly affected by the packing density of the chlorine atoms.

Investigation of $ZrCl_4$ growth during pulsing suggests that self-limiting growth of $ZrCl_4$ may not have occurred. This becomes clear by inspecting Figure 2.9.a. The lack of resemblance between the change in mass during the pulse illustrated in Figure 2.9.a and the change in mass during the pulse of $ZrCl_4$ in Figure 4.2 highlights this. Lausund *et al.* investigated the growth rate of Zr–BP-4,4-DC as a function of pulse and purge times at 290 °C [103]. They found that $ZrCl_4$ saturates the Si(100) surface after approximately 3 seconds. The change in mass that they observed during their investigation of self-saturating growth for $ZrCl_4$ closely resembles the change in mass that was observed in Figure 4.3. The investigation to determine the required pulse time for achieving saturation of $ZrCl_4$, Figure 4.3, indicates that while saturation of $ZrCl_4$ does occur, the steady increase in the mass of both crystal between 2 - 12 seconds could suggest incomplete or inefficient surface reactions.

Furthermore, the results align with the finding reported by Rogowska *et al*, who discovered a steady increase in the growth rate between 1-12 seconds [98]. Kukli *et al* synthesized ZrO_2 film on Si and SiO_2 substrates using H_2O and H_2O_2 as the oxygen precursor and $ZrCl_4$ as the metal precursor [104] They discovered that the adsorption of $ZrCl_4$ did not exhibit complete self-limiting behavior as the QCM response continued to increase even when the pulse was prolonged to 40 seconds. This was observed for depositions carried out between 250 - 500 °C. This phenomena was also observed by Aarik *et al*, who discovered that despite complete saturation of $ZrCl_4$ not occurring within a 40 second pulse, the change in mass increased rapidly and then began to stabilize [105]. Despite the persistent challenge of achieving self-limiting $ZrCl_4$ growth, extensive research is still being conducted on the applications of ALD materials utilizing $ZrCl_4$ precursors [101, 106, 107].

5.1.2 Zr-1,4-BDC System

The QCM investigation of the Zr-1,4-BDC system shows that reproducible growth was achieved, as evidenced by the almost identical GPCs in Table 4.1. Despite this, there are slight variations in the refractive index, which could indicate that the materials do not have identical compositions. The GPC of 0.7 - 0.9 nm/cycle is higher than expected, when comparing to previous studies conducted by Lausund *et al.*, who reported a GPC of approximately 0.6 - 0.7 nm/cycle [10]. A QCM investigation with identical pulse and purge times, which were chosen according to a successful deposition conducted by Lausund [17], was carried out to determine the reaction scheme of the Zr-1,4-BDC System. The QCM response for the cycles in Figure 4.5 are presented as Δm_1 and Δm_2, left and right blue, dashed rectangles, respectively. The reaction scheme is determined by inspecting the mass change during the pulse and purge sequences. The QCM response for $ZrCl_4$ and 1,4-BDC resulted in a change in mass of 1.5 and 2.1, respectively. This equates to a $\Delta m_1/\Delta m_2$ of 0.7. This value can be compared to the calculated mass change for the reaction scheme presented in Equation (5.3) and (5.4).

$$\vdash (OH)_x + ZrCl_{4(g)} \rightarrow \vdash O_x - Zr - Cl_{(4-x)} + xHCl_{(g)} \tag{5.3}$$

$$\vdash O_x - Zr - Cl_{(4-x)} + 2C_6H_4(COOH)_{2(g)} \rightarrow \vdash O_x - Zr - (C_6H_4O_{\frac{8-x}{2}})_2(OH)_x + (4-x)HCl_{(g)} \tag{5.4}$$

By solving for x using the reaction scheme presented and $\Delta m_1/\Delta m_2$, an x value of 1.6 was obtained, as indicated in Appendix 8.3.2, which is very close to reported data [10]. The 5 second 1,4-BDC pulse yielded an increase in response that is fundamentally due to chemisorption. Although there is a rapid reduction in response for approximately 2 seconds, corresponding to just below 2 Hz, during the subsequent purge, the response eventually stabilizes. This could be due to a low reaction temperature. This investigation was conducted at 245 °C, whereas, Lausund investigated the mass increase as a function of time for the same system at 265 °C [17]. He observed that a more stable reduction in mass occurs during the 1,4-BDC purge. At low reaction temperatures, some precursor molecules lack sufficient thermal energy to break existing bonds and form new chemical bonds. As a result, some adsorbate molecules adhere through weak Van der Waals forces, leading to physisorption.

The QCM investigation of saturation versus pulse time for 1,4-BDC in Figure 4.6 shows a rapid increase in mass which is a good indication of ALD growth. Both signals for sensor A and B increase at approximately the same rate, however deviation in mass is observed after 5.5 seconds. Higher mass is observed for sensor B since the sensor is located at the inlet. This suggests a concentration gradient in the reaction chamber, where a higher concentration is expected at the inlet than at the outlet.

The QCM investigation examining the effect of water on Zr-1,4-BDC revealed that pulsing water as part of the precursor sequence resulted in overall less growth. The system without water pulse, Figure 4.5, shows an overall growth of 32 Hz. The systems with water pulse, Figure 4.7.a and b, exhibit an overall growth of 25 Hz and 20 Hz, respectively. The stoichiometry of the $ZrCl_4$+H_2O+1,4-BDC system was examined by using the reaction scheme outlined in Equation (5.5 - 5.7). The deposition of three precursors makes it challenging to determine a suitable value for x that satisfies all three equations. To mitigate this challenge, an assumption was made that there was excess water in the system, as confirmed by the FTIR data in Figure 4.20.

$$\vdash -(OH)_x + ZrCl_{4(g)} \rightarrow \vdash -O_x - Zr - Cl_{(4-x)} + xHCl_{(g)} \tag{5.5}$$

$$\vdash -O_x - ZrCl_{(4-x)} + 2(H_2O)_{(g)} \rightarrow \vdash -O_x - Zr(OH)_{4-x} + (4-x)HCl_{(g)} \tag{5.6}$$

$$\begin{aligned} \vdash -O_x - Zr(OH)_{4-x} + C_6H_4(COOH)_{2(g)} \rightarrow \vdash & -O_x - Zr - O_{4-x} - (C_6H_4O_{\frac{4-x}{2}})(OH)_x \\ & + (3-x)H_2O_{(g)} \end{aligned} \tag{5.7}$$

By setting $x = 1$ in Equation (5.5), the observed and calculated QCM response for Δm_2, Equation (5.6), become equivalent when 3 water molecules react with the surface. An investigation of a 1:1 and a 1:2 stoichiometry for Zr-1,4-BDC was conducted to match the observed and calculated QCM response. This led to the determination that 0.96 molecules of 1,4-BDC react with 1 zirconium atom to give an overall stoichiometry of 1:1 when water is pulsed between pulses of $ZrCl_4$ and 1,4-BDC. The QCM response for Figure 4.7.a, where the reaction temperature was 245 °C, shows that a reduction in mass occurs when water is pulsed after the 1,4-BDC cycle. This indicates etching of 1,4-BDC. Ahmadijokan *et al.* proposed UiO-66's significant potential for water-based applications owing to its remarkable thermal stability [16]. Although Zr-1,4-BDC and UiO-66 are distinct in their crystal structures, the observed etching of 1,4-BDC at 245 °C contradicts this proposal.

5.1.3 Zr-BP-4.4-DC System

In order to adequately assess the reactivity and stability of Zr-BP-4,4-DC, it is necessary to ensure that the self-limiting potential of the process is maximized. Since the growth should be dependent on the adsorption of precursor molecules rather than the growth conditions, the self-limiting behavior cannot be maximised until the process becomes independent of growth conditions. Therefore, the decision was made to initially investigate the saturation versus pulse time for BP-4,4-DC to ensure that saturation of BP-4,4-DC occurred in the ensuing depositions. Building upon previous investigations of saturation versus pulse time for 1,4-BDC, a similar change in mass for BP-4,4-DC was expected due to the similar chemical structures of these compounds. In Figure 4.8, the growth rate of BP-4,4-DC in sensor B increased with increasing pulse time. However, it is evident that saturation was not reached as rapidly as expected. Comparison between the QCM response in Figure 4.6 and 4.8 shows that the mass of 1,4-BDC, deposited at 245 °C, increased more rapidly than the mass of BP-4,4-DC. Lausund suggested that the slow saturation could be attributed to the lower vapor pressure of the bulkier molecule [17]. Faster saturation of BP-4,4-DC could be achieved by increasing the reaction temperature, however this may lead to decomposition. Lausund also suggested that slow saturation could be an indication of steric hindrance. A simplified illustration of how steric hindrance affects saturation is presented in Figure 5.1.

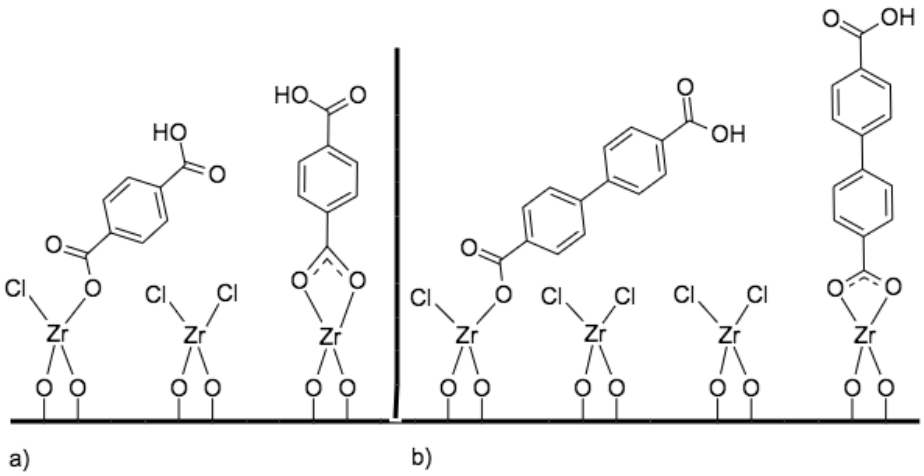

Figure 5.1: A simplified schematic drawing of steric hindrance induced by tilted orientation of (a) 1,4-BDC and (b) BP-4,4-DC. BP-4,4-DC partially blocks more binding sites, compared to 1,4-BDC due to its greater length. Inspired by [17].

Steric hindrance, induced by tilted orientation, can result in the partial blocking of reaction sites. When molecules exhibit monodentate coordination to zirconium, titled orientation occurs. Combined with the longer length of the BP-4,4-DC molecular structure, measuring 4.3 Å more than 1,4-BDC, the steric effect is more pronounced in monodentate coordinated organic linker [17].

The stoichiometry for the cycle in Figure 4.10 was determined by inspecting the mass change during the pulse and purge sequences. The QCM response for $ZrCl_4$ and BP-4,4-DC resulted in a change in mass of 1.5 and 2.5, respectively. This equates to a $\Delta m_1/\Delta m_2$ of 0.6. This value can be compared to the calculated mass change for the reaction scheme presented in Equation (5.8) and (5.9).

$$\vdash (OH)_x + ZrCl_{4(g)} \rightarrow \vdash O_x - Zr - Cl_{(4-x)} + xHCl_{(g)} \tag{5.8}$$

$$\begin{gathered} \vdash O_x - Zr - Cl_{(4-x)} + 2C_{12}H_8(COOH)_{2(g)} \rightarrow \\ \vdash O_x - Zr - (C_{12}H_8O_{\frac{8-x}{2}})_2(OH)_x + (4-x)HCl_{(g)} \end{gathered} \tag{5.9}$$

By solving for x using the reaction scheme presented and $\Delta m_1/\Delta m_2$, an x value of 0.5 was obtained, Appendix 8.3.3. This indicates that the stoichiometry of Zr:BP-4,4-DC is not 1:2, since at least one chlorine atom must react. It is also not possible to describe the mass variation of $ZrCl_4$ by the reaction scheme because it assumes that 50% of the $ZrCl_4$ molecules are physisorbed. With the assumption that the stoichiometry is 1:1, the reaction scheme becomes:

$$\vdash (OH)_x + ZrCl_{4(g)} \rightarrow \vdash O_x - Zr - Cl_{(4-x)} + xHCl_{(g)} \tag{5.10}$$

$$\begin{gathered} \vdash O_x - Zr - Cl_{(4-x)} + C_{12}H_8(COOH)_{2(g)} \rightarrow \\ \vdash O_x - Zr - (C_{12}H_6O_{4-x})(OH)_x + (4-x)HCl_{(g)} \end{gathered} \tag{5.11}$$

where $x = 3$, which is within the expected range of 1-3 [17].

The investigation focused on determining the number of cycles necessary to achieve standard stable growth of Zr-BP-4,4-DC by depositing the hybrid material on porous ZrO_2. The result is presented in Figure 4.11. It was determined that 4 cycles were required to achieve standard stable growth of Zr-BP-4,4-DC on sensor A and 3 or 4 cycles on sensor B. A few interpretations can be deduced from these results. Firstly, the deposition process exhibited minimal variation. This is supported by the resemblance in the growth rate after the fourth cycle, especially in sensor A. In addition, ZrO_2 displayed minimal, if any, chemical reactivity during the growth of Zr-BP-4,4-DC. The deposition of ZrO_2 on Zr-BP-4,4,-DC, however, showed that Zr-BP-4,4-DC was still chemically active even after 200 cycles of ZrO_2. Under normal conditions, i.e. on non-porous coating, the film thickness should be equivalent to approximately 30 nm.

MOF's such as NH_2-UiO-66 and UiO-66 are known for their hydrothermal and chemical stability towards water and air [108]. However, a comparative study conducted by Leus *et al.* on the stability of various MOFs under different conditions reported that UiO-67, synthesized by solvothermal method, based on the procedure by Katz *et al.* [109], is not suitable for applications requiring high stability in the presence of water [110]. Accordingly, the decision was made to investigate the effect of water on Zr-BP-4,4-DC by varying the water sequence. The QCM response of Figure

4.12.a indicates that although water enters the pores of the hybrid film, some of it remains after purging has concluded. With the assumption that there is a delay in the instrument, the signal prior to the water pulse was 37 Hz. This increased to 44 Hz after pulsing and decreased to 39.5 Hz at the end of purging, indicating that 35% of the water that entered the pores remained after purging. This can be due to the porosity of the amorphous Zr-BP-4,4-DC. Lausund proposed that amorphous Zr-1,4-BDC has less accessible pores than crystalline UiO-66 film causing slower kinetics for water to get out of the pores [17]. A similar outcome should be expected for amorphous Zr-BP-1,4-DC. This is further supported by the QCM response of figure 4.13.b, which shows all of the water getting out of the pores with extended purging. Figure 4.12.b indicates that BP-4,4-DC encounters difficulty in adsorbing onto an OH-terminated surface, as shown by a shallower slope compared to previous depositions without water, which had a steeper slope.

In the past, acetic acid has been used as a modulating agent of wet-based MOFs to promote crystallization. While ALD and wet-based methods, such as solvothermal synthesis, differ fundamentally, it has been reported that acetic acid can serve as a solvent or stabilizing agent in various chemical environments [111, 112]. Furthermore, it has been reported that depositing acetic acid after the deposition of BP-4,4-DC results in the removal of excess linker molecules [17]. An investigation of the modulating effect of acetic acid on $ZrCl_4$ was conducted to see how this affects the growth of BP-4,4-DC, Figure 4.14. The QCM response shows a rapid increase followed by a rapid decrease in mass during acetic acid pulsing. This could be due to acetic acid coordinating to and dissociating from zirconium. During pulsing, the mass continues to decrease. This could indicate that, in addition to acetic acid dissociating from zirconium, zirconium (IV) acetate hydroxide is also dissociating as a result of etching reactions caused by the HCl byproduct. A simplified overview of the acetic acid pulse and the reactions that occur is presented in Figure 5.2.

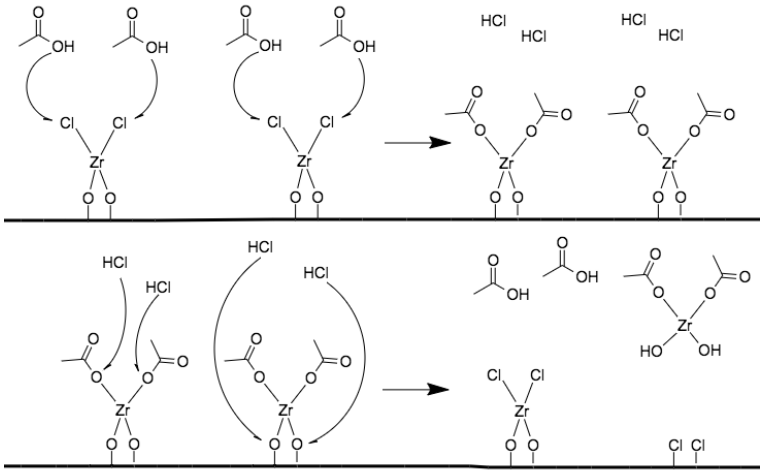

Figure 5.2: A simplified illustration of the reactions that occur during the acetic acid pulse. During pulsing, acetic acid coordinates to zirconium leading to the formation of the byproduct HCl (above). HCl, however, reversibly reacts leading to chemical etching (below). Inspired by [113].

5.2 Characterization

The porosity of thin films can be characterized using various methods, one of which involves measuring the water uptake and release on a QCM crystal in an ALD reactor [103]. An alternative approach involves characterizing the surface area using the Brunauer-Emmett-Teller (BET) method by measuring the adsorption of nonreactive gases such as nitrogen [114]. The EP approach combined with a heating plate was employed to characterize the evolution of the films porosity. The results, presented in Figure 4.18, indicate that irreversible structural changes occurred. Figure 4.18.a illustrates that the variation in film thickness during thermal treatment is nearly indistinguishable for Zr-1,4-BDC with and without acetic acid. As previously mentioned, acetic acids capability to remove monodentate-coordinated 1,4-BDC, leaving only those with bidentate coordination has been previously reported [17]. The comparable change in thickness at similar temperatures for both films suggests that modulation with acetic acid was not effective. In a system with a higher proportion of bidentate-coordinated organic linkers, one would expect a less pronounced decrease in thickness due to the stronger coordination between the linkers and the substrate. Figure 4.18.b also shows an irreversible structural change in the film. This could be attributed to improper activation. Mondloch *et al.* reported that improper activation of UiO-67 from water resulted in the complete loss of porosity [14]. This suggests that densification, possibly due to pore shrinkage, may have occurred. Thus, the investigation could have been improved by treating the films in acetic acid vapor, in a procedure akin to that described by Lausund in his PhD thesis [17], instead of water vapor and/or nitrogen gas. Lausund determined that treatment of Zr-1,4-BDC in an autoclave with acetic acid vapor produced highly crystalline UiO-66 films.

Investigation of the saturation profile of amorphous Zr-1,4-BDC further illustrates the films inability to maintain structural integrity, Figure 4.16. However, storage of Zr-1,4-BDC in a humidity chamber demonstrated that the amorphous films are stable at room temperature, as shown in Figure 4.19, suggesting that the amorphous films lack thermal stability. In contrast to the challenges faced in the investigation of the optical properties of Zr-1,4-BDC due to the presence of interference fringes that obscured the absorption peaks (see Appendix 8.6), FTIR provided an insight into the bonding characteristics of Zr-1,4-BDC with water pulsing. Verpoort *et al.* observed that the prominent peaks at approximately 1,400 cm^1 and 1,500–1,700 cm^1 provide insights into the coordination modes of 1,4-BDC to zirconium [115]. A splitting range of 50 - 150 cm^1 indicates a bidentate coordination complex, a splitting range of 130 - 200 cm^1 indicates a bridging complex, and splitting exceeding 200 cm^1 indicates a monodentate coordination complex. Consequently, the observed splitting value of 277 cm^1, Figure 4.20, suggests monodentate coordination of 1,4-BDC to zirconium. This is further corroborated by Lausund *et al.* who suggested that the broad absorption band with a peak at 3067 cm^1 may arise from OH groups on monodentate 1,4-BDC molecules [10].

6 Conclusion

The objective of this project was to develop porous coatings for chromatography enhanced sensors. This involved characterization of the growth dynamics of ZrO_2, Zr-1,4-BDC, and Zr-BP-4,4-DC to determine the most favorable growth conditions for synthesizing UiO-66 and UiO-67 thin films.

ZrO_2 thin films were deposited using $ZrCl_4$ and H_2O precursors, exhibiting an average GPC of 0.15 nm/cycle indicating higher growth than expected. Achieving uniform ZrO_2 growth with controlled chemistry proved more challenging than anticipated. Synthesis of this film with reproducible growth was unsuccessful due to its porosity. Moreover, significant variations in film thickness and refractive index indicated the films susceptibility to temperature variations during synthesis. An investigation into the potential limitation of ZrO_2 growth by densely packed chlorine atoms revealed that growth was not limited by the radius of chlorine atoms.

Uniform growth of Zr-1,4-BDC films was achieved with varied number of cycles and pulse and purge times, yielding a GPC of 0.7-0.9 nm/cycle. Investigation into the growth rate of $ZrCl_4$ as a function of pulse time indicated that although saturation occurs at approximately 0.25 seconds, longer exposure led to continued growth. Investigation of Zr-1,4-BDC with water pulsing revealed that pulsing water as part of the precursor sequence resulted in an overall reduced growth. A stoichiometry of 1:1 was achieved when 1,4-BDC was deposited on an OH-terminated surface, while the stoichiometry was determined to be 1:2 without water pulsing. Pulsing water as part of the precursor sequence in a Zr-1,4-BDC system indicated etching of 1,4-BDC. Thermal treatment of Zr-1,4-BDC with and without acetic acid pulsing led to irreversible structural changes. The change in thickness for these systems at comparable temperatures indicated that acetic acid was ineffective at removing monodentate coordinated linker molecules. The FTIR spectrum of Zr-1,4-BDC revealed that the system exhibits monodentate coordination, as evidenced by the large splitting range between the asymmetric and symmetric stretching modes of the carboxylate group.

QCM analysis of the Zr-BP-4,4-DC system showed that BP-4,4-DC reaches saturation much slower than 1,4-BDC, indicating that sufficiently longer pulse times are required to achieve saturation. Postulation between two reaction mechanisms revealed a stoichiometry of 1:1 for Zr-BP-4,4-DC. While standard stable growth of Zr-BP-4,4-DC was achieved within 4 cycles following its deposition on the surface of porous ZrO_2 film, the deposition of ZrO_2 on Zr-BP-4,4-DC film showed that the hybrid film was chemically active even after 200 consecutive cycles of ZrO_2 deposition. To gain insights into the stability and morphology of Zr-BP-4,4-DC, the effect of introducing water as part of the precursor sequence was investigated. This revealed the need for a sufficiently long water purge to effectively remove any water that has entered the pores of the film.

7 Future Work

The aim of this project was to develop growth of UiO-66 and UiO-67 thin films with tunable porosity and controlled chemistry. While this investigation provided valuable insight into the intricacies of the systems, several aspects will require additional attention. It was discovered that developing ZrO_2 film with reproducible growth was challenging due to the porosity of the film. An understanding of the growth dynamics of ZrO_2 is foundational for achieving reproducible growth of Zr-1,4-BDC and Zr-BP-4,4-DC with tunable porosity and controlled chemistry. If the chemical activity of Zr-BP-4,4-DC is to be investigated further, *in-situ* SE characterization of ZrO_2 deposition on a Zr-BP-4,4-DC film should be carried out as this can provide insight into the evolution of porosity of ZrO_2 and how that affects the chemical activity of Zr-BP-4,4-DC. Moreover, this would allow a study of the layer-by-layer growth and material properties of the system.

It was discovered that an almost identical change in film thickness occurred when Zr-1,4-BDC was deposited with and without acetic acid as part of the precursor sequence, indicating that the modulator was ineffective at removing linker molecules with monodentate coordination to zirconium. If the modulating capability of acetic acid is to become an integral part of the deposition process during the synthesis of UiO-66 and UiO-67 thin films, Nuclear Magnetic Resonance (NMR) spectroscopy of the hybrid materials with acetic acid modulation should be carried out to reveal information about the coordination changes induced by acetic acid.

Thermal treatment of amorphous Zr-1,4-BDC, conducted using SE equipped with an environmental chamber, led to irreversible structural changes in the films. Post-deposition autoclave treatment of Zr-1,4-BDC films in acetic acid vapor following a method similar to the one described by Lausund in his doctoral thesis may produce Zr-1,4-BDC film with enhanced structural integrity [17]. This improvement may allow characterization of the films porosity by the specialized EP approach. The natural next step is to compare the porous materials capacity to separate chemicals through chromatography such as Thin layer Chromatography (TLC), with the aim to eventually develop porous coatings for chromatography enhanced sensor.

8 Appendix

8.1 ZrO_2 system - Growth

Table 8.1: The run, thickness (nm), and index of refraction of the average film growth for Figure 4.1.

Run	Thickness (nm)	Index of refraction
1	55.73	2.20
2	59.21	2.16
3	46.49	2.15
4	38.22	1.49
5	66.51	2.15
6	63.97	2.16
7	61.35	2.14
8	66.65	2.14
9	68.26	2.14
10	73.71	2.49
11	67.06	2.15

Table 8.2: Statistical data related to the film thickness of Figure 4.1.

Run	Thickness standard deviation	Variation (%)
1	8.21	23
2	1.22	4
3	1.32	5
4	13.17	65
5	3.64	11
6	2.4	7
7	3.71	9
8	1.57	5
9	3.43	9
10	5.86	11
11	30.97	89

8.2 Temperature log for the deposition campaign of the ZrO_2 system

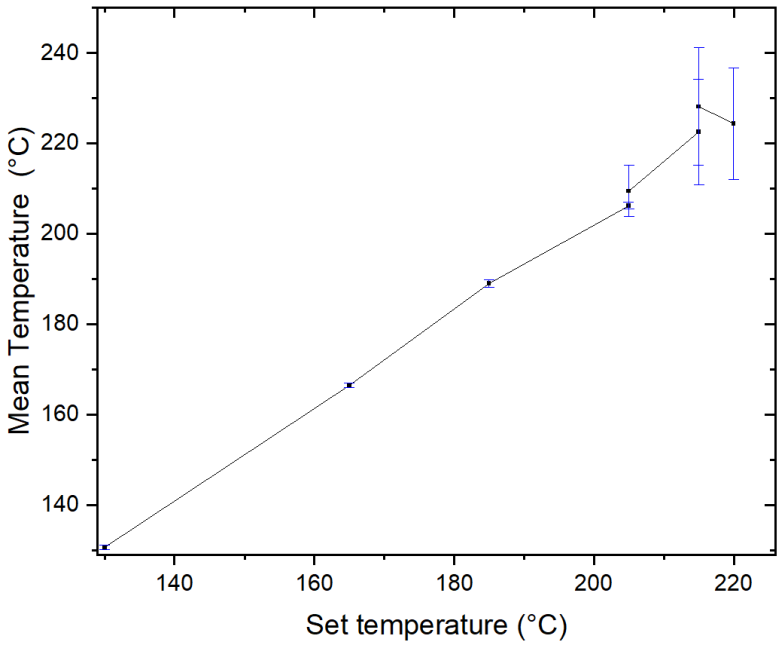

Figure 8.1: Real temperature of temperature zones in ALD reactor against set temperature.

8.3 Stoichiometry calculations

The following calculations are carried out in order to obtain relevant information from the QCM analysis presented in the results section of this report. By solving for x, which represents the surface ligands zirconium react with, an analysis of the change in signal for the half cycles can be used to determine the stoichiometry of zirconium to surface ligands.

8.3.1 ZrO_2 system

8.3.1.1 Short QCM cycle of ZrO_2 growth

The change in mass is calculated from the following equations:

$$\Delta m_1 = M_r(ZrCl_4) - xM_r(HCl) = 2.4$$
$$\Delta m_2 = 2M_r(H_2O) - (4-x)M_r(HCl) = -0.4$$

By combining the two equations and solving for x, the following equations are produced:

$$\frac{\Delta m_1}{\Delta m_2} = \frac{M_r(ZrCl_4) - xM_r(HCl)}{2M_r(H_2O) - (4-x)M_r(HCl)}$$

$$x = \frac{M_r(ZrCl_4) + (4M_r(HCl) - 2M_r(H_2O))\frac{\Delta m_1}{\Delta m_2}}{(\frac{\Delta m_1}{\Delta m_2} + 1)M_r(HCl)}$$

The x value is determined by combining $\frac{\Delta m_1}{\Delta m_2} = -6.00$ with the molecular mass values presented in the table below:

Table 8.3: Molecular mass of molecules used for calculating the x value.

Molecule	Molecular mass (g/mol)
$ZrCl_4$	233.04
HCl	36.46
H_2O	18.02

Which gives an x value of 2.3

8.3.1.2 Long QCM cycle of ZrO_2 growth

The change in mass is calculated from the following equations:

$$\Delta m_1 = M_r(ZrCl_4) - xM_r(HCl) = 3.7$$
$$\Delta m_2 = 2M_r(H_2O) - (4-x)M_r(HCl) = -0.6$$

By combining the two equations and solving for x, the following equations are produced:

$$\frac{\Delta m_1}{\Delta m_2} = \frac{M_r(ZrCl_4) - xM_r(HCl)}{2M_r(H_2O) - (4-x)M_r(HCl)}$$

$$x = \frac{M_r(ZrCl_4) + (4M_r(HCl) - 2M_r(H_2O))\frac{\Delta m_1}{\Delta m_2}}{(\frac{\Delta m_1}{\Delta m_2} + 1)M_r(HCl)}$$

The x value is determined by combining $\frac{\Delta m_1}{\Delta m_2} = -6.2$ with the molecular mass values presented in the table below:

Table 8.4: Molecular mass of molecules used for calculating the x value.

Molecule	Molecular mass (g/mol)
$ZrCl_4$	233.04
HCl	36.46
H_2O	18.02

Which gives an x value of 2.4

8.3.2 Zr+1,4-BDC system

The change in mass is calculated from the following equations:

$$\Delta m_1 = M_r(ZrCl_4) - xM_r(HCl) = 1.5$$
$$\Delta m_2 = 2M_r(1,4-BDC) - (4-x)M_r(HCl) = 2.1$$

By combining the two equations and solving for x, the following equations are produced:

$$\frac{\Delta m_1}{\Delta m_2} = \frac{M_r(ZrCl_4) - xM_r(HCl)}{2M_r(1,4-BDC) - (4-x)M_r(HCl)}$$

$$x = \frac{M_r(ZrCl_4) + (4M_r(HCl) - 2M_r(1,4-BDC))\frac{\Delta m_1}{\Delta m_2}}{(\frac{\Delta m_1}{\Delta m_2} + 1)M_r(HCl)}$$

The x value is determined by combining $\frac{\Delta m_1}{\Delta m_2} = 0.7$ with the molecular mass values presented in the table below:

Table 8.5: Molecular mass of molecules used for calculating the x value.

Molecule	Molecular mass (g/mol)
$ZrCl_4$	233.04
HCl	36.46
1,4-BDC	166.13

Which gives an x value of 1.6.

8.3.3 Zr+BP-4,4-DC system

The change in mass is calculated from the following equations:

$$\Delta m_1 = M_r(ZrCl_4) - xM_r(HCl) = 1.5$$
$$\Delta m_2 = 2M_r(BP-4,4-DC) - (4-x)M_r(HCl) = 2.5$$

By combining the two equations and solving for x, the following equations are produced:

$$\frac{\Delta m_1}{\Delta m_2} = \frac{M_r(ZrCl_4) - xM_r(HCl)}{2M_r(BP-4,4-DC) - (4-x)M_r(HCl)}$$

$$x = \frac{M_r(ZrCl_4) + (4M_r(HCl) - 2M_r(BP-4,4-DC))\frac{\Delta m_1}{\Delta m_2}}{(\frac{\Delta m_1}{\Delta m_2}+1)M_r(HCl)}$$

The x value is determined by combining $\frac{\Delta m_1}{\Delta m_2} = 0.6$ with the molecular mass values presented in the table below:

Table 8.6: Molecular mass of molecules used for calculating the x value.

Molecule	Molecular mass (g/mol)
$ZrCl_4$	233.04
HCl	36.46
BP-4,4-BDC	242.23

Which gives an x value of 0.5.

8.4 Packing density calculations

The packing density is determined by assuming that the chloride ions are arranged in a desne hexagonal packing:

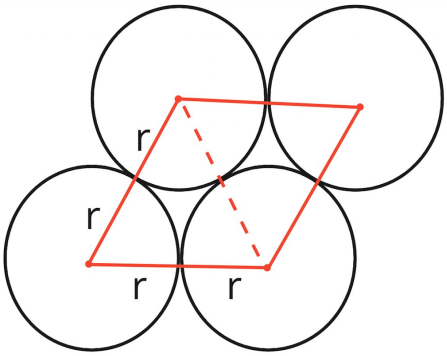

The theoretical and calculated values, below, are used to determine the packing density:

Table 8.7: Theoterical and calulated values used for determining density.

Theoretical values	Observed value
Density of ZrO_2: 5.68 g/cm^2	GPC: 0.150 nm
Radius of Cl^- ion: 0.167 nm	
Molecular mass of ZrO_2: 123.22 g/mol	

We determine the area of the four lattice points, image above, from the radius of chlorine ions:

$$Area = \frac{\sqrt{3}}{2}(2r)^2$$

To obtain:

$$Area = 9.66 \bullet 10^{-2} \frac{nm^2}{Cl^-}$$

Since zirconium has a 1:1.67 ratio with chlorine atoms:

$$Area \bullet 1.67 = 0.161 \frac{nm^2}{Zr}$$

The volume is determined by multiplying the GPC with the area:

$$Volume = 0.150nm \bullet 0.161 \frac{nm^2}{Zr} = 0.02415 \frac{nm^3}{Zr}$$

We obtain the density from the molecular mass of ZrO_2 and the volume:

$$\rho = \frac{\frac{123.22\frac{g}{mol}}{6.022\bullet 10^{23} mol^{-1}}}{0.02415(10^{-7})^3 cm^3} = 8.47 g/cm^3$$

We then divide the density of $ZrCl_4$ with the density of ZrO_2 to give 1.5 g/cm^3.

8.5 Capping of Zr-BP-4,4-DC with ZrO_2

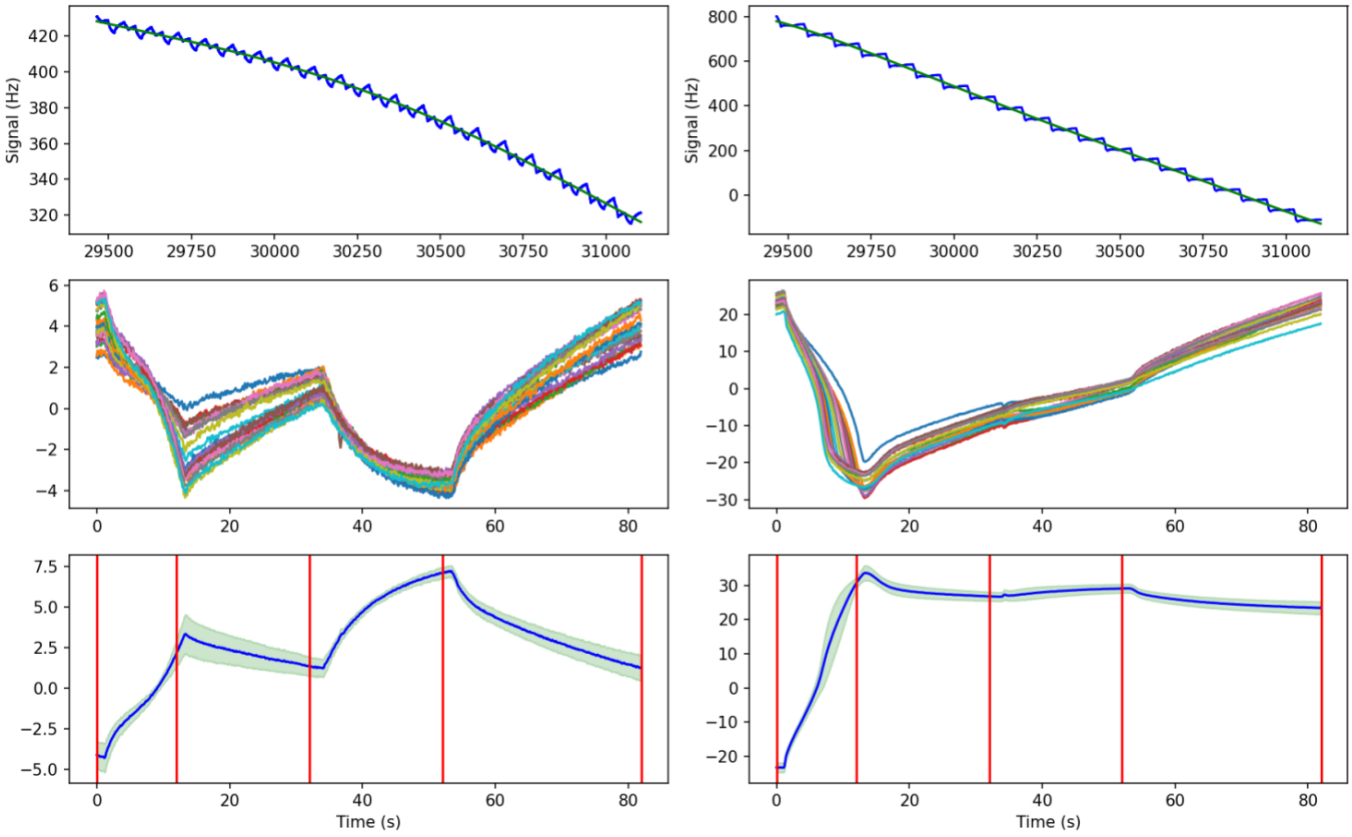

Figure 8.2: QCM of BP-4,4-DC capping with ZrO_2 showing the absence of well-defined ZrO_2 growth after 200 cycles.

8.6 Stoichiometry calculation for Zr-1,4-BDC with water pulsing

To determine the x value for Equation (5.5) and (5.6), We manipulate x to match $\Delta m_1/\Delta m_2$ with the observed change in mass. These become equivalent when the change in mass for Equation (5.5) and (5.6) is 196.58 and -54.02 g/mol, which corresponds to an x value of 1 and 1.54, respectively. This information is then used to match $\Delta m_2/\Delta m_3$. The change in mass for Equation (5.7) is 123.49 g/mol when the stoichiometry is 1:1 for Zr:1,4-BDC.

8.7 Characterization

8.7.1 UV-Vis of Zr-1,4-BDC

UV-Vis spectroscopy was used to measure transmission and reflectivity of Zr-1,4-BDC on a glass plate. This was used to determine absorbance as outlined in Equation (2.4). Measurements were taken from various positions on the glass plate, while a clean glass plate was used as a reference. The data is presented in Figure 4.22.

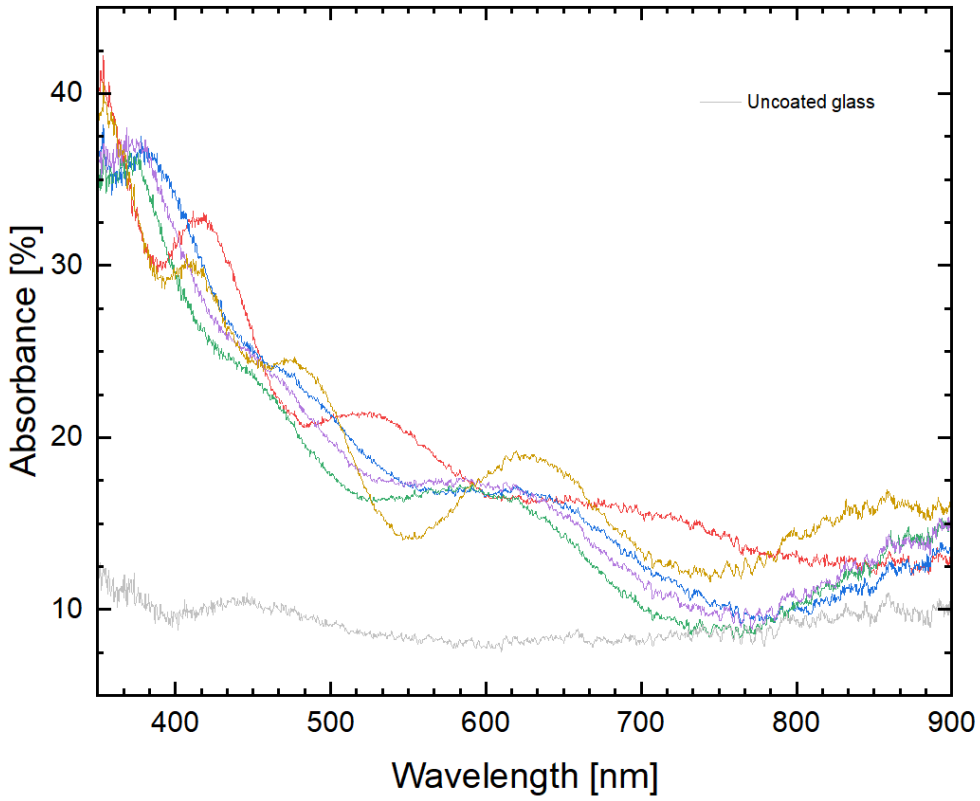

Figure 8.3: UV-Vis absorption spectra of Zr-1,4-BDC film on a glass plate and a sample of clean glass for reference.

The data shows a decrease in absorbance with increasing wavelength, as expected rogowska2022photoactive. We observed the presence of thin film interference on the glass plate with the deposited film, as shown by the oscillations in absorbance.

References

[1] Richard W Johnson, Adam Hultqvist, and Stacey F Bent. A brief review of atomic layer deposition: from fundamentals to applications. Materials today, 17(5):236–246, 2014.

[2] Andrei A Bunaciu, Elena Gabriela UdriŞTioiu, and Hassan Y Aboul-Enein. X-ray diffraction: instrumentation and applications. Critical reviews in analytical chemistry, 45(4):289–299, 2015.

[3] Mikko Ritala and Jaakko Niinistö. Industrial applications of atomic layer deposition. ECS transactions, 25(8):641, 2009.

[4] Chuan-De Wu and Min Zhao. Incorporation of molecular catalysts in metal–organic frameworks for highly efficient heterogeneous catalysis. Advanced Materials, 29(14):1605446, 2017.

[5] Wen-Gang Cui, Tong-Liang Hu, and Xian-He Bu. Metal–organic framework materials for the separation and purification of light hydrocarbons. Advanced Materials, 32(3):1806445, 2020.

[6] Sura Ginting. Synthesis, Structures, Optical and Electronic Properties of Functional Inorganic and Hybrid Materials. PhD thesis, Northern Illinois University, 2020.

[7] David S Sholl and Ryan P Lively. Seven chemical separations to change the world. Nature, 532(7600):435–437, 2016.

[8] Wei-Wei Zhao, Chao-Yan Zhang, Zeng-Guang Yan, Li-Ping Bai, Xiayan Wang, Hongliang Huang, You-Ya Zhou, Yabo Xie, Fa-Sheng Li, and Jian-Rong Li. Separations of substituted benzenes and polycyclic aromatic hydrocarbons using normal-and reverse-phase high performance liquid chromatography with uio-66 as the stationary phase. Journal of Chromatography A, 1370:121–128, 2014.

[9] Isabella Goodenough, Venkata Swaroopa Datta Devulapalli, Wenqian Xu, Mikaela C Boyanich, Tian-Yi Luo, Mattheus De Souza, Mélissandre Richard, Nathaniel L Rosi, and Eric Borguet. Interplay between intrinsic thermal stability and expansion properties of functionalized uio-67 metal–organic frameworks. Chemistry of Materials, 33(3):910–920, 2020.

[10] Kristian Blindheim Lausund and Ola Nilsen. All-gas-phase synthesis of uio-66 through modulated atomic layer deposition. Nature communications, 7(1):13578, 2016.

[11] SM Rossnagel and H Kim. From pvd to cvd to ald for interconnects and related applications. In Proceedings of the IEEE 2001 International Interconnect Technology Conference (Cat. No. 01EX461), pages 3–5. IEEE, 2001.

[12] Jasmina Hafizovic Cavka, Søren Jakobsen, Unni Olsbye, Nathalie Guillou, Carlo Lamberti, Silvia Bordiga, and Karl Petter Lillerud. A new zirconium inorganic building brick forming metal organic frameworks with exceptional stability. Journal of the American Chemical Society, 130(42):13850–13851, 2008.

[13] Jared B DeCoste, Gregory W Peterson, Himanshu Jasuja, T Grant Glover, You-gui Huang, and Krista S Walton. Stability and degradation mechanisms of metal–organic frameworks containing the zr 6 o 4 (oh) 4 secondary building unit. Journal of Materials Chemistry A, 1 (18):5642–5650, 2013.

[14] Joseph E Mondloch, Michael J Katz, Nora Planas, David Semrouni, Laura Gagliardi, Joseph T Hupp, and Omar K Farha. Are zr 6-based mofs water stable? linker hydrolysis vs. capillary-force-driven channel collapse. Chemical communications, 50(64):8944–8946, 2014.

[15] Farhad Ahmadijokani, Rahman Mohammadkhani, Salman Ahmadipouya, Atefeh Shokrgozar, Mashallah Rezakazemi, Hossein Molavi, Tejraj M Aminabhavi, and Mohammad Arjmand. Superior chemical stability of uio-66 metal-organic frameworks (mofs) for selective dye adsorption. Chemical Engineering Journal, 399:125346, 2020.

[16] Farhad Ahmadijokani, Hossein Molavi, Mashallah Rezakazemi, Shima Tajahmadi, Addie Bahi, Frank Ko, Tejraj M Aminabhavi, Jian-Rong Li, and Mohammad Arjmand. Uio-66 metal–organic frameworks in water treatment: A critical review. Progress in Materials Science, 125:100904, 2022.

[17] Kristian Blindheim Lausund. Metal-organic frameworks by molecular layer deposition. 2019.

[18] Hangzhen Lan, Leo D Salmi, Tuukka Rönkkö, Jevgeni Parshintsev, Matti Jussila, Kari Hartonen, Marianna Kemell, and Marja-Liisa Riekkola. Integrated atomic layer deposition and chemical vapor reaction for the preparation of metal organic framework coatings for solid-phase microextraction arrow. Analytica Chimica Acta, 1024:93–100, 2018.

[19] Daniel Buzek, Jan Demel, and Kamil Lang. Zirconium metal–organic framework uio-66: stability in an aqueous environment and its relevance for organophosphate degradation. Inorganic Chemistry, 57(22):14290–14297, 2018.

[20] Catherine P Raptopoulou. Metal-organic frameworks: Synthetic methods and potential applications. Materials, 14(2):310, 2021.

[21] Sixia Wang, Yuan Lv, Youjin Yao, Huijun Yu, and Guang Lu. Modulated synthesis of monodisperse mof-5 crystals with tunable sizes and shapes. Inorganic Chemistry Communications, 93:56–60, 2018.

[22] James Campbell and Begum Tokay. Controlling the size and shape of mg-mof-74 crystals to optimise film synthesis on alumina substrates. Microporous and Mesoporous Materials, 251: 190–199, 2017.

[23] Hussein Rasool Abid, Huyong Tian, Ha-Ming Ang, Moses O Tade, Craig E Buckley, and Shaobin Wang. Nanosize zr-metal organic framework (uio-66) for hydrogen and carbon dioxide storage. Chemical Engineering Journal, 187:415–420, 2012.

[24] Myunghyun Paik Suh, Hye Jeong Park, Thazhe Kootteri Prasad, and Dae-Woon Lim. Hydrogen storage in metal–organic frameworks. Chemical reviews, 112(2):782–835, 2012.

[25] JeongYong Lee, Omar K Farha, John Roberts, Karl A Scheidt, SonBinh T Nguyen, and Joseph T Hupp. Metal–organic framework materials as catalysts. Chemical Society Reviews, 38(5):1450–1459, 2009.

[26] Jian-Rong Li, Julian Sculley, and Hong-Cai Zhou. Metal–organic frameworks for separations. Chemical reviews, 112(2):869–932, 2012.

[27] Jinlin Long, Sibo Wang, Zhengxin Ding, Shuchao Wang, Yangen Zhou, Ling Huang, and Xuxu Wang. Amine-functionalized zirconium metal–organic framework as efficient visible-light photocatalyst for aerobic organic transformations. Chemical Communications, 48(95):11656–11658, 2012.

[28] Shuai Yuan, Liang Feng, Kecheng Wang, Jiandong Pang, Matheiu Bosch, Christina Lollar, Yujia Sun, Junsheng Qin, Xinyu Yang, Peng Zhang, et al. Stable metal–organic frameworks: design, synthesis, and applications. Advanced Materials, 30(37):1704303, 2018.

[29] Hailian Li, Mohamed Eddaoudi, Michael O'Keeffe, and Omar M Yaghi. Design and synthesis of an exceptionally stable and highly porous metal-organic framework. nature, 402(6759): 276–279, 1999.

[30] Yang An, Xinling Lv, Weiyi Jiang, Lingling Wang, Yuxin Shi, Xinxin Hang, and Huan Pang. The stability of mofs in aqueous solutions—research progress and prospects. Green Chemical Engineering, 2023.

[31] Yan Bai, Yibo Dou, Lin-Hua Xie, William Rutledge, Jian-Rong Li, and Hong-Cai Zhou. Zr-based metal–organic frameworks: design, synthesis, structure, and applications. Chemical Society Reviews, 45(8):2327–2367, 2016.

[32] Ulrich S Schubert and Nicola Hüsing. Synthesis of inorganic materials. John Wiley & Sons, 2019.

[33] Guillaume Maurin, Christian Serre, Andrew Cooper, and Gérard Férey. The new age of mofs and of their porous-related solids. Chemical Society Reviews, 46(11):3104–3107, 2017.

[34] Hai-Long Jiang and Qiang Xu. Porous metal–organic frameworks as platforms for functional applications. Chemical Communications, 47(12):3351–3370, 2011.

[35] Hao Li, Libo Li, Rui-Biao Lin, Wei Zhou, Zhangjing Zhang, Shengchang Xiang, and Banglin Chen. Porous metal-organic frameworks for gas storage and separation: Status and challenges. EnergyChem, 1(1):100006, 2019.

[36] Hiroyasu Furukawa, Nakeun Ko, Yong Bok Go, Naoki Aratani, Sang Beom Choi, Eunwoo Choi, A Özgür Yazaydin, Randall Q Snurr, Michael O'Keeffe, Jaheon Kim, et al. Ultrahigh porosity in metal-organic frameworks. Science, 329(5990):424–428, 2010.

[37] Lifeng Ding and A Ozgur Yazaydin. Hydrogen and methane storage in ultrahigh surface area metal–organic frameworks. Microporous and mesoporous materials, 182:185–190, 2013.

[38] Jiong Zhou, Guocan Yu, Qing Li, Mengbin Wang, and Feihe Huang. Separation of benzene and cyclohexane by nonporous adaptive crystals of a hybrid [3] arene. Journal of the American Chemical Society, 142(5):2228–2232, 2020.

[39] Jiwei Qin, Qing Ye, Xiaojuan Xiong, and Ning Li. Control of benzene–cyclohexane separation system via extractive distillation using sulfolane as entrainer. Industrial & Engineering Chemistry Research, 52(31):10754–10766, 2013.

[40] Nicolas Chanut, Aziz Ghoufi, Marie-Vanessa Coulet, Sandrine Bourrelly, Bogdan Kuchta, Guillaume Maurin, and Philip L Llewellyn. Tailoring the separation properties of flexible metal-organic frameworks using mechanical pressure. Nature communications, 11(1):1216, 2020.

[41] Ivor Smith. Chromatography. Elsevier, 2013.

[42] Ozlem Coskun. Separation techniques: chromatography. Northern clinics of Istanbul, 3(2): 156, 2016.

[43] Jian-Rong Li, Ryan J Kuppler, and Hong-Cai Zhou. Selective gas adsorption and separation in metal–organic frameworks. Chemical Society Reviews, 38(5):1477–1504, 2009.

[44] Hui Wu, Taner Yildirim, and Wei Zhou. Exceptional mechanical stability of highly porous zirconium metal–organic framework uio-66 and its important implications. The journal of physical chemistry letters, 4(6):925–930, 2013.

[45] Xueyun Li, Bo Li, Mingchen Liu, Yufeng Zhou, Liyuan Zhang, and Xiaoqiang Qiao. Core–shell metal–organic frameworks as the mixed-mode stationary phase for hydrophilic interaction/reversed-phase chromatography. ACS applied materials & interfaces, 11(10): 10320–10327, 2019.

[46] Xiang Zhao, Yanxiang Wang, Dong-Sheng Li, Xianhui Bu, and Pingyun Feng. Metal–organic frameworks for separation. Advanced materials, 30(37):1705189, 2018.

[47] Fei Gao, Runhan Yan, Yao Shu, Qingbin Cao, and Li Zhang. Strategies for the application of metal–organic frameworks in catalytic reactions. RSC advances, 12(16):10114–10125, 2022.

[48] Peter Ozaveshe Oviroh, Rokhsareh Akbarzadeh, Dongqing Pan, Rigardt Alfred Maarten Coetzee, and Tien-Chien Jen. New development of atomic layer deposition: processes, methods and applications. Science and technology of advanced materials, 20(1):465–496, 2019.

[49] Nagy L Torad, Shuaihua Zhang, Wael A Amer, Mohamad M Ayad, Minjun Kim, Jeonghun Kim, Bing Ding, Xiaogang Zhang, Tatsuo Kimura, and Yusuke Yamauchi. Advanced nanoporous material–based qcm devices: A new horizon of interfacial mass sensing technology. Advanced Materials Interfaces, 6(20):1900849, 2019.

[50] Vlad Pascanu, Greco Gonzalez Miera, A Ken Inge, and Belén Martín-Matute. Metal–organic frameworks as catalysts for organic synthesis: a critical perspective. Journal of the American Chemical Society, 141(18):7223–7234, 2019.

[51] Pieterjan Valvekens, Frederik Vermoortele, and Dirk De Vos. Metal–organic frameworks as catalysts: the role of metal active sites. Catal. Sci. Technol., 3:1435–1445, 2013.

[52] Pilar García-García, Maike Müller, and Avelino Corma. Mof catalysis in relation to their homogeneous counterparts and conventional solid catalysts. Chemical Science, 5(8): 2979–3007, 2014.

[53] Xian Fang, Boyang Zong, and Shun Mao. Metal–organic framework-based sensors for environmental contaminant sensing. Nano-micro letters, 10:1–19, 2018.

[54] Lauren E Kreno, Kirsty Leong, Omar K Farha, Mark Allendorf, Richard P Van Duyne, and Joseph T Hupp. Metal–organic framework materials as chemical sensors. Chemical reviews, 112(2):1105–1125, 2012.

[55] Nan Gao, Runan Tan, Zhiwei Cai, Hui Zhao, Gang Chang, and Yunbin He. A novel electrochemical sensor via zr-based metal organic framework–graphene for pesticide detection. Journal of Materials Science, 56(34):19060–19074, 2021.

[56] Zi-Jian Li, Xue Wang, Lin Zhu, Yu Ju, Zeru Wang, Qian Zhao, Zhi-Hui Zhang, Tao Duan, Yuan Qian, Jian-Qiang Wang, et al. Hydrolytically stable zr-based metal–organic framework as a highly sensitive and selective luminescent sensor of radionuclides. Inorganic Chemistry, 61(19):7467–7476, 2022.

[57] Pengchen Su, Anrui Zhang, Long Yu, Hongwei Ge, Ning Wang, Shuyi Huang, Yuejie Ai, Xiangke Wang, and Suhua Wang. Dual-functional uio-type metal-organic frameworks for the sensitive sensing and effective removal of nitrofurans from water. Sensors and Actuators B: Chemical, 350:130865, 2022.

[58] Elisabetta Comini. Achievements and challenges in sensor devices. Frontiers in Sensors, 1: 607063, 2021.

[59] Jianwei Ren, Henrietta W Langmi, Brian C North, and Mkhulu Mathe. Review on processing of metal–organic framework (mof) materials towards system integration for hydrogen storage. International Journal of Energy Research, 39(5):607–620, 2015.

[60] Abdalla M Abdalla, Shahzad Hossain, Ozzan B Nisfindy, Atia T Azad, Mohamed Dawood, and Abul K Azad. Hydrogen production, storage, transportation and key challenges with applications: A review. Energy conversion and management, 165:602–627, 2018.

[61] Oleksii V Gutov, Wojciech Bury, Diego A Gomez-Gualdron, Vaiva Krungleviciute, David Fairen-Jimenez, Joseph E Mondloch, Amy A Sarjeant, Salih S Al-Juaid, Randall Q Snurr, Joseph T Hupp, et al. Water-stable zirconium-based metal–organic framework material with high-surface area and gas-storage capacities. Chemistry–A European Journal, 20(39): 12389–12393, 2014.

[62] Paul Balcombe, Kris Anderson, Jamie Speirs, Nigel Brandon, and Adam Hawkes. The natural gas supply chain: the importance of methane and carbon dioxide emissions. ACS Sustainable Chemistry & Engineering, 5(1):3–20, 2017.

[63] Matthew J Prosniewski, Tyler A Rash, Ernest W Knight, Andrew K Gillespie, David Stalla, Conrad J Schulz, and Peter Pfeifer. Controlled charge and discharge of a 40-l monolithic adsorbed natural gas tank. Adsorption, 24:541–550, 2018.

[64] Weidong Fan, Xia Wang, Ben Xu, Yutong Wang, Dandan Liu, Ming Zhang, Yizhu Shang, Fangna Dai, Liangliang Zhang, and Daofeng Sun. Amino-functionalized mofs with high physicochemical stability for efficient gas storage/separation, dye adsorption and catalytic performance. Journal of Materials Chemistry A, 6(47):24486–24495, 2018.

[65] Jiafei Lyu, Xuan Zhang, Zhijie Chen, Ryther Anderson, Xingjie Wang, Megan C Wasson, Peng Bai, Xianghai Guo, Timur Islamoglu, Diego A Gomez-Gualdron, et al. Modular synthesis of highly porous zr-mofs assembled from simple building blocks for oxygen storage. ACS applied materials & interfaces, 11(45):42179–42185, 2019.

[66] Jing Dong, Dan Zhao, Yi Lu, and Wei-Yin Sun. Photoluminescent metal–organic frameworks and their application for sensing biomolecules. Journal of Materials Chemistry A, 7(40): 22744–22767, 2019.

[67] Sophie E Miller, Michelle H Teplensky, Peyman Z Moghadam, and David Fairen-Jimenez. Metal-organic frameworks as biosensors for luminescence-based detection and imaging. Interface Focus, 6(4):20160027, 2016.

[68] Mark D Allendorf, Christina A Bauer, RK Bhakta, and RJT Houk. Luminescent metal–organic frameworks. Chemical Society Reviews, 38(5):1330–1352, 2009.

[69] Vonika Ka-Man Au. Recent advances in the use of metal-organic frameworks for dye adsorption. Frontiers in Chemistry, 8:708, 2020.

[70] Yifang Zhao, Heng Zeng, Xiao-Wei Zhu, Weigang Lu, and Dan Li. Metal–organic frameworks as photoluminescent biosensing platforms: mechanisms and applications. Chemical Society Reviews, 50(7):4484–4513, 2021.

[71] Brij Mohan, Sandeep Kumar, Hui Xi, Shixuan Ma, Zhiyu Tao, Tiantian Xing, Hengzhi You, Yang Zhang, and Peng Ren. Fabricated metal-organic frameworks (mofs) as luminescent and electrochemical biosensors for cancer biomarkers detection. Biosensors and Bioelectronics, 197:113738, 2022.

[72] Vera V Butova, Andriy P Budnyk, Alexander A Guda, Kirill A Lomachenko, Aram L Bugaev, Alexander V Soldatov, Sachin M Chavan, Sigurd Øien-Ødegaard, Unni Olsbye, Karl Petter Lillerud, et al. Modulator effect in uio-66-ndc (1, 4-naphthalenedicarboxylic acid) synthesis and comparison with uio-67-ndc isoreticular metal–organic frameworks. Crystal Growth & Design, 17(10):5422–5431, 2017.

[73] Li-Ming Yang, Eric Ganz, Stian Svelle, and Mats Tilset. Computational exploration of newly synthesized zirconium metal–organic frameworks uio-66,-67,-68 and analogues. Journal of Materials Chemistry C, 2(34):7111–7125, 2014.

[74] Diego Gianolio, Jenny Grazia Vitillo, Bartolomeo Civalleri, Silvia Bordiga, U Olsbye, KP Lillerud, Loredana Valenzano, and Carlo Lamberti. Combined study of structural properties on metal-organic frameworks with same topology but different linkers or metal. In Journal of Physics: Conference Series, volume 430, page 012134. IOP Publishing, 2013.

[75] Long Jiao, Joanne Yen Ru Seow, William Scott Skinner, Zhiyong U Wang, and Hai-Long Jiang. Metal–organic frameworks: Structures and functional applications. Materials Today, 27:43–68, 2019.

[76] Sigurd Øien-Ødegaard, Boris Bouchevreau, Knut Hylland, Lianpao Wu, Richard Blom, Carlos Grande, Unni Olsbye, Mats Tilset, and Karl P Lillerud. Uio-67-type metal–organic frameworks with enhanced water stability and methane adsorption capacity. Inorganic chemistry, 55(5):1986–1991, 2016.

[77] Kexin Ling, Meredith M Ogle, Erick Flores, Fernando Godoy, and Angel A Martí. Exploring the photophysical properties of uio-67 mof doped with rhenium carbonyl complexes. Journal of Photochemistry and Photobiology, 11:100–127, 2022.

[78] Qiangyu Zhao, Quanxin Du, Yang Yang, Ziyu Zhao, Jie Cheng, Fukun Bi, Xiaoyu Shi, Jingcheng Xu, and Xiaodong Zhang. Effects of regulator ratio and guest molecule diffusion on vocs adsorption by defective uio-67: Experimental and theoretical insights. Chemical Engineering Journal, 433:134510, 2022.

[79] Jaan Aarik, Andrew R Akbashev, Mikhael Bechelany, Maria Berdova, David Cameron, Nikolai Chekurov, Victor E Drozd, Simon D Elliott, Gloria Gottardi, Kestutis Grigoras10, et al. On the early history of ald: Molecular layering. J. Appl. Chem. USSR, 43:1155–1157, 1970.

[80] Riikka L Puurunen. A short history of atomic layer deposition: Tuomo suntola's atomic layer epitaxy. Chemical Vapor Deposition, 20(10-11-12):332–344, 2014.

[81] Riikka L Puurunen, Jaakko Saarilahti, and Hannu Kattelus. Implementing ald layers in mems processing. ECS Transactions, 11(7):3, 2007.

[82] Yoon Seok Jung, Peng Lu, Andrew S Cavanagh, Chunmei Ban, Gi-Heon Kim, Se-Hee Lee, Steven M George, Stephen J Harris, and Anne C Dillon. Unexpected improved performance

of ald coated licoo2/graphite li-ion batteries. Advanced Energy Materials, 3(2):213–219, 2013.

[83] WMM Kessels, HCM Knoops, MJ Weber, AJM Mackus, and Mariadriana Creatore. Atomic layer deposition of nanomaterials for li-ion batteries, fuel cells, and solar cells. Material Matters, 8(4):117–117, 2013.

[84] Woojin Jeon. Recent advances in the understanding of high-k dielectric materials deposited by atomic layer deposition for dynamic random-access memory capacitor applications. Journal of Materials Research, 35(7):775–794, 2020.

[85] René Vervuurt. Atomic layer deposition for device integration of graphene.

[86] MFJ Vos. Atomic-layer deposition process development-10 steps to successfully develop, optimize and characterize ald recipes. 2019.

[87] Hongyan Xu, Mohammad Karbalaei Akbari, Surender Kumar, Francis Verpoort, and Serge Zhuiykov. Atomic layer deposition–state-of-the-art approach to nanoscale hetero-interfacial engineering of chemical sensors electrodes: A review. Sensors and Actuators B: Chemical, 331:129403, 2021.

[88] Guang-Jie Yuan, Jie-Fei Xie, Hao-Hao Li, Hong-Liang Lu, and Ying-Zhong Tian. Atomic layer deposition of inorganic films for the synthesis of vertically aligned carbon nanotube arrays and their hybrids. Coatings, 9(12):806, 2019.

[89] Xiaoxi Qiao, Xiangjun Zhang, Yu Tian, and Yonggang Meng. Progresses on the theory and application of quartz crystal microbalance. Applied Physics Reviews, 3(3), 2016.

[90] Kannan M Krishnan. Principles of materials characterization and metrology. Oxford University Press, 2021.

[91] Salisu Nasir, Mohd Zobir Hussein, Zulkarnain Zainal, Nor Azah Yusof, Syazwan Afif Mohd Zobir, and Ibrahim Mustapha Alibe. Potential valorization of by-product materials from oil palm: A review of alternative and sustainable carbon sources for carbon-based nanomaterials synthesis. BioResources, 14(1):2352–2388, 2019.

[92] Damian Wojcieszak, Michał Mazur, Danuta Kaczmarek, Agata Poniedziałek, and Małgorzata Osękowska. An impact of the copper additive on photocatalytic and bactericidal properties of tio2 thin films. Mater. Sci. Pol, 35:421–426, 2017.

[93] Hiroyuki Fujiwara. Spectroscopic ellipsometry: principles and applications. John Wiley & Sons, 2007.

[94] Ellipsometry FAQ. J.A. Woollam. (2018, january 8). Retrieved March 8, 2023, from https://www.jawoollam.com/resources/ellipsometry-faqtoggle-id-2.

[95] Jeffrey S Gaffney, Nancy A Marley, and Darin E Jones. Fourier transform infrared (ftir) spectroscopy. Characterization of materials, pages 1–33, 2002.

[96] Marwa El-Azazy. Introductory chapter: infrared spectroscopy-a synopsis of the fundamentals and applications. Infrared Spectroscopy-Principles, Advances, and Applications, pages 1–10, 2018.

[97] Muhammad Sajid Hamid Akash, Kanwal Rehman, Muhammad Sajid Hamid Akash, and Kanwal Rehman. Ultraviolet-visible (uv-vis) spectroscopy. Essentials of pharmaceutical analysis, pages 29–56, 2020.

[98] Melania Rogowska, Ellen Bruzell, Håkon Valen, and Ola Nilsen. Photoactive zr-aromatic hybrid thin films made by molecular layer deposition. RSC advances, 12(25):15718–15727, 2022.

[99] G Scarel, S Ferrari, S Spiga, C Wiemer, G Tallarida, and M Fanciulli. Effects of growth temperature on the properties of atomic layer deposition grown zro 2 films. Journal of Vacuum Science & Technology A: Vacuum, Surfaces, and Films, 21(4):1359–1365, 2003.

[100] Thomas E Macdermott. The structural chemistry of zirconium compounds. Coordination Chemistry Reviews, 11(1):1–20, 1973.

[101] Joonas Merisalu, Taivo Jõgiaas, Toomas Daniel Viskus, Aarne Kasikov, Peeter Ritslaid, Tanel Käämbre, Aivar Tarre, Jekaterina Kozlova, Hugo Mändar, Aile Tamm, et al. Structure and electrical properties of zirconium-aluminum-oxide films engineered by atomic layer deposition. Coatings, 12(4):431, 2022.

[102] Antti Rahtu and Mikko Ritala. Reaction mechanism studies on the zirconium chloride–water atomic layer deposition process. Journal of Materials Chemistry, 12(5):1484–1489, 2002.

[103] Kristian Blindheim Lausund, Malin Solheim Olsen, Per-Anders Hansen, Håkon Valen, and Ola Nilsen. Mof thin films with bi-aromatic linkers grown by molecular layer deposition. Journal of Materials Chemistry A, 8(5):2539–2548, 2020.

[104] Kaupo Kukli, Katarina Forsgren, Jaan Aarik, Teet Uustare, Aleks Aidla, Antti Niskanen, Mikko Ritala, Markku Leskelä, and Anders Hårsta. Atomic layer deposition of zirconium oxide from zirconium tetraiodide, water and hydrogen peroxide. Journal of Crystal Growth, 231(1-2):262–272, 2001.

[105] Jaan Aarik, Aleks Aidla, Hugo Mändar, Teet Uustare, and Väino Sammelselg. Growth kinetics and structure formation of zro2 thin films in chloride-based atomic layer deposition process. Thin Solid Films, 408(1-2):97–103, 2002.

[106] Miika Mattinen, Georgi Popov, Marko Vehkamaki, Peter J King, Kenichiro Mizohata, Pasi Jalkanen, Jyrki Raisanen, Markku Leskela, and Mikko Ritala. Atomic layer deposition of emerging 2d semiconductors, hfs2 and zrs2, for optoelectronics. Chemistry of Materials, 31 (15):5713–5724, 2019.

[107] Aile Tamm, Helle-Mai Piirsoo, Taivo Jõgiaas, Aivar Tarre, Joosep Link, Raivo Stern, and Kaupo Kukli. Mechanical and magnetic properties of double layered nanostructures of tin and zirconium oxides grown by atomic layer deposition. Nanomaterials, 11(7):1633, 2021.

[108] Linlin Wan, Chen Zhou, Kai Xu, Bo Feng, and Aisheng Huang. Synthesis of highly stable uio-66-nh2 membranes with high ions rejection for seawater desalination. Microporous and Mesoporous Materials, 252:207–213, 2017.

[109] Michael J Katz, Zachary J Brown, Yamil J Colón, Paul W Siu, Karl A Scheidt, Randall Q Snurr, Joseph T Hupp, and Omar K Farha. A facile synthesis of uio-66, uio-67 and their derivatives. Chemical Communications, 49(82):9449–9451, 2013.

[110] Karen Leus, Thomas Bogaerts, Jeroen De Decker, Hannes Depauw, Kevin Hendrickx, Henk Vrielinck, Veronique Van Speybroeck, and Pascal Van Der Voort. Systematic study of the chemical and hydrothermal stability of selected "stable" metal organic frameworks. Microporous and Mesoporous Materials, 226:110–116, 2016.

[111] Xiaowei Zhao, Wenzui Jin, Jinguang Cai, Jianfeng Ye, Zhenhu Li, Yurong Ma, Jinglin Xie, and Limin Qi. Shape-and size-controlled synthesis of uniform anatase tio2 nanocuboids enclosed by active {100} and {001} facets. Advanced Functional Materials, 21(18):3554–3563, 2011.

[112] Ruijuan Qi and Yan Cheng. Synthesis of se nanowires at room temperature using selenourea as se source. Journal of Materials Science: Materials in Electronics, 31:5843–5847, 2020.

[113] V Petrovic. Boronic acids in molecular layer deposition. Master's thesis, 2019.

[114] Priya Sinha, Archit Datar, Chungsik Jeong, Xuepeng Deng, Yongchul G Chung, and Li-Chiang Lin. Surface area determination of porous materials using the brunauer–emmett–teller (bet) method: limitations and improvements. The Journal of Physical Chemistry C, 123(33):20195–20209, 2019.

[115] Francis Verpoort, T Haemers, P Roose, and J-P Maes. Characterization of a surface coating formed from carboxylic acid-based coolants. Applied spectroscopy, 53(12):1528–1534, 1999.